ELECTRO-MAGNETIC SOURCE IMAGING USING REALISTIC HEAD MODELS

A THESIS SUBMITTED TO
THE GRADUATE SCHOOL OF NATURAL AND APPLIED SCIENCES
OF
MIDDLE EAST TECHNICAL UNIVERSITY

BY

ZEYNEP AKALIN ACAR

IN PARTIAL FULFILLMENT OF THE REQUIREMENTS
FOR
THE DEGREE OF DOCTOR OF PHILOSOPHY
IN
ELECTRICAL AND ELECTRONICS ENGINEERING

JUNE 2005

Approval of the Graduate School of Natural and Applied Sciences.

Prof. Dr. Canan Özgen
Director

I certify that this thesis satisfies all the requirements as a thesis for the degree of Doctor of Philosophy.

Prof. Dr. İsmet Erkmen
Head of Department

This is to certify that we have read this thesis and that in our opinion it is fully adequate, in scope and quality, as a thesis for the degree of Doctor of Philosophy.

Prof. Dr. Nevzat G. Gençer
Supervisor

Examining Committee Members

Prof. Dr. Mustafa Kuzuoğlu	(METU, EEE)	_____
Prof. Dr. Nevzat G. Gençer	(METU, EEE)	_____
Prof. Dr. Pekcan Ungan	(Hacettepe Univ.)	_____
Prof. Dr. B. Murat Eyüboğlu	(METU, EEE)	_____
Assist. Prof. Dr. Yeşim Serinağaoğlu	(METU, EEE)	_____

I hereby declare that all information in this document has been obtained and presented in accordance with academical rules and ethical conduct. I also declare that, as required by these rules and conduct, I have fully cited and referenced all material and results that are not original to this work.

Name, Last Name :

Signature :

ABSTRACT

ELECTRO-MAGNETIC SOURCE IMAGING
USING REALISTIC HEAD MODELS

Akalın Acar, Zeynep
Ph.D., Department of Electrical and Electronics Engineering
Supervisor: Prof. Dr. Nevzat G. Gençer

June 2005, 170 pages

Electro-Magnetic Source Imaging (EMSI) is the estimation of the position, orientation and strength of active electrical sources within the brain from electrical and magnetic measurements. For an accurate source localization, the head model must correctly represent the electrical and geometrical properties of the head. To solve the forward problem using realistic head models numerical techniques must be used. This work uses the Boundary Element Method (BEM) for solving the forward problem. The accuracy of the existing BEM formulation is improved by using second order elements, recursive integration and the isolated problem approach (IPA). Two new formulations are developed to improve the solution speed by computing transfer matrices for EEG and MEG solutions. The IPA formulation is generalized and integrated into the accelerated BEM algorithm. Once the transfer matrices are computed, the forward solutions take about 300 ms for a 256 sensor EEG and MEG system.

The head model used in the BEM solutions is constructed by segmenting three dimensional multimodal magnetic resonance images. For segmentation, a semi-automatic hybrid algorithm is developed that makes use of snakes, mor-

phological operations, thresholding and region growing. The mesh generation algorithm allows intersecting tissue compartments.

For the inverse problem solution genetic algorithm (GA) is used to search for a given number of dipoles. Source localization with simulated data show that the localization error is within 1.1 mm for EEG and 1.2 mm for MEG when SNR is 10 on a realistic model with 7 compartments. When a single-dipole source in a realistic model is explored using a best-fit spherical model, the localization errors increase up to 8.5 mm for EEG and 7 mm for MEG. Similar tests are also performed with multiple dipoles. It was observed that realistic models provide definitely more accurate results compared to spherical models. The EMSI approach is also tested using experimental EEG data to localize the sources of auditory evoked potentials. The reconstructed source locations are correctly found in the Heschl's gyrus. In conclusion, this thesis presents a complete source localization framework for future brain research using the EMSI.

Keywords: Electro-Magnetic Source Imaging, Boundary Element Method, forward problem, segmentation, mesh generation, inverse problem, genetic algorithm.

ÖZ

GERÇEKÇİ KAFA MODELLERİ KULLANARAK
ELEKTRO-MANYETİK KAYNAK GÖRÜNTÜLEME

Akalın Acar, Zeynep
Doktora, Elektrik ve Elektronik Mühendisliği Bölümü
Tez Yöneticisi: Prof. Dr. Nevzat G. Gençer

Haziran 2005, 170 sayfa

Elektro-Manyetik Kaynak Görüntüleme (EMKG) beyin içerisindeki aktif elektriksel kaynakların yer, yön ve şiddetlerinin kafa yüzeyinden alınan potansiyel ve manyetik alan ölçümleri kullanılarak tespit edilmesidir. Kaynakların yerlerini doğru olarak tespit edebilmek için kullanılan modelin kafanın elektriksel ve geometrik özelliklerini doğru bir biçimde yansıtması gerekir. İleri problemi gerçekçi modellerle çözebilmek için sayısal yöntemler kullanılmalıdır. Bu çalışmada ileri problemi çözmek için Sınır Elemanı Yöntemi (BEM) kullanılmaktadır. Mevcut BEM formülasyonunun doğruluğu ikinci derece elemanlar, tekrarlamalı integral hesaplaması ve izole problem yaklaşımı (IPA) kullanılarak iyileştirilmiştir. Çözüm hızını arttırmak amacıyla EEG ve MEG için geliştirilen iki yeni formülasyonla transfer matrisleri oluşturulmuştur. Genelleştirilen IPA formülasyonu hızlandırılmış BEM algoritmasına entegre edilmiştir. Bu sayede transfer matrisleri hesaplandıktan sonra, ileri problem çözüm süresi 256 kanallı bir EEG ve MEG sistemi için yaklaşık 300 ms olmaktadır.

BEM çözümlerinde kullanılan kafa modelleri üç boyutlu çok kipli MR

görüntülerinden bölütleme ile elde edilmektedir. Bölütleme için, morfolojik operasyonlar, yılanlar, alan büyütme ve sınırlama işlemleri kullanan yarı otomatik hibrid bir algoritma geliştirilmiştir. Bölütleme sonrası kullanılan ağ oluşturma algoritması kesişen dokuların modellenmesine olanak sağlamaktadır.

Geri problem çözümü için genetik algoritma (GA) verilen sayıda dipol aramak için kullanılmıştır. Üretilmiş verilerle yapılan denemelerde konumlandırma hatası, yedi bölmeli gerçekçi bir modelde sinyal gürültü oranı (SNR) 10 alındığında, EEG için 1.1 mm, MEG için ise 1.2 mm olmaktadır. Gerçekçi bir kafa modeline yerleştirilen tek bir dipol gerçekçi modele en iyi uyacak bir küresel model ile araştırıldığında, konumlandırma hataları EEG ve MEG için 8.5 ve 7 mm'ye yükselmiştir. Benzer testler birden fazla dipol ile de gerçekleştirilmiş ve gerçekçi kafa modellerinin küresel modellere göre daha doğru sonuç verdiği kesin olarak gözlenmiştir.

Bu çalışmada gerçekleştirilen EMKG yaklaşımı bir duyma deneyi ile elde edilen EEG ölçümlerinden kaynakları bulmak için de kullanılmıştır. Aranan kaynaklar, doğru olarak Heschl girusunda tespit edilmiştir. Sonuç olarak bu tez, gerçekçi kafa modelleri kullanarak EMKG ileri ve geri problemlerinin çözülmesi için komple bir platform oluşturmaktadır.

Anahtar Kelimeler: Elektro-Manyetik Kaynak Görüntüleme, Sınır Elemanı Yöntemi, ileri problem, bölütleme, ağ oluşturma, geri problem, genetik algoritma.

ACKNOWLEDGMENTS

I would like to thank all the people who contributed to this study. First of all, I'm very grateful to my supervisor Dr. Nevzat G. Gençer who has given me the opportunity to fulfill this research and for his support, guidance and motivation. I would also like to thank Dr. Pekcan Ungan and Dr. Süha Yağcıoğlu from the Department of Biophysics in Hacettepe University, for their cooperation in acquiring experimental EEG data and for the support and suggestions they have given. I would also like to thank them for their hospitality during my visits there. I also acknowledge my thesis examining committee members for reading the manuscript of the thesis.

I would like to thank Dr. Mehmet Çamurdanoğlu from the Bayındır Hospital, Dr. Serdar Akyar and Dr. Suat Fitöz from the Ankara University Medical Faculty for their helps in supplying and analyzing the MR images.

I would like to express my gratitude to my family, friends and parents-in-law for their friendship and support. I would especially like to thank my parents who have respected and supported my personal choices throughout my education.

Finally, I want to dedicate this work to my husband Dr. Can Erkin Acar, whose help, understanding and patience was invaluable during the course of this study.

TABLE OF CONTENTS

PLAGIARISM iii

ABSTRACT iv

ÖZ vi

ACKNOWLEDGMENTS viii

TABLE OF CONTENTS ix

LIST OF TABLES xiii

LIST OF FIGURES xv

LIST OF ABBREVIATIONS xx

CHAPTER

1 INTRODUCTION 1

1.1 Brain Anatomy and Neurophysiology 2

1.1.1 Brain Anatomy 2

1.1.2 Neurophysiology 4

1.2 Electroencephalography 7

1.3 Magnetoencephalography 11

1.4 Electro-Magnetic Source Imaging 13

1.4.1 Source Models 15

1.4.2 Head Modelling 16

1.4.2.1 Simple Head Models 16

1.4.2.2 Realistic Head Models 18

1.4.3 Inverse Problem 19

1.5 Purpose of the Thesis 20

1.6 Thesis Outline 21

2 AN ADVANCED BOUNDARY ELEMENT METHOD IMPLEMENTATION . . . 23
2.1 Introduction . . . 23
2.2 BEM Formulation . . . 25
2.3 Accelerated BEM for EEG . . . 28
2.4 Accelerated BEM for MEG . . . 30
2.5 Results . . . 31
2.5.1 Increasing accuracy using the recursive integration . . . 32
2.5.2 Validation of the intersecting meshes . . . 33
2.5.3 Sensitivity of the measurements to eye conductivity . . . 34
2.5.4 Computation speed . . . 35
3 USE OF THE ISOLATED PROBLEM APPROACH FOR MULTI-COMPARTMENT BEM MODELS . . . 37
3.1 Intoduction . . . 37
3.2 Isolated Problem Approach . . . 39
3.3 Accelerated BEM for EEG . . . 43
3.4 Accelerated BEM for MEG . . . 44
3.5 Results . . . 45
3.5.1 Accuracy of the BEM solutions . . . 45
3.5.2 Results with the realistic model . . . 47
3.5.2.1 The effect of the CSF layer on the potentials: . . . 47
3.5.2.2 The effect of an inhomogeneity in the brain: . . . 48
3.5.2.3 The effect of the IPA on the potentials when there is an inhomogeneity: 49
3.5.3 Computation speed . . . 51
4 REALISTIC HEAD MODELING: THE SEGMENTATION PHASE . . . 53
4.1 Introduction . . . 53
4.2 Properties of MR images . . . 54
4.3 The Hybrid Segmentation Algorithm . . . 55
4.3.1 The Snakes Algorithm . . . 59
4.3.2 Automatic Threshold Selection . . . 61

4.3.3 Morphological Processing 63
4.3.4 Region Growing 65
4.4 Results 65
5 REALISTIC HEAD MODELING: THE MESH GENERATION PHASE 69
5.1 Introduction 69
5.2 The Mesh Generation Algorithm 70
5.2.1 Generation of Individual Meshes 70
5.2.2 Mesh Generation for Intersecting Surfaces . . . 71
5.3 The Algorithms used in Mesh Generation 72
5.3.1 Triangulation 73
5.3.2 Smoothing 74
5.3.3 Coarsening 75
5.3.3.1 Basic Quadric Error Metric 77
5.3.3.2 Vertex Placement 78
5.3.4 Topological correction 79
5.4 Results 80
6 REGISTRATION OF MRI AND EEG DATA 85
6.1 Introduction 85
6.2 The method 86
6.3 Results 88
6.3.1 Simulations 88
6.3.2 Realistic mapping 89
7 THE INVERSE PROBLEM OF EMSI 91
7.1 Introduction 91
7.2 The Inverse Problem Approaches 92
7.2.1 Parametric methods 95
7.2.2 Imaging methods 96
7.2.3 Choice of the inverse method 99
7.3 Auditory experiments 100
7.4 Genetic Algorithms 102
7.4.1 Basic Concept of GAs 104
7.4.2 Genetic operators 104
7.4.2.1 Selection 105

7.4.2.2 Crossover . . . 105
7.4.2.3 Mutation . . . 105
7.4.3 Comparison of GA with other algorithms . . . 106
7.4.4 Improvements to basic GA . . . 107
7.5 Results . . . 108
7.5.1 Performance of GA for source localization . . . 108
7.5.2 Simulation studies with realistic head models . 119
7.5.3 Source localization using experimental EEG data . . . 124
7.5.3.1 Stimulation and recording . . . 125
7.5.3.2 Data processing . . . 127
7.5.3.3 EEG dipole source analysis . . . 127
8 CONCLUSION AND DISCUSSION . . . 142
8.1 Accuracy of the BEM . . . 142
8.2 Accelerated BEM . . . 144
8.3 Head modeling . . . 145
8.4 Inverse Problem . . . 146
REFERENCES . . . 148
APPENDICES . . . 165
A BEM FORMULATION . . . 165
VITA . . . 167

LIST OF TABLES

2.1 Conductivities (in S/m) of the tissues in Figure 2.2 for 5 different cases. 33

2.2 RDM change in potential values between models with eyes and without eyes for a dipole located parallel to the eyes for eye conductivities of 0.3, 0.4, and 0.5 S/m 35

2.3 RDM change in potential values between models with eyes and without eyes for a dipole directed towards the eyes for eye conductivities of 0.3, 0.4, and 0.5 S/m 35

2.4 Computational complexity for a realistic mesh with 7988 nodes, A_s matrix has 1910 nodes 36

3.1 The relative difference measures (%RDMs and RDM*s) for various tangential (x-directed) dipoles located on the z axis ($z = 1 - 6\ cm$) in a 4-layer spherical head model. The results are presented for solutions with and without the IPA. 46

3.2 The relative difference measures (%RDMs and RDM*s) for various radial (z-directed) dipoles located on the z axis ($z = 1 - 6\ cm$) in a 4-layer spherical head model. The results are presented for solutions with and without IPA. 46

3.3 The %RDMs, RDM*s and MAG values for x- and z-directed dipoles located on the z axis. The potentials of the reference head model are compared with the potentials when there is no CSF layer in the head model. 48

3.4 Effect of the inhomogeneity on the potential solutions. The potentials using the two head models are compared. %RDMs, RDM*s and MAG values for a dipole located 0.5 cm near the inhomogeneity are presented. The dipole is oriented parallel and perpendicular to the inhomogeneity. 49

3.5 Effect of the IPA on the potential solutions when inhomogeneity is included. % RDM , RDM*s and MAGs for a dipole located 0.5 cm near the inhomogeneity are presented. The dipole is oriented parallel and perpendicular to the inhomogeneity. 50

3.6 Computational complexity for a realistic mesh with 9906 nodes, A_s matrix has 3828×3828 entries. 51

4.1 Summary of MRI Tissue Characteristics of Brain Structures . 55

6.1 Simulated Registration Results: The average error after registration using different number of sensors with different orientation and noise. 88

7.1 Comparison between GA and Gradient-Based Optimization and Search Procedures [1] 107
7.2 Mean localization (LE, mm) and orientation errors (OE, degrees) for the dipoles placed on the grid shown in Figure 7.2. The results are obtained using the analytical solutions of the potential field. 114
7.3 Mean localization (LE, mm) and orientation errors (OE, degrees) for dipoles placed on the grid shown in Figure 7.2. The results are obtained using the analytical solutions of the magnetic field. 119
7.4 Mean EEG and MEG localization errors (mm) for the dipole setup shown in Figure 7.12. The simulated data is generated from Model1 by adding sensor noise with SNR=10. 123
7.5 Mean and maximum EEG localization errors (mm) when dipoles are located face-to-face, with different separations (mm). The simulated data is generated from the realistic model by adding sensor noise with SNR=10. 124
7.6 The RDM (%) values for the auditory experiment, showing the error between the measured data and field computed from the localized dipoles. The localization results for both spherical and realistic head models are shown. 132

LIST OF FIGURES

1.1 The primary divisions of the human brain. (This figure is reproduced from [2].) . . . 3
1.2 The neuron. (This figure is reproduced from [3].) . . . 5
1.3 A coronal slice of the brain. (This figure is reproduced from [4].) . . . 6
1.4 The structure of the gray matter. The white cells correspond to pyramidal cells. (This figure is reproduced from [5].) . . . 6
1.5 The four lobes of the brain. (This figure is reproduced from [5].) 7
1.6 An illustration of the excitatory and inhibitory post synaptic potentials. The voltage measurements are presented on the right of the figure. Due to excitatory presynaptic activity, an action potential is depicted. (This figure is reproduced from [6].) . . . 8
1.7 A typical EEG pattern of an awake person. This data is obtained using the EEG system in Hacettepe University, Department of Biophysics. . . . 10
1.8 data acquisition system, (a) amplifiers, (b) a 256 channel cap. (These figures are reproduced from [7].) . . . 11
1.9 (a) MEG system in a shielded room, (b) An MEG system with the patient and the clinician. The MEG sensors are uniformly distributed over the inner surface of a helmet-shaped dewar. (These figures are reproduced from [8].) . . . 13
1.10 Block diagram of Electro-Magnetic Source Imaging. . . . 14

2.1 A 6-noded triangular, quadratic and isoparametric BEM element. . . . 26
2.2 The cross-section of the model used in the FEM and BEM calculations. Regions corresponding to scalp, skull, brain and eye are labelled as 1, 2, 3, and 4, respectively. . . . 34

3.1 Schematic representation of the model. The model has L layers where $(K-1)^{th}$ compartment has a low conductivity that corresponds to the skull in a head model. . . . 41
3.2 The cut-away view of the head mesh including the inhomogeneity. . . . 49

3.3 The top view of the head model to show the location of the inhomogeneity and the dipole. 50
3.4 Contour plots on a realistic head mesh with and without IPA for various inhomogeneity conductivities: (a) and (b) no inhomogeneity, (c) and (d) inhomogeneity with low conductivity = 0.033 S/m, (e) and (f) inhomogeneity with high conductivity = 3.3 S/m. 52

4.1 MR images of an axial slice in the head. (a) T_1–weighted, (b) T_2–weighted, (c) PD–weighted. 56
4.2 Obtaining the scalp surface. (a) A slice in PD images, (b) the slice after simple thresholding of this slice, (c) the snakes algorithm is applied to the slice, (d) scalp is extracted using the snakes algorithm. 57
4.3 Flowchart of the segmentation algorithm. 58
4.4 Dilation and erosion operations. (a) the original image, (b) dilated image, (c) eroded image. 64
4.5 Segmentation of the skull (a) before removing the holes, (b) after removing the holes. 66
4.6 Segmentation of a slice. (a) A slice from T1 image, (b) segmented slice. The sinuses and the skull are segmented together. 66
4.7 Segmented tissues of the whole head (a) scalp, (b) skull, (c) cortex, (d) WM, (e) eyes, (f) eyeballs. 67

5.1 The flowchart of the mesh generation algorithm. 71
5.2 The flowchart of the algorithm for intersecting meshes. 72
5.3 (a) Spherical surface partially corrupted by white noise, (b) after 10 steps of smoothing, (c) after 50 steps of smoothing, (d) after 200 steps of smoothing. (This figure is reproduced from [9].) 76
5.4 Contraction of an edge. (This figure is reproduced from [10].) . 77
5.5 The meshes generated for (a) scalp, (b) skull, (c) cortex and (d) white matter. All layers are represented using 4000 elements. 81
5.6 The mesh of the outer skull and eye tissues (a) before intersection (b) after intersection. The mesh contains 2003 elements. 82
5.7 A figurative representation of the head mesh. 83
5.8 Cut-away view of the BEM mesh showing the inner layers. For simplicity in illustrations the quadratic elements of the mesh are displayed as linear elements. 83

6.1 Illustration of registration of simulated noise free digitizer points to MRI data. (a) Before registration, (b) after registration. . . 89
6.2 Registration of measured electrode positions to the segmented scalp surface. The locations of the 256 electrodes on the head surface. 89

7.1 The forward and inverse problems of EMSI. The forward problem computes fields from the sources. The inverse problem locates sources from the measurements. 94
7.2 A grid of dipole locations are shown on the x-z plane for a four-layer spherical model. The dipole orientations projected onto the x-z plane are also displayed for a specific grid point. . 109
7.3 Electrode locations on the spherical surface. (a) 64 electrodes, (b) 128 electrodes, (c) 256 electrodes. 110
7.4 Localization errors (mm) for a grid of dipoles when there are 64 electrodes. The potential field is calculated analytically. (a) SNR=5, (b) SNR=10. 111
7.5 Localization errors (mm) for a grid of dipoles when there are 128 electrodes. The potential field is calculated analytically. (a) SNR=5, (b) SNR=10. 112
7.6 Localization errors (mm) for a grid of dipoles when there are 256 electrodes. The potential field is calculated analytically. (a) SNR=5, (b) SNR=10. 113
7.7 Localization errors for a grid of dipoles when there are 64 electrodes. The forward problem solutions for the potential field are obtained numerically. SNR=10. 115
7.8 Localization errors (mm) for a grid of dipoles when there are 64 sensors. The magnetic field is calculated analytically. (a) SNR=5, (b) SNR=10. 116
7.9 Localization errors (mm) for a grid of dipoles when there are 128 sensors. The magnetic field is calculated analytically. (a) SNR=5, (b) SNR=10. 117
7.10 Localization errors (mm) for a grid of dipoles when there are 256 sensors. The magnetic field is calculated analytically. (a) SNR=5, (b) SNR=10. 118
7.11 Realistic models. (a) Model 1, the reference model, (b) Model 2, the eyes are removed from the reference model (the eye conductivities are assumed to be equal to the skull conductivity), (c) Model 3, the eyes and the CSF are removed from the reference model (CSF conductivity is assumed to be equal to the brain conductivity). 121
7.12 Position of the dipoles used in realistic head simulations. The inverse problem solutions are done for two directions: horizontal, towards the face, and vertical, towards the top. 122
7.13 Selection of the scalp points to find the best-fit sphere. 122
7.14 The scalp surface and the best fit sphere. 123
7.15 Face-to-face dipole configuration for multiple dipole localization simulations. The dipole separation between the face-to-face dipoles is (a) 4 cm and (b) 1 cm. 124
7.16 Block-diagram of the EEG system in the Biophysics Department of the Hacettepe University. 126
7.17 Timing related to stimuli and data acquisition during the AEP experiment. 126

7.18 Position of the selected electrodes on the scalp surface, after applying the segmentation (Chapter 4) and registration (Chapter 6) processes. 127
7.19 (a) The subject (the author of this thesis) with the electrode cap. (b) Süha Yağcıoğlu and Nevzat Gençer injecting gel into the electrodes. 128
7.20 Acquired EEG data for all channels. Each channel is plotted with a different color. (a) Before filtering, (b) after filtering. The Red line shows the specific time instant where the data of 128 channels are used for source localization. 129
7.21 Topographic view of the electrode potentials on the scalp surface with 1 kHz stimulus, (a) top view, (b) left view, (c) back view. The time instant corresponding to this potential profile is shown in Figure 7.20(b) 130
7.22 Topographic view of the electrode potentials on the scalp surface with 5 kHz stimulus, (a) top view, (b) left view, (c) back view. The time instant corresponding to this potential profile is shown in Figure 7.20(b) 131
7.23 Location of the estimated dipoles for the 1kHz stimuli shown (a) on the axial MR slice, (b) on the segmented axial brain slice. Activities of each temporal lobe are presented using a single equivalent dipole. 133
7.24 Location of the estimated dipoles for the 1kHz stimuli shown on the segmented brain slices (a) sagittal view, (b) coronal view. Activities of each temporal lobe are presented using a single equivalent dipole. 134
7.25 Location of the estimated dipoles for the 5kHz stimuli shown (a) on the axial MR slice, (b) on the segmented axial brain slice. Activities of each temporal lobe are presented using a single equivalent dipole. 135
7.26 Location of the estimated dipoles for the 5kHz stimuli shown on the segmented brain slices (a) sagittal view, (b) coronal view. Activities of each temporal lobe are presented using a single equivalent dipole. 136
7.27 Location of the estimated dipoles for the 1kHz stimuli shown (a) on the axial MR slice, (b) on the segmented axial brain slice. Activities of each temporal lobe are presented using two equivalent dipoles. 137
7.28 Location of the estimated dipoles for the 1kHz stimuli shown on the segmented brain slices (a) sagittal view, (b) coronal view. Activities of each temporal lobe are presented using two equivalent dipoles. 138
7.29 Location of the estimated dipoles for the 1kHz stimuli shown (a) on the axial MR slice, (b) on the segmented axial brain slice. Activities of each temporal lobe are presented using three equivalent dipoles. 139

7.30 Location of the estimated dipoles for the 1kHz stimuli shown on the segmented brain slices (a) sagittal view, (b) coronal view. Activities of each temporal lobe are presented using three equivalent dipoles. 140
7.31 The location of Heschls gyrus where the auditory sources are found. (This figure is reproduced from [11].) 141

LIST OF ABBREVIATIONS

ASC Adaptive Skeleton Climbing

BEM Boundary Element Method

CT Computerized Tomography

CSF Cerebrospinal Fluid

EEG Electroencephalography

EMSI Electro-Magnetic Source Imaging

ESI Electrical Source Imaging

FDM Finite Difference Method

FEM Finite Element Method

FP Forward Problem

GA Genetic Algorithms

GM Gray Matter

IP Inverse Problem

IPA Isolated Problem Approach

MEG Magnetoencephalography

MR Magnetic Resonance

MSI Magnetic Source Imaging

PD Proton Density

RDM Relative Difference Measure

RHS Right Hand Side

WM White Matter

CHAPTER 1

INTRODUCTION

Understanding the structure and functionality of the brain has been one of the most challenging problems. Twenty-five centuries ago, Hippocrates wrote:

"Men ought to know that from nothing else but the brain comes joys, delights, laughter and sports, and sorrows, griefs, despondency and lamentations. And by this, in an especial manner, we acquire wisdom and knowledge, and see and hear, and know what we are foul and what we are fair, what are bad and what are good, what are sweet and what unsavory; some we perceive by habit and some we perceive by utility... And by the same organ we become mad and delirious, and fears and terrors assail us, some by night and some by day, and dreams and untimely wanderings, and cares that are not suitable, and ignorance of present circumstances, desuetude and unskilfulness. All these things we endure from the brain."

A lot of information have been obtained about the brain through scientific research over the past century. This includes an understanding of how some parts of the brain carry out sensory functions. How we acquire wisdom and knowledge is a fascinating but much harder problem to study.

Furthermore, the human brain, due to its structural and functional complexity, is more vulnerable and sensitive compared with the rest of the human body. A lot of brain related diseases and disorders such as Alzheimer, Parkinson, multiple sclerosis, epilepsy, dementia and brain tumors threaten the individuals and society, and need to be researched, understood and cured.

This research attempts to contribute to understanding the brain functions.

The tools and investigation framework constructed in this thesis attempts to improve the state of the art in brain research.

This chapter introduces the head modeling and source localization framework developed during the course of the thesis work. In head modeling, the geometrical and electrical properties of the head are represented in a form suitable for computation of potentials and magnetic fields. The aim of source localization is to find the electrically active regions within the brain from external potential (electroencephalogram, EEG) and magnetic field (magnetoencephalogram, MEG) measurements. In order to provide some background information, first the brain anatomy and basic aspects of neurophysiology are summarized. This is followed by two sections on EEG and MEG that describe the origin and properties of these signals. In Section 1.4 the electro-magnetic source imaging (EMSI) problem is defined. In that section, the historical development of head modelling is summarized, source models are introduced and the forward and inverse problem algorithms are discussed. Finally, in Sections 1.5 and 1.6 the purpose and the outline of the thesis are presented.

1.1 Brain Anatomy and Neurophysiology

1.1.1 Brain Anatomy

The brain can be divided into three primary regions: the brainstem, the cerebellum and the cerebrum. The brainstem contains nerve fibers that allow signals (*action potentials*) to travel between the spinal cord and the higher brain centers. The two egg-shaped structures at the sides of the top of the brainstem are the *thalamus*. It is an important integrating center and the relay station for all sensory input to the cortex, except smell. The *cerebellum* provides fine control of muscle movements and is located on top and to the back of the brainstem. An illustration of the main brain regions is given in Figure 1.1.

The *cerebrum* is the largest part of the brain. It is divided into two almost equal halves. The 2–3 mm thick outer region of the cerebrum is called the

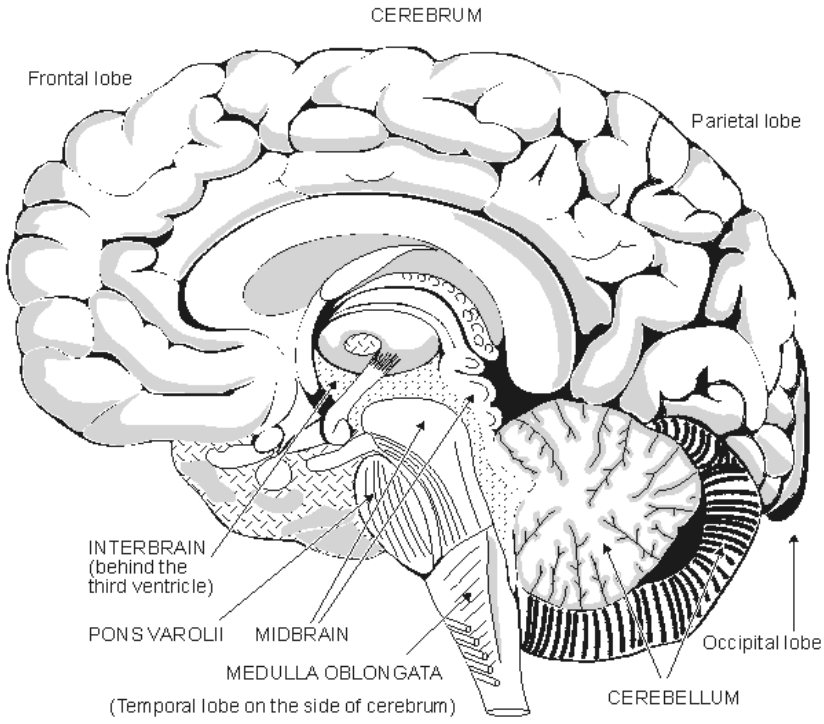

Figure 1.1: The primary divisions of the human brain. (This figure is reproduced from [2].)

cerebral cortex. It has a surface area of about 1600 cm^2 and contains about 10^{10} *neurons* (nerve cells) [12]. Neurons have varying shapes and sizes but have the same anatomical structure (Figure 1.2). The soma (cell body) contains the nucleus of the cell. The inputs from other cells are received through dendrites that arise from the soma and branch repeatedly to connect to the other cells. The impulses are sent to the other cells through a single axon. The end of the axon is divided into branches which connect to the other neurons through *synapses*. The synapse is a specialized interface between two neurons [5]. The neurons in the cortex are strongly interconnected. A single neuron may have 10^3 to 10^5 synapses that connect to other neurons [12].

In Figure 1.3 a coronal slice of the brain is shown. The outermost surface of the brain, the cortex, is composed of *gray matter*, which contains the cell body and dendrites of the neurons. Just below the gray matter is a second major region, the *white matter*, in which axons of the nerve cells predominate. In humans, white matter volume is roughly equal to that of the cortex. White matter interconnections (*association fibers*) are also quite numerous. An under

surface area of cortex of 1 cm^2 may contain 10^7 input fibers, mostly connecting different regions of the cortex. A much smaller number of the fibers that enter the underside of the cortical surface (maximum 5%) radiate from the thalamus and other subcortical structures. The *ventricles* consists of cavities in the brain which are filled with cerebrospinal fluid.

The thickness of the cortical gray matter varies between 1 mm and 4 mm. Inside the gray matter the cells are arranged in six layers. Figure 1.4 illustrates the structure of the gray matter. The two large pyramidal cells in layers 3 and 6 (shown in white) have apical and basal dendrites (Figure 1.2). The layers 1 and 2 contain the apical dendrites, and the basal dendrites are located in layers 3 – 5 of the gray matter [5]. The fissures in the brain cortex are called *sulci*. The rounded areas between the sulci are the *gyri*. The main fissures in the brain subdivide the brain into the frontal, parietal, occipital and the temporal lobes as illustrated in Figure 1.5.

1.1.2 Neurophysiology

Neurophysiology studies the functioning of the nervous system. Most of our consciousness and experiences depend, through some mostly unknown process, on the interaction of the cortical neurons. Most of the electrical potentials that are measured on the scalp is believed to be generated in the cortex. This section investigates the chemical and electrical properties and behavior of the neural cells.

The main task of a neuron is to transport signals. The signals are transmitted through a series of electrical and chemical events. At rest, the intracellular region of a neuron is polarized at -60 mV relative to the extracellular region. The potential difference is caused by the unequal distribution of Na^+, K^+ and Cl^- ions across the cell membrane. This distribution is maintained by active Na^+ and K^+ ion pumps located in the cell membrane. An active neuron releases a chemical substance, called a neurotransmitter at the synapse. The postsynaptic neuron, on the receiving side, contains a large number of receptors at the dendrites and near the cell body that are sensitive to the

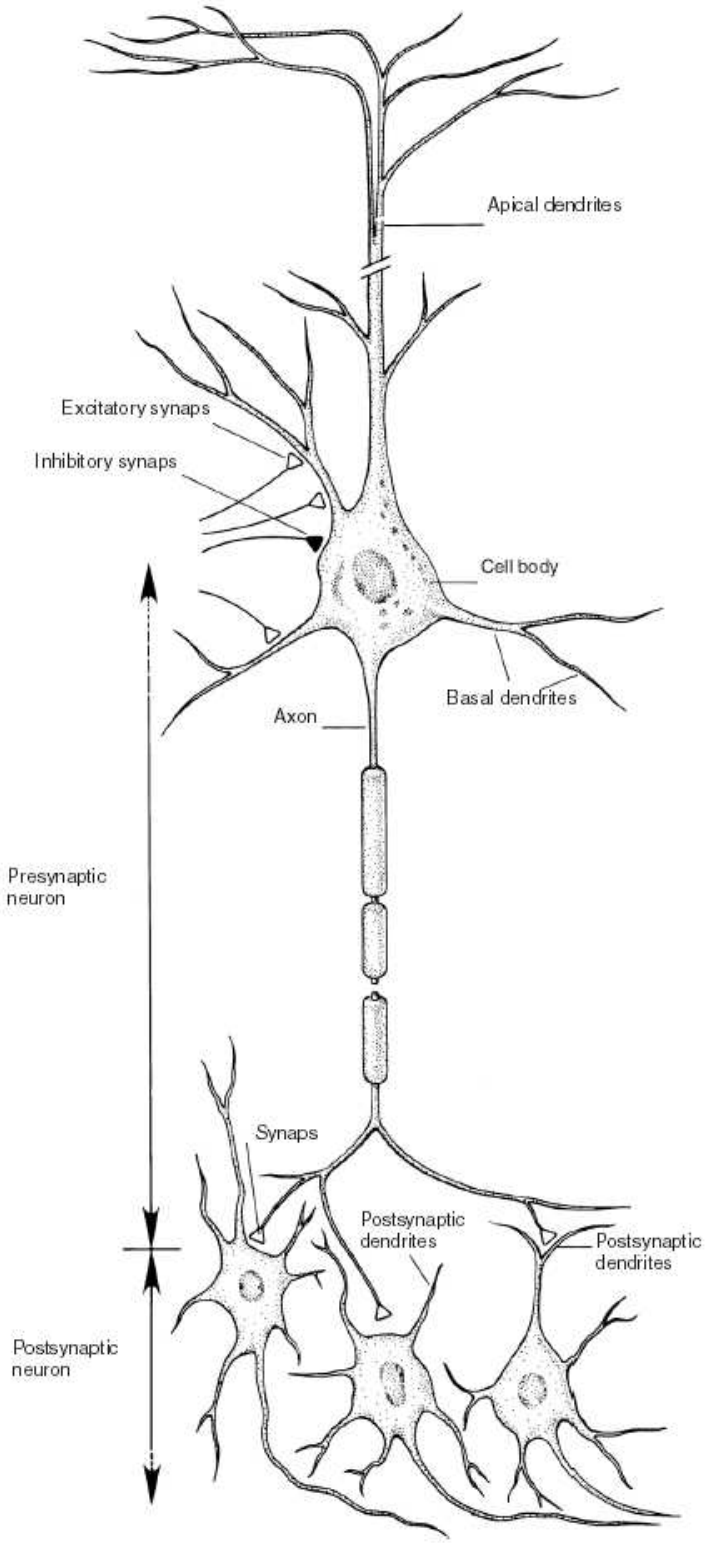

Figure 1.2: The neuron. (This figure is reproduced from [3].)

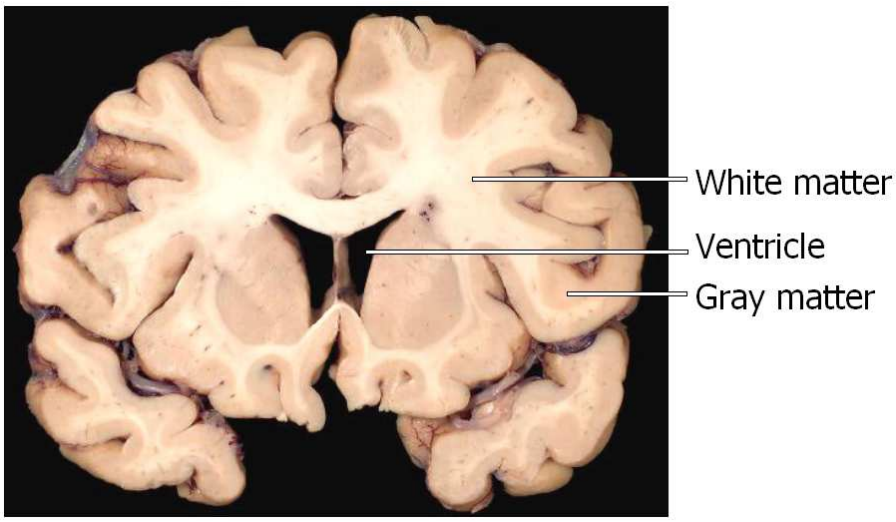

Figure 1.3: A coronal slice of the brain. (This figure is reproduced from [4].)

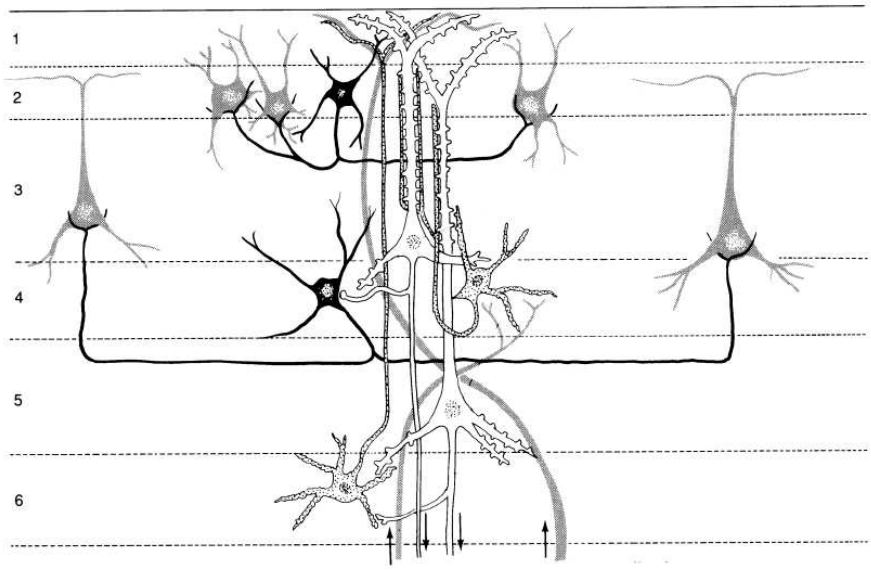

Figure 1.4: The structure of the gray matter. The white cells correspond to pyramidal cells. (This figure is reproduced from [5].)

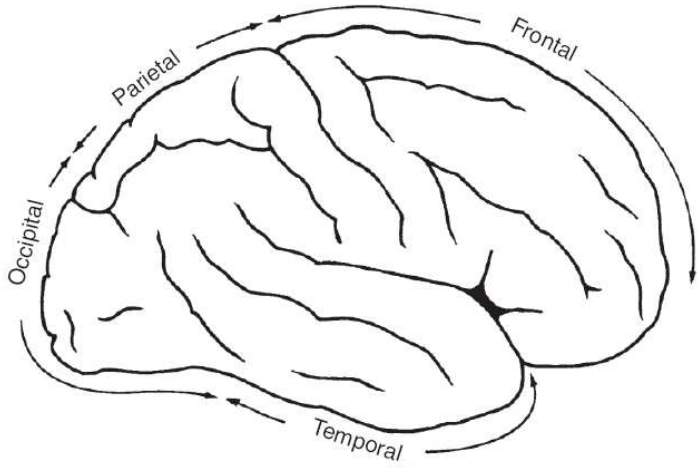

Figure 1.5: The four lobes of the brain. (This figure is reproduced from [5].)

neurotransmitter. The neurotransmitter getting in contact with the receptors changes the permeability of the membrane for charged ions and may cause a depolarization of the membrane, thus triggering an *action potential* [5].

There are two types of synaptic inputs to a neuron. The first type of input produces *excitatory postsynaptic potentials* (EPSPs) across the membrane of the output neuron. This makes it easier for the neuron to fire an action potential. The second type of input is *inhibitory postsynaptic potentials* (IPSPs) which act in the opposite manner on the output neuron. Since there is a large number of presynaptic neurons in contact with a postsynaptic neuron, all the EPSP and IPSP's from the presynaptic neurons are integrated at the cell body. When the net depolarization of the cell body reaches a certain threshold, an action potential is generated that propagates along the axon to other neurons. The excitatory and inhibitory postsynaptic potentials and the generation of an action potential is illustrated in Figure 1.6 [12].

1.2 Electroencephalography

The presence of electrical current in the brain was discovered by an English physician, Richard Caton, in 1875. It was not until 1924 that Hans Berger, a German neurologist, used his ordinary radio equipment to amplify the brain's electrical activity so that he could record it on graph paper [13]. Measurement

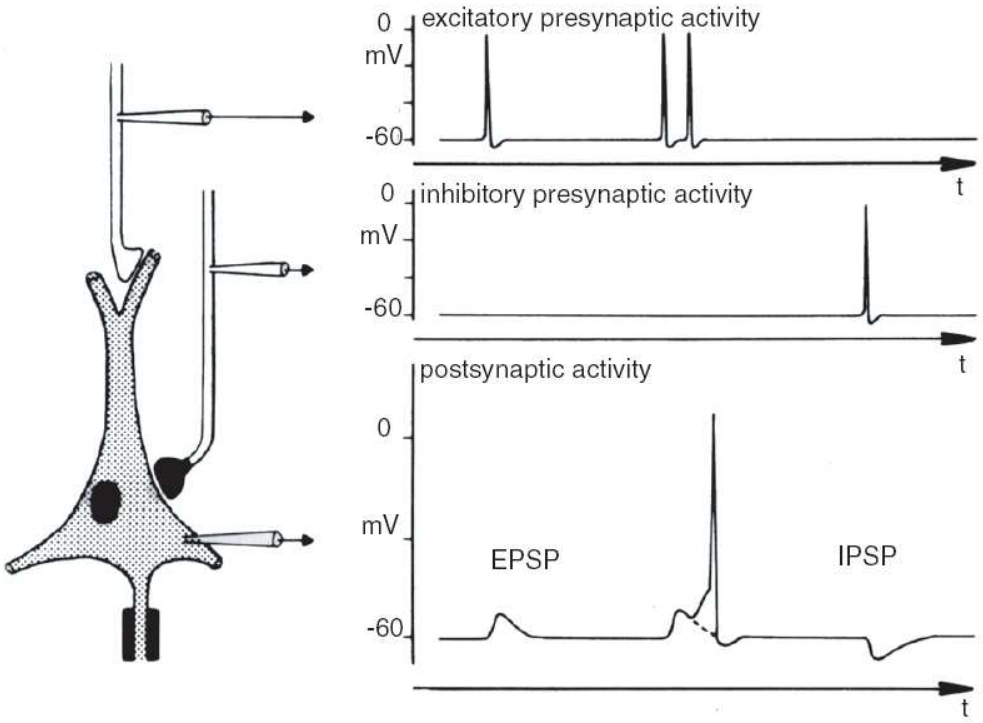

Figure 1.6: An illustration of the excitatory and inhibitory post synaptic potentials. The voltage measurements are presented on the right of the figure. Due to excitatory presynaptic activity, an action potential is depicted. (This figure is reproduced from [6].)

of a set of electric potential differences between pairs of scalp electrodes is called EEG. While the hardware and software continues to improve with the recent technological developments, the basic principle of EEG remains unchanged from Berger's time. For clinical observation, the EEG sensors are attached to the skin at selected locations directly above cortical regions of interest. Alternatively, the sensors may be fitted in an elastic cap for rapid attachment with near uniform coverage of the entire scalp. For research purposes, up to 256 electrodes are used in these setups [14].

A typical EEG recording is shown in Figure 1.7. The recordings are largely due to summed postsynaptic potentials in the many hundreds of thousands of brain neurons that are close to the recording electrodes. While the neural activity is described in terms of action potentials, the contribution of action potentials to the EEG is, in fact, very small. The EEG patterns are complicated waves with large variations in both amplitude and frequency. The wave's amplitude is in the order of microvolts (μV) and indicates how much electrical activity of a similar type is going on beneath the recording electrodes at any given time. The amplitude may range from 0.5 to 100 μV. Note that EEG amplitudes are about 1000 times smaller than an action potential recorded from inside a cell. This difference in amplitude occurs partly because the EEG indicates extracellular potentials, partly because the EEG is recorded through the skull and other brain coverings, and partly because postsynaptic potentials are of lower amplitude than action potentials. The frequency of EEG may vary from 1 to 40 Hz or higher. Four major frequency ranges are found in EEG patterns. In general, lower EEG frequencies indicate less responsive behaviors, such as sleep, whereas higher frequencies indicate states of increased alertness [15].

The reason for the wavelike nature of the EEG, and how it originates is not known. It is currently thought that the thalamus plays a critical role. The clusters of neurons in the thalamus provide a fluctuating output through nerve fibers leading from the thalamus to the cortex. This output causes, in turn, a rhythmic pattern of synaptic activity in the neurons of the cortex. Most of a

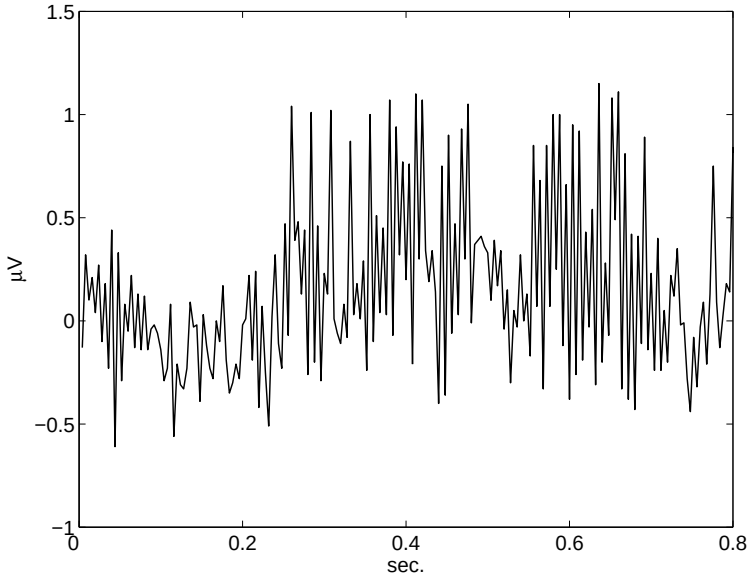

Figure 1.7: A typical EEG pattern of an awake person. This data is obtained using the EEG system in Hacettepe University, Department of Biophysics.

recorded EEG signal consists of cortical synaptic activity [15].

The EEG is a useful clinical tool. It helps in locating the regions of the brain diseased or damaged, for example, by tumors, blood clots, hemorrhage, regions of dead tissue, and high or low blood sugar, since abnormal EEG patterns are observed over these areas. The methods for estimating the location, extent and dynamic behavior of the actual current sources in the brain are currently less widely used in clinical EEG [14]. The aim of most clinical and research applications is to associate the characteristic differences in EEG data with differences in patient populations. For example, *epilepsy* is a common neurological disease which is associated with abnormal synchronized discharges of cerebral neurons. These discharges are reflected in the EEG as a combination of spikes with high amplitude (up to 1000 μV). The EEG can also be helpful in distinguishing confusion caused by overmedication from that caused by a degenerative disease, such as the Alzheimer's disease [15].

Raw EEG measurements provide some clinically useful information, such as the spikes observed in epileptic seizures. However, event-related signals, such as those created by applying a specific sensory stimulus or cognitive experiment, are often lost in background brain activity. It was reported that,

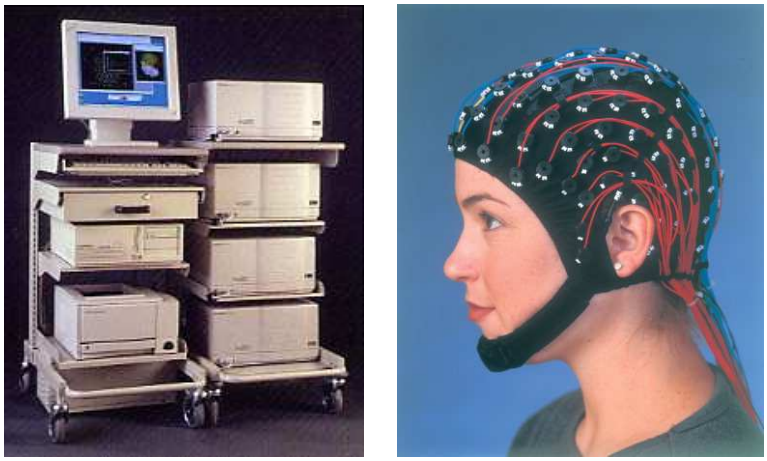

(a) (b)

Figure 1.8: data acquisition system, (a) amplifiers, (b) a 256 channel cap. (These figures are reproduced from [7].)

in 1947, that the background noise can be reduced by combining multiple, *stimulus-locked* EEG recordings of the same stimulus [16]. This technique reveals the event related spatio-temporal components of the EEG signal and is now a standard method for reducing noise in event-related research. However, due to the stochastic nature of the evoked potentials, it was observed that some information was lost when the measurements were averaged. Over the past two decades, statistical methods like principle component analysis, or regularization methods were proposed to extract information from the raw EEG measurements [17].

The characteristics of scalp EEG depend not only on the nature and location of the current sources, but also on the electrical and geometrical properties of the head tissues. The connection between surface and depth events is thus intimately dependent on the physics of electric field behavior in biological tissue. The Section 1.4 will discuss modeling of the geometry and electrical properties of the head can be modeled to extract more accurate information from the EEG recordings.

1.3 Magnetoencephalography

When information is being processed in the brain, small currents that flow in the neural system produce a weak magnetic field. This magnetic field is

extraordinarily weak (compared to the typical EEG scalp potentials), on the order of several tens of femtoTeslas ($\sim 10^{-15}$T), whereas a heartbeat produces a signal in picoTesla ($\sim 10^{-12}$T) and the earth's magnetic field is in the order of tens of microTesla ($\sim 10^{-6}$T). Thus a sophisticated sensing technology is required to measure brain's magnetic field [14].

The MEG measurements are carried out by superconducting quantum interference devices (SQUID), a sensitive detector of magnetic flux, introduced in the late 1960s by James Zimmerman [18]. The first SQUID measurement of the brain was performed at the Massachusetts Institute of Technology by David Cohen [19]. He measured the spontaneous alpha activity of a healthy subject and the abnormal brain activity of an epileptic patient. Evoked responses were first recorded a few years later [20], [21].

Noise is a major concern for MEG. There is instrumental noise and high and low frequency interference from external sources. Using superconducting sensors, and keeping the sensing circuitry in a Dewar cooled with liquid helium minimizes the instrumental noise. High frequency interference is attenuated by the use of shielded rooms made of mu-metal, copper, and aluminum. Low frequency interference caused by moving objects near the MEG system is attenuated by using gradiometers as sensing units. Recent developments in MEG include whole-head sensor arrays for the monitoring of brain magnetic fields at typically 100 to 300 locations.

MEG also has important applications in clinical studies where disease or treatments affect spontaneous or event-related neural activity, like EEG. Stimulus-locked averaging is commonly used to reduce back-ground noise to investigate event-related signals [14].

While EEG is very sensitive to the effects of the secondary or volume currents, MEG is more sensitive to the primary current sources. This was often viewed as an advantage of MEG over EEG. However, it is now widely accepted that EEG and MEG provide complementary information about the underlying brain activity. Thus, EEG and MEG are no longer viewed as competing modalities, and most MEG facilities have equipment for simultaneously ac-

(a) (b)

Figure 1.9: (a) MEG system in a shielded room, (b) An MEG system with the patient and the clinician. The MEG sensors are uniformly distributed over the inner surface of a helmet-shaped dewar. (These figures are reproduced from [8].)

quiring EEG and MEG data.

1.4 Electro-Magnetic Source Imaging

A set of EEG and MEG recordings obtained from an array of sensors provide information about the sources of the underlying brain activity. Using these recordings, it is possible to form an image that represents the distribution of the electrical sources within the brain. When used with event related measurements, these images provide information about the centers of the brain functions related to the experiment. These images are called *electric source image* (ESI) when obtained through EEG measurements, *magnetic source image* (MSI) when MEG measurements are used, and *electro-magnetic source image* when both modalities are used.

In EMSI, the *current dipole model* is traditionally employed to represent the center of simultaneously active neural sources [22]. The aim of EMSI is to construct a source distribution by estimating the spatio-temporal behavior of these dipoles. Before we can make such an estimate, we must first understand and solve the *forward problem* of EMSI, in which the scalp potentials and magnetic fields are solved for a specific dipole configuration. Complementarily, the

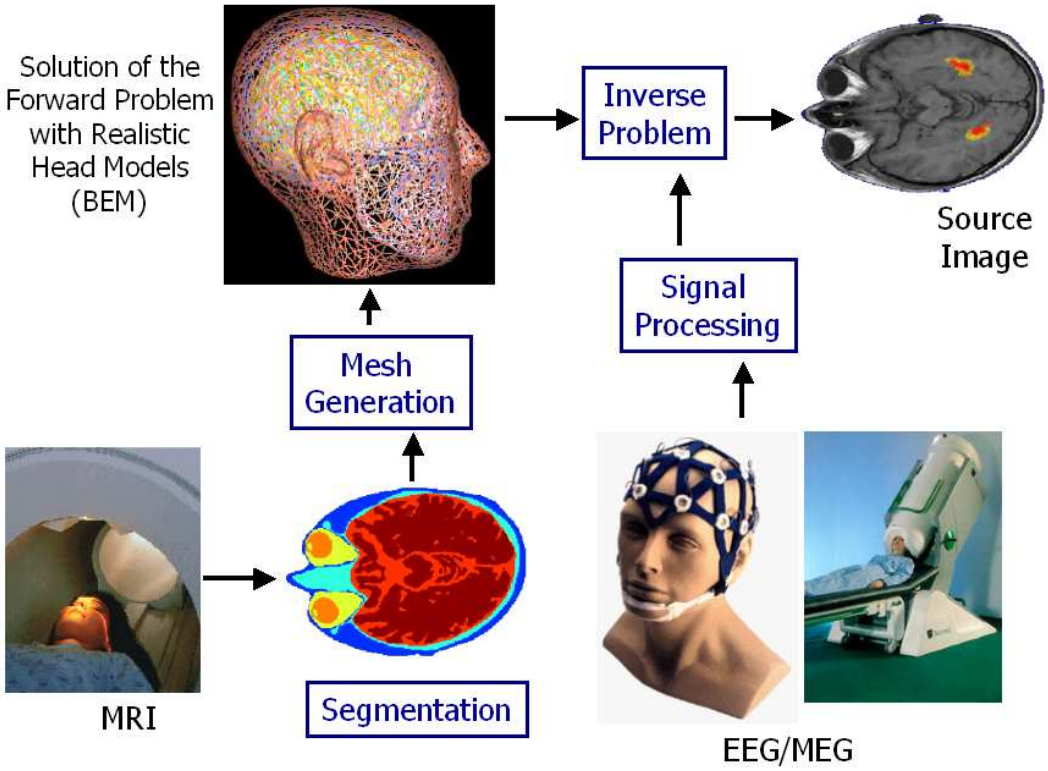

Figure 1.10: Block diagram of Electro-Magnetic Source Imaging.

inverse problem is the localization of the sources based on the measurements and the calculations. Accurate modelling of the human head is necessary to increase the accuracy of EMSI solutions. When the realistic head models are used, a numerical approach must be adopted such as the Boundary Element Method (BEM), the Finite Element Method (FEM), and the Finite Difference Method (FDM). Numerical methods require information about geometrical and electrical properties of the head. This information is usually obtained from segmentation of tomographic images. The segmented volumes are converted to a suitable representation (mesh) needed by the numerical method using a mesh generation process. Head modelling and numerical modelling will be described in detail in the following sub-sections.

Figure 1.10 shows a summary of the EMSI procedure using realistic head models. The geometry information is obtained from tomographic images such as Magnetic Resonance Imaging (MRI) or Computed Tomography (CT) slices using segmentation to determine the tissue boundaries. A volume or a surface mesh suitable for the numerical model is generated from the segmented volume.

In order to use the measurements together with the numerical model, the electrode and sensor positions must be registered with the mesh. Using an inverse problem algorithm, sources are estimated by comparing the EEG/MEG recordings to the forward problem solutions.

The following sub-sections describe various aspects of the EMSI in more detail. First, the source models used in the EMSI are described. Next, various approaches and techniques for modeling the head are introduced. Finally, a brief discussion of inverse problem of the EMSI is discussed. A detailed literature survey on the inverse problem can be found in Chapter 7.

1.4.1 Source Models

The current sources within the human body can be modeled in different ways, depending on the nature of the problem and the model being used. Sources can be modeled as current dipoles, multipole expansions, or distributed current sources such as line, surface or volume current densities [23]. The current dipole model is a popular choice in EMSI studies. The electrical and magnetic field measurements recorded outside the scalp can be represented in terms of multiple current dipoles within the head. Each dipole represents the activity over a small patch of cortex. The brain activity does not actually consist of discrete dipole like activations. The simultaneous activation of pyramidal cells may encompass a larger region of the cortex, requiring multiple dipoles within the region to model the activity. Such activity may be modeled more conveniently by using multipolar models [14]. A dipole is a combination of a current source and a current sink quite close together [24]. Suppose a point source of strength $-I_0$ is placed a small distance, d, away from a point source strength I_0 located at the origin of coordinates. If r is the distance from sink to field point, the total dipole field, Φ_d can be expressed as:

$$\Phi_d = \frac{I_0}{4\pi\sigma}\frac{\partial(1/r)}{\partial d}d. \tag{1.1}$$

The field of two equal and opposite point sources separated by a small distance is called a *dipole field* [24]. The dipole is mathematically defined as

$p = I_0 d$. Then Equation (1.1) can be written as:

$$\Phi_d = \frac{1}{4\pi\sigma} \nabla(1/r) \cdot \vec{p}. \tag{1.2}$$

A dipole has six parameters. Three parameters describe the position of the dipole, orientation is defined by two parameters, and the remaining parameter is the magnitude of the dipole. A typical dipole source, formed by synchronous activity of probably tens of thousands of neurons is 10 nAm [25].

1.4.2 Head Modelling

The solution of the forward problem requires a particular source model, and a head model. Analytic solutions exist for simple head models, such as when the head is assumed to consist of homogeneous spherical shells. To increase accuracy in the solutions, realistic head models are preferred. Use of these models, require numerical methods to solve the forward equations. In this section, a historical development of head modelling and most widely used numerical methods and their properties are explained.

1.4.2.1 Simple Head Models

The first volume conductor models of the human head consisted of homogeneous conductors (sphere and spheroids) that have analytical solutions for the electric and magnetic fields [26]. Geselowitz and Grynszpan studied analytical formulations of potentials and magnetic fields for current dipoles placed inside a sphere [27] [28]. Analytical solutions for the electrical and magnetic fields produced by current dipoles inside prolate spheroid (egg-shape) and oblate spheroid (discus-shape) are presented in [29], [30], and [31]. However it was soon noticed that the skull had a conductivity which was significantly lower than the conductivity of the scalp and the brain tissue. Therefore the volume conductor model of the head needed further refinement. Three or four layer concentric spherical head models were introduced, in order to represent layers like skull, scalp and cerebrospinal fluid (CSF). For these geometries the analytical solution of the forward problem is presented in [32]. For magnetic fields, it

was shown that the concentric spheres model is equivalent to the homogeneous spheres model [27]. It was also mentioned that there are analytical solutions available for layered spheroidal volume conductors [33].

Many researchers have investigated the accuracy and performance of simple head models that have analytical solutions for the potential and magnetic fields on source localization. Solutions on experimental data and solutions using constructed head models have been compared. The results have shown that the use of simple head models can yield significant errors in source localization. Henderson *et al* [34], compared the localization using a saline-filled conductor and a spherical model, and obtained 1 cm localization error. Cohen *et al* [35], measured the localization performance of EEG and MEG data using implanted sources in human brain, and a spherical head model for reconstructing source locations. They computed average localization errors as as 8 mm for MEG, and 10 mm for EEG. It was stated in [36], that a spherical model was insufficient for localizing the sources implanted in a human skull using MEG data. Weinberg *et al* [37], also used a human skull with implanted sources, and modelled the skull as a collection of 25 spheres and obtained 3.5 mm localization error. Zhang *et al* showed that when two dipoles were simultaneously active shell model misspecification may produce large errors in the estimation of dipole parameters using single time or multiple-time points in source localization [38], [39].

Conductivity inhomogeneities of the head were simulated using concentric and eccentric spheres model of the head [32], [40], [41], [42], [43], [44], [45]. Ueno *et al* investigated the effects of inhomogenieties using spherical models, and showed that EEG and MEG measurements are significantly affected when there is an inhomogeniety close to the source [46], [47]. In addition to the accuracy of the head model, there are a lot of other factors such as measurement noise, registration of sensor and/or electrode positions and the choice of the source model which affect the localization performance.

The main advantage of simple head models is the speed of computations. Using these models, the inverse problem can be solved with minimal computer

resources. Therefore, these models are routinely used in most clinical and research applications on MEG/EEG source localization.

1.4.2.2 Realistic Head Models

In the previous section, the studies using head models consisting a set of nested concentric or eccentric homogeneous and isotropic spheres have been described. In reality, of course, we do not have heads like this. Our heads are anisotropic, inhomogeneous, and not spherical.

More accurate solutions in EMSI use anatomical information obtained from high-resolution volumetric brain images obtained with magnetic resonance (MR) and/or X-ray computed tomography (CT) imaging. Different tissues can have different voxel intensities. It is possible to divide the image in several regions having the same voxel intensity. This process is called *segmentation* of medical images. The segmented volumes can then be included in a numerical method for the calculation of the forward fields.

In EMSI studies, the most widely used numerical methods are the BEM [48], [49], [50], [51], [52], the FEM [53], [54], [55], [56] and the FDM [57], [58]. They all can be used to solve the forward problem of EEG/MEG source analysis in a realistic head model. The major differences between the three methods can be summarized as follows. In the BEM, the solutions are calculated on the boundaries between the homogenous isotropic conducting regions. On the other hand, in the FEM and the FDM the solution of the forward problem is calculated in the entire volume. Subsequently, the FEM and FDM lead to a larger number of computational points than the BEM which increases the number of computations. While the BEM computations are usually faster, BEM assumes homogeneity and isotropy within each region of the head.

Conventional methods of calculating the forward problem using the numerical methods are very time consuming. When incorporated as part of an inverse solution, they may seem even more impractical. However, through use of fast numerical methods, precalculation, look-up tables, and interpolation of the precalculated fields, both the FEM and the BEM can be made efficient for

applications in MEG and EEG [59], [60], [61], [62].

Realistic modeling of the human head is necessary to increase the accuracy of EMSI solutions. Roth *et al* [63], Crouzeix *et al* [64], and Cuffin [45] investigated dipole localization accuracy using spherical and realistic meshes. It was shown that a realistic model improves the localization accuracy on the order of 1-2 cm. However, their realistic models have only three tissue types, namely, the scalp, skull and the brain. Ramon *et al* [65] examined the effects of soft skull bone, cerebrospinal fluid (CSF) and gray matter on scalp potentials using the finite element method (FEM). They observed that the scalp potentials were significantly affected by these tissues. Thus, the accuracy in source localization can further be improved if more realistic head models are used in the forward problem solutions.

1.4.3 Inverse Problem

An essential part of obtaining EMSIs is the solution of the electric and magnetic fields (the forward problem) for a given source configuration assuming a head model. The solution of the inverse problem (i.e., given the measured data, finding the location and direction of dipoles) is based on the comparison of the measured and calculated fields.

The inverse problem solution is complicated by the fact that a number of source configurations may give rise to the same potential distributions over the scalp [66]. On the other hand, different field distributions can only be achieved by different sources. The only way to eliminate the non-uniqueness of the problem is to select a priori models for both head and underlying sources. Various mathematical, biophysical, statistical, anatomical, functional limits have been proposed over the years to reduce the uncertainity in the inverse problem solution. As more appropriate a priori models are used, the information about the sources will be more reliable.

The literature on source localization is diverse and rich. The suggested methods range from genetic algorithms to artificial neural networks. The inverse problem methods are usually investigated under two main categories:

the parametric methods and the imaging methods [14], [67], [68].

The choice of the inverse problem algorithm is not the only criteria for a successful source localization. The choice of the a priori model, the position and number of sensors, the position of the reference electrode for EEG, the numerical head model, registration of the head model with measurements, and the selected inverse problem algorithm all affect the localization performance. These issues are discussed extensively in Chapter 7.

1.5 Purpose of the Thesis

The purpose of this thesis is to build an efficient and accurate source localization framework using the BEM. To build and test this framework, the following items have been accomplished:

Increasing the accuracy of the existing BEM formulation : In a previous study, Gençer and Tanzer [51] have proposed the use of high-order isoparametric elements to increase the accuracy in the solutions. In this study, the accuracy in the BEM solutions is further improved by applying the recursive integration technique [69]. The new BEM implementation allows the use of quadratic elements with realistic head models and is capable of handling intersecting surfaces, like skull and eyes. The isolated problem approach (IPA) [49], [48], which is a technique to improve the accuracy of the solutions in the presence of the low conductivity skull layer, have been generalized to use with complex BEM models [70].

Improving the efficiency of the BEM computations : To decrease the computation time, two new formulations are presented for the calculation of EEG and MEG transfer matrices that relate the sources to the fields at the sensor locations. By pre-computing the transfer matrices, forward solutions for electric and magnetic fields are reduced to simple matrix-vector multiplications. This method offers improved computational speed and lower storage requirements. The IPA is also integrated into the algorithms [59].

Generating more accurate head meshes : For realistic head modeling, a hybrid segmentation algorithm is developed to obtain scalp, skull, gray matter (GM), white matter (WM), eyeballs and the surrounding tissue of the eyes from multimodal (T_1–, T_2–weighted and proton density (PD)) MR images. A realistic head model is generated using quadratic isoparametric elements. Using a novel mesh generation approach, it is possible to model complex geometries such as the intersecting skull and eye boundaries [59].

Accurate registration of EEG data with the BEM mesh : An important consideration that affects the accuracy of EMSI experiments is the mapping of electrode and sensor positions on to the realistic head model. For this purpose, an optimization algorithm have been implemented [71] to map digitized electrode coordinates onto the BEM mesh.

Implementation of genetic algorithms : There is a wide array of approaches and algorithms for solving the inverse problem of EMSI. In this work, genetic algorithm (GA) which is a global optimization technique is implemented for solving the inverse problem. Different GA operations have been tested and GA has been merged with local optimization algorithms to improve the convergence speed of the inverse problem.

Source localization using experimental data : To test the EMSI framework on real data, an auditory experiment have been conducted. The acquired EEG data have been mapped onto the head model and the source distribution at the peak of the recorded data have been investigated.

1.6 Thesis Outline

This thesis consists of six chapters describing the main components of the EMSI solution framework. Chapter 2 introduces the BEM and presents new formulations for calculating the transfer matrices. This chapter explains how the accuracy of the BEM solutions with realistic head models are increased

and the efficiency of the BEM computations are improved. The next chapter introduces a generalized formulation and implementation of the IPA for multi-compartment BEM models. For realistic head modeling, the adopted segmentation and mesh generation approaches are described in Chapters 4 and 5. The registration of EEG and MR data from digitized electrode positions is described in Chapter 6. Finally the inverse problem approach, namely the genetic algorithms are described in Chapter 7. The results with simulated and experimental data are presented.

Since the chapters are self-contained, each chapter starts with an introduction and a literature survey, followed by the description of the work and related algorithms. The results relevant to each chapter are presented at the end of the chapter itself. The conclusion and discussion of this work is presented as a final Chapter 8. Previous BEM formulation proposed by Gençer and Tanzer [51] is given in the Appendix.

CHAPTER 2

AN ADVANCED BOUNDARY ELEMENT METHOD IMPLEMENTATION

2.1 Introduction

Localization of the brain activities using the electroencephalography and magnetoencephalography measurements is called electro-magnetic source imaging [14], [72], [73], [74]. The *forward problem* of EMSI is the solution of the scalp potentials and magnetic fields due to a given source configuration. To solve the potential distribution due to electrical sources in the brain, various numerical methods have been used. For compartmental models of the head, the Boundary Element Method is frequently employed. This chapter focuses on 1) increasing the accuracy of the BEM solutions with realistic head models and 2) improving the efficiency of the BEM computations.

To increase the numerical accuracy in the solutions either the numerical formulation is improved or the quality of the meshes used in the calculations is increased. The numerical error caused by high conductivity difference between the skull and brain layer is reduced using the modified equations, as given in the isolated problem approach [48], [49]. The use of high-order elements (quadratic, cubic) in the BEM formulations [69], [75], [51] and the method of recursive integration [69] also increase the accuracy. While the advantages of high-order elements and recursive integration were shown by concentric spherical-shell head models they have not been applied to realistic head geometries. This study uses both high order elements and recursive

integration with realistic head models.

When realistic head models are used, the forward problem computation time increases considerably. Usually a pre-computation phase, such as inverting or decomposing the BEM coefficient matrix is necessary to reduce the time for the individual dipole solutions. One obvious way to reduce the computation time is to solve the potentials only at the electrode positions. Thus, a transfer matrix relating the source distribution to the potentials on the electrode locations is computed. Several researchers have exploited this idea but their approaches differed in the computation of the transfer matrix. Cuffin calculated the transfer matrix using the power series expansion of the BEM coefficient matrix [50]. Fletcher *et al* obtained the transfer matrix by first computing the true inverse of the coefficient matrix in the BEM formulation and selecting the corresponding rows [76]. Similarly, Fuchs *et al* computed the transfer matrix by first obtaining the LU decomposition of the coefficient matrix [77]. This study, introduces, for the first time, a method to calculate the transfer matrix for the solution of the magnetic fields at the sensor locations [59].

An alternative approach for decreasing the computation time is to precompute the solutions over a grid of dipoles covering the brain volume. The solutions for an arbitrary source configuration are then obtained using interpolation [61], [62]. However, when this technique is employed, the density of grid points and the choice of interpolation function determine the accuracy in solutions; increasing the density of grid points also increases the pre-computation time.

Recently, the inhomogeneities in the skull layer were modelled. Oostenveld and Oostendorp [78] compared the accuracy of the BEM and the FDM solutions for a head geometry with a hole in the skull. The effects of holes and other inhomogeneities in the skull were also investigated by Benar and Gotman [79]. Both of these studies concluded that such defects should be included in the model to improve the accuracy. However, they have not provided a general method for modelling such complex geometries. Through a novel mesh

generation approach, this study makes it possible to model intersecting tissue compartments using BEM.

The next section introduces the BEM and presents new formulations for calculating the transfer matrices. First, the matrix equations are presented for the solution of the potential and magnetic fields using BEM. Then, the transfer matrix formulations are derived that incorporate the IPA when there is a single layer inside the skull. For more complex models the formulations for the transfer matrix formulations are given Chapter 3. The original BEM formulation derived by Gençer and Tanzer is given in the Appendix for completeness [51].

Several properties of the new BEM formulation is investigated and validated in the results section. The effect of recursive integration is shown using a spherical head model, and the use of intersecting tissue boundaries is validated comparing the forward problem solutions of a BEM and a FEM model. The sensitivity of measurements to eye conductivity is presented using this model. Finally, the computational performance of the forward problem solution is presented.

2.2 BEM Formulation

The electric potential ϕ and the magnetic field $\vec{B}$ due to a current dipole source $\vec{p}$ in a piecewise homogeneous volume conductor model of the head, satisfy the following integral equations [80]:

$$\bar{\sigma}\phi(\vec{r}) = g(\vec{r}) + \frac{1}{4\pi}\sum_{k=1}^{L}(\sigma_k^- - \sigma_k^+)\int_{S_k}\phi(\vec{r}\,')\frac{\vec{R}}{R^3}\cdot d\vec{S}_k(\vec{r}\,'), \tag{2.1}$$

$$\vec{B}(\vec{r}) = \vec{B}_0(\vec{r}) + \frac{\mu_0}{4\pi}\sum_{k=1}^{L}(\sigma_k^- - \sigma_k^+)\int_{S_k}\phi(\vec{r}\,')\frac{\vec{R}}{R^3}\times d\vec{S}_k(\vec{r}\,'). \tag{2.2}$$

Here, the surfaces between different conductivity regions are denoted by S_k, $k = 1 \ldots L$. The inner and outer conductivities of S_k are represented by σ_k^- and σ_k^+, respectively. $\vec{R} = \vec{r} - \vec{r}\,'$ is the vector between the field point $\vec{r}$ and the source point $\vec{r}\,'$, R is the magnitude of $\vec{R}$, and $\bar{\sigma}$ is the mean conductivity at

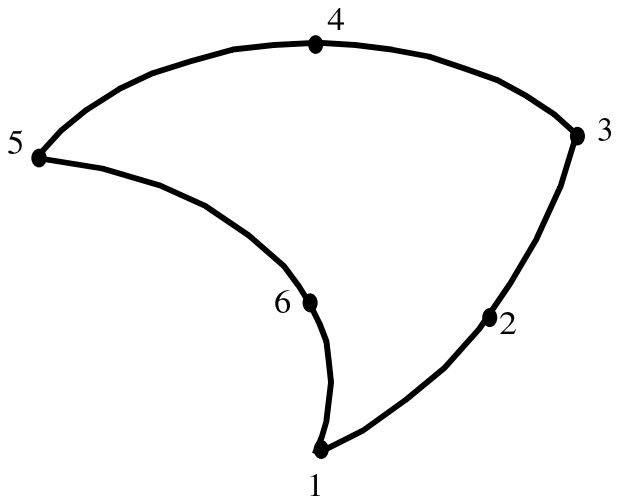

Figure 2.1: A 6-noded triangular, quadratic and isoparametric BEM element.

the field point. The contribution of the primary sources g and $\vec{B}_0$ are defined as follows:

$$g(\vec{r}) = \frac{1}{4\pi\sigma_0}\frac{\vec{p}\cdot\vec{R}}{R^3}, \tag{2.3}$$

$$\vec{B}_0(\vec{r}) = \frac{\mu_0}{4\pi}\frac{\vec{p}\times\vec{R}}{R^3}, \tag{2.4}$$

where σ_0 represents the unit conductivity and μ_0 is the permeability of the free space. The second terms in Equation (2.1) and Equation (2.2) can be solved numerically by discretizing the surfaces into elements and computing the surface integrals over these elements [80], [81], [82], [83]. In most studies, the elements are chosen as plane triangles on which the potential has either constant or linear variation. A review of these studies have been reported by Ferguson and Stroink [84]. In this study, triangular, quadratic and isoparametric BEM elements (Figure 2.1) are used for discretizing the surface [51]. Integrating Equation (2.1) over all elements, a set of equations are obtained. In matrix notation, this can be expressed as:

$$\Phi = \mathbf{g} + \mathbf{C}_0\Phi \tag{2.5}$$

where Φ is an $N \times 1$ vector of node potentials and N is the number of nodes in the whole BEM mesh. $\mathbf{C}_0$ is an $N \times N$ matrix whose elements are determined by the geometry and electrical conductivity of the head and $\mathbf{g}$ is an $N \times 1$

vector representing the contribution of the primary sources. To eliminate the singularity in the solution of Equation (2.5), the method of matrix deflation is employed [85]. The deflated matrix $\mathbf{C}$, can be calculated from $\mathbf{C}_0$ as below:

$$\mathbf{C}_{ij} = \mathbf{C}_0 - \frac{1}{N} e_i e_j^T \tag{2.6}$$

where e_i is an identity vector with its ith component equal to one and T denotes the transpose. If $\mathbf{I}$ denotes the $N \times N$ identity matrix, then

$$\begin{aligned} \Phi &= (\mathbf{I} - \mathbf{C})^{-1}\mathbf{g} \\ \Phi &= \mathbf{A}^{-1}\mathbf{g}. \end{aligned} \tag{2.7}$$

Here, $\mathbf{A}$ represents $(\mathbf{I} - \mathbf{C})$. After calculating Φ, $\vec{B}$ is computed using Φ through Equation (2.2). The expression for the magnetic field can be written in matrix notation as

$$\mathbf{B} = \mathbf{B}_0 + \mathbf{H}\Phi. \tag{2.8}$$

In the above expression, $\mathbf{B}$ is an $n \times 1$ vector representing the magnetic fields at the sensor locations and n is the number of magnetic sensors. $\mathbf{B}_0$ denotes the $n \times 1$ vector of magnetic fields at the same sensor locations for an unbounded homogenous medium. $\mathbf{H}$ is an $n \times N$ coefficient matrix determined by the geometry and electrical conductivity of the head.

When the compartment surfaces are close to each other, or when the source is close to a surface (closer than the element size), numerical errors are observed. To overcome this problem, the recursive integration technique was proposed [69]. In the recursive integration, the surface elements are divided into sub-elements and the numerical integration is performed on each sub-element. This process is repeated recursively until a subdivision criterion is met. Since the potential field is calculated at the original nodes, the size of the BEM matrix equation remains the same, but the accuracy of the surface integral is improved.

The head models used for the BEM implementations in the literature were constructed using non-intersecting layers that represent the main tissues, i.e., the scalp, skull, and the brain. In these models, the eyes and the eye-holes

in the skull were neglected to simplify the mesh generation and the BEM implementation. More complex head models have been studied to investigate the skull defects and holes in the skull. However, to model a skull with a hole, either a thin closed surface was used to represent the skull layer [79] or a different conductivity region was defined in the skull leading to infinitely thin layers between skull and hole regions [78]. To use a better head model in the numerical solutions, one must generate a BEM mesh that correctly defines the boundaries of different conductivity regions. A mesh generation algorithm that handles such cases will be presented in Chapter 5.

2.3 Accelerated BEM for EEG

This section introduces a novel approach for computing the node potentials on a small subset of nodes corresponding to the electrode positions. This approach pre-calculates and stores relevant matrices, providing a significant decrease in the computation time for a given source configuration.

Let us assume that each electrode corresponds to a node in the BEM mesh. If m is the number of electrodes, then the electrode potentials can be written as

$$\Phi_e = \mathbf{E}\mathbf{g} \tag{2.9}$$

where Φ_e is an $m \times 1$ vector of electrode potentials and $\mathbf{E}$ is the $m \times N$ *transfer matrix* for the electric field.

Let the transfer matrix $\mathbf{E}$ be defined as:

$$\mathbf{E} = \mathbf{D}\mathbf{A}^{-1}. \tag{2.10}$$

where $\mathbf{D}$ is an $m \times M$ sparse matrix to select m rows of $\mathbf{A}^{-1}$. Note that, if the rows of $\mathbf{A}^{-1}$ is computed and stored, then Φ_e can be calculated by a simple matrix-vector multiplication for any source vector $\mathbf{g}$. To obtain the rows of $\mathbf{A}^{-1}$ the following approach is used. Taking the transpose of both sides of Equation (2.10) we obtain,

$$\mathbf{E}^T = (\mathbf{A}^{-1})^T\mathbf{D}^T. \tag{2.11}$$

Using the identity $(\mathbf{A}^{-1})^T = (\mathbf{A}^T)^{-1}$, and multiplying both sides with $\mathbf{A}^T$, it is possible to obtain

$$\mathbf{A}^T\mathbf{E}^T = \mathbf{D}^T. \tag{2.12}$$

Thus, the i^th column vector $\mathbf{e}_i$ of $\mathbf{E}^T$ can be obtained using the following equation:

$$\mathbf{A}^T\mathbf{e}_i = \mathbf{d}_i \tag{2.13}$$

here $\mathbf{d}_i$ is the ith column of $\mathbf{D}^T$. Thus the $\mathbf{E}$ matrix (i.e., the required rows of $\mathbf{A}^{-1}$) can be computed using Equation (2.13) with m different right-hand side vectors $\mathbf{d}_i$.

In this study, the accelerated BEM approach is also extended to incorporate the IPA for a three layer head model. Let the surfaces S_1, S_2, and S_3 represent the scalp, skull and brain surfaces in a three-layer head model, respectively. Then, Equation (2.5) can be expressed in block matrix form as follows:

$$\begin{bmatrix} \Phi_1 \\ \Phi_2 \\ \Phi_3 \end{bmatrix} = \begin{bmatrix} \mathbf{C}_{11} & \mathbf{C}_{12} & \mathbf{C}_{13} \\ \mathbf{C}_{21} & \mathbf{C}_{22} & \mathbf{C}_{23} \\ \mathbf{C}_{31} & \mathbf{C}_{32} & \mathbf{C}_{33} \end{bmatrix} \begin{bmatrix} \Phi_1 \\ \Phi_2 \\ \Phi_3 \end{bmatrix} + \begin{bmatrix} \mathbf{g}_1 \\ \mathbf{g}_2 \\ \mathbf{g}_3 \end{bmatrix} \tag{2.14}$$

where the potentials on the corresponding surfaces are denoted by Φ_1, Φ_2, and Φ_3. The ratio of the conductivities across S_3 can be defined as $\beta = \frac{\sigma_2}{\sigma_3}$, where σ_2 and σ_3 are the conductivities of the second and the third layers, respectively. If $\beta \ll 1$, then Φ_1 and Φ_2 are much smaller than Φ_3 in magnitude causing numerical errors in matrix solutions. When IPA is applied, the source terms are modified as [49]:

$$\mathbf{g}' = \begin{bmatrix} \mathbf{g}'_1 \\ \mathbf{g}'_2 \\ \mathbf{g}'_3 \end{bmatrix} = \begin{bmatrix} \beta\mathbf{g}_1 \\ \beta\mathbf{g}_2 \\ \beta\mathbf{g}_3 - \frac{2\sigma_2}{\sigma_2+\sigma_3}\Phi_3^0 \end{bmatrix}, \tag{2.15}$$

and the resulting potentials can be written as

$$\Phi' = \mathbf{A}^{-1}\mathbf{g}' = \begin{bmatrix} \Phi'_1 \\ \Phi'_2 \\ \Phi'_3 \end{bmatrix} = \begin{bmatrix} \Phi_1 \\ \Phi_2 \\ \Phi_3 - \Phi_3^0 \end{bmatrix}. \tag{2.16}$$

In equations Equation (2.15) and Equation (2.16), Φ_3^0 is the potential on the surface S_3 when the head is represented by a homogeneous brain region (i.e., the skull and scalp layers are omitted). Φ_3^0 can be obtained from

$$\Phi_3^0 = (\mathbf{A}_s)^{-1}\mathbf{g}_3^0 \tag{2.17}$$

where $\mathbf{A}_s$ is in the form of $(\mathbf{I} - \mathbf{C'_{33}})$ and $\mathbf{g}_3^0$ is the corresponding source term. Here, the matrix $\mathbf{C'_{33}}$ is the scaled and deflated version of $\mathbf{C_{33}}$ (Hämäläinen and Sarvas 1989).

As a result, the accelerated approach for potential field calculations using IPA starts with the calculation of the transfer matrix $\mathbf{E}$ and $\mathbf{A}_s$. Once these matrices are computed and stored, the potentials due to an arbitrary source configuration can be obtained as follows: 1) Φ_3^0 is computed using Equation (2.17), 2) $\mathbf{g'}$ is calculated using Equation (2.15), and 3) Φ_e is solved using Equation (2.9).

2.4 Accelerated BEM for MEG

An accelerated approach can also be developed to obtain magnetic fields. To calculate the magnetic field at the sensor locations from Equation (2.8), the potential field at all nodes is used. However, since

$$\mathbf{H}\Phi = \mathbf{H}\mathbf{A}^{-1}\mathbf{g}, \tag{2.18}$$

equation Equation (2.8) can be rewritten as

$$\mathbf{B} = \mathbf{B_0} + \mathbf{M}\mathbf{g} \tag{2.19}$$

where

$$\mathbf{M} = \mathbf{H}\mathbf{A}^{-1}. \tag{2.20}$$

The $\mathbf{M}$ matrix is the $n \times N$ *transfer matrix* which relates the source vector $\mathbf{g}$ to the magnetic field measurements. $\mathbf{M}$ can be pre-computed using the same technique as given in equations Equation (2.11) and Equation (2.12). Thus, the i^th column vector $\mathbf{m}_i$ of $\mathbf{M}^T$ can be obtained using the following equation:

$$\mathbf{A}^T\mathbf{m}_i = \mathbf{h}_i \tag{2.21}$$

here $\mathbf{h}_i$ is the ith column of $\mathbf{H}^T$. Once $\mathbf{M}$ is computed and stored, the magnetic field for an arbitrary source configuration can be solved without computing the potentials at all nodes.

This method can also be extended to be used with the IPA. When IPA is applied, the potentials are modified as follows:

$$\Phi' = \Phi - \Phi'' \tag{2.22}$$

where Φ and Φ' are as given in equations Equation (2.14) and Equation (2.16), and Φ'' is defined as

$$\Phi'' = \begin{bmatrix} 0 \\ 0 \\ \Phi_3^0 \end{bmatrix}. \tag{2.23}$$

Then, equation Equation (2.8) can be rewritten as:

$$\begin{aligned} \mathbf{B} &= \mathbf{B}_0 + \mathbf{H}(\Phi' + \Phi'') \\ &= \mathbf{B}_0 + \mathbf{H}\Phi' + \mathbf{H}\Phi'' \\ &= \mathbf{B}_0 + \mathbf{H}\mathbf{A}^{-1}\mathbf{g}' + \mathbf{H}\Phi'' \end{aligned} \tag{2.24}$$

Since Φ'' is zero for the first and the second layers we can write $\mathbf{H}\Phi''$ as

$$\mathbf{H}\Phi'' = [\mathbf{H}_1\ \mathbf{H}_2\ \mathbf{H}_3] \begin{bmatrix} 0 \\ 0 \\ \Phi_3^0 \end{bmatrix} = \mathbf{H}_3\Phi_3^0 \tag{2.25}$$

Therefore, Equation (3.14) becomes

$$\mathbf{B} = \mathbf{B}_0 + \mathbf{M}\mathbf{g}' + \mathbf{H}_3\Phi_3^0. \tag{2.26}$$

As a result, to obtain fast magnetic field solutions, first the matrices $\mathbf{M}$, $\mathbf{H}_3$, and $\mathbf{A}_s^{-1}$ are computed and stored. After this pre-computation stage, the solutions for arbitrary source configurations can be obtained using Equation (3.16) with simple matrix-vector multiplications.

2.5 Results

Several properties of the new BEM formulation is investigated and validated in the results section. The effect of recursive integration is shown using a

spherical head model, and the use of intersecting tissue boundaries is validated comparing the forward problem solutions of a BEM and a FEM model. The sensitivity of measurements to eye conductivity is presented using a realistic model constructed in Chapters 4 and 5. Finally, the computational performance of the forward problem solution is presented for this model.

2.5.1 Increasing accuracy using the recursive integration

The BEM formulation used in this work was previously used to test the accuracy for a concentric three-spheres model [51]. The radius of the spheres were 10, 9, and 8 cm with conductivities 0.2, 0.005, and 0.2 S/m, respectively. The analytical (V') and numerical (V) solutions were compared using the relative difference measure (RDM) and RDM* [48]:

$$\%\text{RDM} = \left(\frac{\sum_{i=1}^{m} (V_i' - V_i)^2}{\sum_{i=1}^{m} (V_i'^2)} \right)^{1/2} \times 100, \tag{2.27}$$

$$\text{RDM*} = \left(\sum_{i=1}^{m} \left[\frac{V_i'}{\sqrt{\sum_{i=1}^{m} (V_i'^2)}} - \frac{V_i}{\sqrt{\sum_{i=1}^{m} (V_i^2)}} \right]^2 \right)^{1/2}, \tag{2.28}$$

For a specific mesh with second-order elements, the computed RDMs were found to be less than 2% for both potential and magnetic field solutions. However, it is observed that, as the conductivity ratio between the skull and the brain (β) decreases and/or the layers get close to each other, the numerical error in the solutions increases. To assess the numerical method for such a case, the 3-layer spherical Rush and Driscoll model [86] is used. In this model, the radii of the spheres are 9.2, 8.5, and 8 cm, and the conductivities are 0.2, 0.0025, and 0.2 S/m, respectively. Thus the thickness of the inner layer and β for this model are smaller compared to the three-spheres model used in the

previous study [51].

The BEM mesh used in the simulations has 512 elements and 1026 nodes per layer. Note that, this yields element edge sizes larger than the skull thickness, thus numerical errors must be expected. Using this mesh, the previous BEM implementation generates RDMs on the order of $20-30\%$ for tangential dipoles located on the z-axis. The maximum error occurs when the dipole is located 2 mm below the skull layer. To improve the accuracy in solutions, the recursive integration technique is employed [69]. When one-step recursive integration is applied, the maximum RDM decreases to 2.2%. The RDMs slightly decrease for further iterations. Since the effect of the secondary magnetic fields is low on concentric spheres model, the change in the magnetic field due to recursive integration is less than 1%.

2.5.2 Validation of the intersecting meshes

The BEM implementation that uses intersecting meshes is tested using the model shown in Figure 2.2. The model is based on the concentric three-spheres model with an additional inhomogeneity intersecting the outer skull layer to model a single eye. Since an analytical solution is not possible for such a head geometry, the numerical solutions are compared with the results obtained by FEM [74], [87], [88].

For comparison, first a FEM mesh is constructed and the elements that are on the conductivity boundaries in the FEM model are used to create the BEM mesh. The RDMs are calculated for 9 dipoles located radially and tangentially at different depths. The tests are performed for five cases assigning different

Table 2.1: Conductivities (in S/m) of the tissues in Figure 2.2 for 5 different cases.

	scalp (1)	skull (2)	brain (3)	eye (4)
case 1	0.2	0.2	0.2	0.2
case 2	0.2	0.2	0.4	0.2
case 3	0.3	0.1	0.2	0.2
case 4	0.2	0.2	0.2	0.5
case 5	0.2	0.005	0.2	0.5

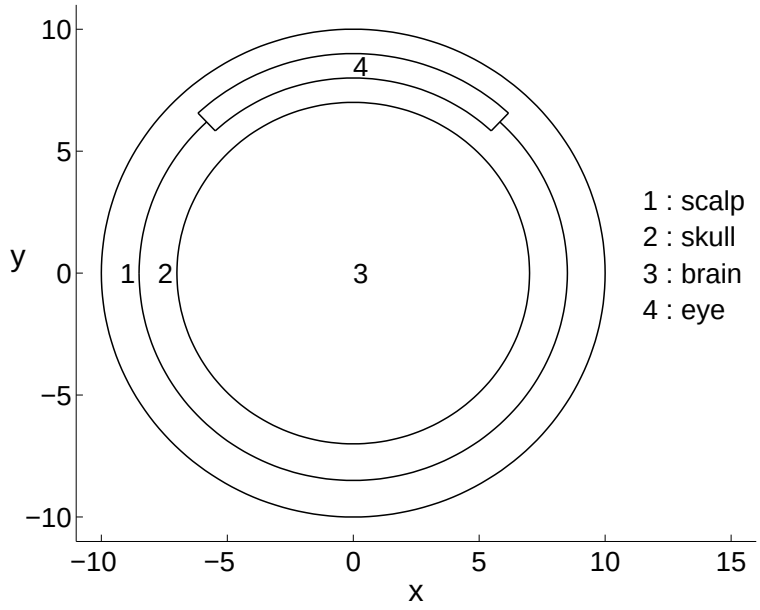

Figure 2.2: The cross-section of the model used in the FEM and BEM calculations. Regions corresponding to scalp, skull, brain and eye are labelled as 1, 2, 3, and 4, respectively.

conductivity values to the scalp, skull, brain and eye (Table 2.1). In the first case, the model is assumed to be homogeneous, in the second case the conductivity of the brain is increased to compare the BEM and FEM solutions. The results of the two cases are also compared with the analytical solutions and the RDMs are found to be less than 1%. In the third case, the tissue conductivities surrounding the eye (region 4) are changed. The scalp conductivity is increased and the skull conductivity is decreased. In the fourth case, all tissue conductivities are the same but the eye conductivity is increased. For the last case, realistic conductivities are assigned to the tissues. We observed that the RDMs between the potential fields of the FEM and BEM models are below 1% for all cases, validating the BEM implementation for intersecting surfaces.

2.5.3 Sensitivity of the measurements to eye conductivity

To investigate the effects of eyes on the forward problem solutions we compared the potential and magnetic field solutions for varying eye conductivities [89]. The head model, developed in Chapters 4 and 5, includes four tissues: scalp,

Table 2.2: RDM change in potential values between models with eyes and without eyes for a dipole located parallel to the eyes for eye conductivities of 0.3, 0.4, and 0.5 S/m

	distance between the eyes and the dipole (cm)			
$\sigma_{eyes}(S/m)$	6.6	4.4	2.7	1.4
0.3	2.15	3.15	4.60	6.38
0.4	3.50	5.17	7.63	10.56
0.5	4.49	6.68	9.91	13.67

Table 2.3: RDM change in potential values between models with eyes and without eyes for a dipole directed towards the eyes for eye conductivities of 0.3, 0.4, and 0.5 S/m

	distance between the eyes and the dipole (cm)			
$\sigma_{eyes}(S/m)$	6.6	4.4	2.7	1.4
0.3	6.90	7.57	8.41	11.08
0.4	10.72	11.95	13.56	17.91
0.5	13.29	14.98	17.26	22.75

skull, brain and eyes. A 256-electrode Neuroscan cap is used to obtain realistic electrode positions on the scalp surface (Chapter 6). The electrode positions are registered using a Polhemus/Fastrak digitizer (Figure 6.2).

The calculations are performed for a single dipole located at varying distances and orientations with respect to an eye surface. The eye conductivity is assumed to be 0.5 S/m. The RDMs and RDM*s are calculated between the two models: a realistic model with eyes and without eyes. The results obtained for the potential solutions, for a dipole located 1.4 cm away from an eye surface, are summarized in Table 2.2 and Table 2.3. It is observed that, as the dipole approaches to the eye surface the effects of eyes become significant for the potential solutions. Thus we suggest to include the eyes in the numerical model especially for sources in the prefrontal lobe. For the magnetic field calculations, the RDMs for all dipole locations and configurations are found to be less than 0.1 %.

2.5.4 Computation speed

In this section, the computation times for different stages of the forward problem are presented. The computation times are recorded for the specific head

Table 2.4: Computational complexity for a realistic mesh with 7988 nodes, A_s matrix has 1910 nodes

Matrix filling (**A** matrix)	8 minutes
Single solution ($\mathbf{A}\Phi = \mathbf{g}$)	2 minutes
Calculation of **E** (256 electrodes)	2.2 hours
Matrix filling ($\mathbf{A}_s$ matrix)	0.6 minutes
Calculation of $\mathbf{A}_s^{-1}$ matrix	20 s
Matrix filling (**H** matrix)	22 s
Calculation of **M** (256 sensors)	2.2 hours
Calculation of the modified right hand side (RHS)	10 ms
Calculation of the electrode potentials using **E**	102 s
Calculation of the sensor fields using **M**	137 ms s

model described in Chapters 4 and 5 and electrode/sensor configuration (256 electrodes/sensors). The head model includes five different tissue types: the eyes, scalp, skull, and the brain. The corresponding BEM mesh has 7988 nodes and 4026 quadratic elements. The solutions are obtained using a nonoptimized iterative solver (biconjugate gradient method). For computations, a 2.4 GHz Pentium IV personal computer (PC) with 1 GB memory is used. The BEM implementation is written using C++ programming language. Table 2.4 shows the computation times of various stages.

CHAPTER 3

USE OF THE ISOLATED PROBLEM APPROACH FOR MULTI-COMPARTMENT BEM MODELS

3.1 Intoduction

In the BEM implementations, generally, the three-shell model of the head is used to model the scalp, skull and the brain tissues. However, the low conductivity of the skull layer results in inaccuracy in the solutions of the resultant system of equations. To increase the accuracy, the isolated problem approach is employed and a modified set of equations is solved [48], [49]. When the white matter, gray matter, a (large) ventricle or a tumor in the brain is to be modeled, i.e., when more realistic head models are to be used, the IPA can still be applied. For that purpose, a general formulation was provided in the literature [48]; however, its numerical implementation has not been attempted by others in this field. In this study, the generalized version of IPA is investigated using spherical and realistic head models. The extended forms of the modified source terms are derived. Two different forms of the discretized version are presented to apply the IPA when the BEM is used for a multi-compartment tissue model in the skull. Numerical solutions for a realistic head model are provided.

Realistic modeling of the human head is necessary to increase the accuracy of EMSI solutions. Roth *et al* [63], Crouzeix *et al* [64], and Cuffin [45] investi-

gated dipole localization accuracy using spherical and realistic meshes. It was shown that a realistic model improves the localization accuracy on the order of 1-2 cm. However, in those studies, the realistic models have only three tissue types, namely, the scalp, skull and the brain. Ramon *et al* [65] examined the effects of soft skull bone, cerebrospinal fluid (CSF) and gray matter on scalp potentials using the finite element method (FEM). They observed that the scalp potentials were significantly affected by these tissues. Thus, the accuracy in the source localization can be improved if more accurate realistic head models are used in the forward problem solutions.

The IPA is a method to overcome numerical inaccuracies caused by high conductivity difference between the skull and the inner layers (CSF or brain). Hämäläinen and Sarvas [49] formulated the IPA for a three layer head model when there exists a single isolated layer (i.e., there is only brain inside the skull). In that study, a modified set of equations was derived and the results were compared with the analytical solutions. Meijs *et al* [48] derived integral equations to use the IPA with multi-layer head models assuming multiple isolated layers. However, to the knowledge of the authors, such use has not been numerically implemented by other researchers. The researchers who use models with more than three layers have not applied the IPA [69], [90], [91]. Meijs *et al* [48], tested the accuracy of solutions using a four-shell spherical model with linear elements, and concluded that the IPA is necessary to improve the MAG error measure, whereas it slightly improves the Relative Difference Measure (RDM*). Fuchs *et al* [92] proposed a weighted IPA approach that use a parameter c to improve accuracy when there are multiple layers in the skull. They have concluded that the parameter mostly depends on the skull conductivity for spherical models. Frijns *et al* [69] used high-order elements with recursive integration and compared the accuracy of various algorithms on four layer spherical meshes of different sizes. It was agreed that the use of the IPA is not necessary when quadratic elements are employed. However, the results reported in that study are for a single tangential dipole placed at 80% eccentricity (11 mm away from the cortex). Our results indicate that, for

higher eccentricities, that is, when the dipole gets closer to the brain surface, the IPA improves both MAG and RDM* metrics. This behavior is observed even if quadratic elements are used and recursive integration is applied.

This part of the thesis study contributes to the numerical accuracy of the potential solutions when a multi-compartment tissue model is used inside the skull. In itemized form, 1) a generalized formulation of the IPA for multi-layer models is presented, 2) the transfer matrix formulations derived in the previous chapter are updated to incorporate the generalized IPA, 3) the effects of the IPA on the solution accuracy is tested using spherical models, 4) the effects of the CSF layer and a tumor tissue are explored in a realistic head model. The next section introduces the formulations of the IPA and presents formulations for calculating the transfer matrices. In the results section, first, the accuracy of the BEM is investigated using spherical models with and without IPA. Realistic head models are used to investigate the effects of the CSF layer and a tumor tissue in a realistic head model, and the effect of IPA on solution accuracy. Finally, the computational performance of the forward problem solution is presented.

3.2 Isolated Problem Approach

In a three-layer head model, when the skull to brain conductivity ratio (β) is small ($\beta < 0.1$), the solution of Equation (2.5) yields numerical inaccuracies. The accuracy of the solutions can be improved using the Isolated Problem Approach [49]. In the IPA, the region inside the skull is considered as a homogeneous isolated model. The solution to the original set of equations is expressed in terms of the isolated problem solution and a correction term. In this section, 1) the derivation of the integral equations for the correction terms is extended for a multi-layer head model, 2) the discretized form of the extended modified set of equations is presented, 3) the extended version is simplified to reduce the computation time.

Let us assume that the head model has L layers. The L^{th} layer is the innermost layer and the $(K-1)^{th}$ compartment corresponds to the low conductivity

skull. We will define the surfaces S_1 to S_{K-1} as the *outer* surfaces and S_{K+1} to S_L as *inner* surfaces. The potentials on the inner surfaces are higher than the potentials on the outer surfaces, due to the low conductivity of the $(K-1)^{th}$ compartment. To reduce the numerical errors on the potentials of the outer surfaces Hämäläinen and Sarvas [49] proposed the following decomposition:

$$\phi(\vec{r}) = \phi'(\vec{r}) + \phi''(\vec{r}) \tag{3.1}$$

where $\phi''(\vec{r})$ is the solution of the integral equation for the conductor G bounded by S_K (including surfaces S_K to S_L) and $\phi'(\vec{r})$ is the correction term. When ϕ is expressed in the above given form, equation Equation (2.7) can be written as

$$\begin{aligned} \Phi' + \Phi'' &= \mathbf{A}^{-1}\mathbf{g} \\ \Phi' &= \mathbf{A}^{-1}(\mathbf{g} - \mathbf{A}\Phi'') \\ \Phi' &= \mathbf{A}^{-1}\mathbf{g}' \end{aligned} \tag{3.2}$$

Decomposing the solution into two parts does not provide any advantage unless the correction term Φ' is solved more accurately. As β goes to zero, the potentials on the outer surfaces should vanish (this can only be achieved if $\mathbf{g}$ and $\mathbf{A}\Phi''$ cancel each other). However, since the second term is calculated numerically, it is difficult to obtain exact cancellation. The residual error term will be multiplied with $\mathbf{A}^{-1}$ which has a higher condition number due to small β. The IPA is based on the more accurate solution of the right-hand side term $\mathbf{g}'$. The correct behavior is guaranteed if the right-hand side is calculated as given in [49], [48]. Note that, in that representation, each entry in the right-hand side is obtained as a multiple of β.

The formulations below derive the IPA formulation for a general multi-layer model where there are arbitrary number of layers inside and outside the low conductivity layer (Figure 3.1).

For the isolated problem, $\phi''(\vec{r})$ is zero on the surfaces $S_1, \ldots, S_{K-1}$ and the conductivity $\sigma_K^+ = 0$. Therefore, the integral equation for the isolated problem can be expressed as:

$$\bar{\sigma}''(\vec{r})\phi''(\vec{r}) \;=\; g(\vec{r}) + \frac{\sigma_K^-}{4\pi}\int_{S_K} \phi''(\vec{r}\,')\frac{\vec{R}}{R^3}\cdot d\vec{S}_K(\vec{r}\,')$$

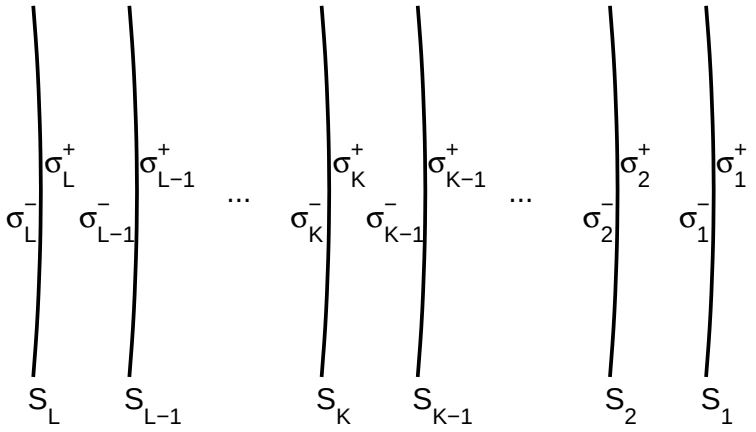

Figure 3.1: Schematic representation of the model. The model has L layers where $(K-1)^{th}$ compartment has a low conductivity that corresponds to the skull in a head model.

$$+ \quad \frac{1}{4\pi} \sum_{j=K+1}^{L} (\sigma_j^- - \sigma_j^+) \int_{S_j} \phi''(\vec{r}\,') \frac{\vec{R}}{R^3} \cdot d\vec{S}_j(\vec{r}\,'). \qquad (3.3)$$

where $\bar{\sigma}''(\vec{r})$ represents the mean conductivity around a point in the isolated-problem space. (Note that the conductivity of the points on S_K is different in the original and the isolated models). The integral equation for the correction term $\phi'(\vec{r})$ can be obtained by inserting Equation (3.1) into Equation (2.1):

$$\bar{\sigma}(\vec{r})(\phi'(\vec{r}) + \phi''(\vec{r})) = g(\vec{r}) + \frac{1}{4\pi} \sum_{j=1}^{L} (\sigma_j^- - \sigma_j^+) \int_{S_j} (\phi'(\vec{r}\,') + \phi''(\vec{r}\,')) \frac{\vec{R}}{R^3} \cdot d\vec{S}_j(\vec{r}\,'),$$

$$\begin{aligned} \bar{\sigma}(\vec{r})\phi'(\vec{r}) + \bar{\sigma}(\vec{r})\phi''(\vec{r}) &= g(\vec{r}) + \frac{1}{4\pi} \sum_{j=1}^{L} (\sigma_j^- - \sigma_j^+) \int_{S_j} \phi'(\vec{r}\,') \frac{\vec{R}}{R^3} \cdot d\vec{S}_j(\vec{r}\,') \\ &+ \frac{1}{4\pi} \sum_{j=K}^{L} (\sigma_j^- - \sigma_j^+) \int_{S_j} \phi''(\vec{r}\,') \frac{\vec{R}}{R^3} \cdot d\vec{S}_j(\vec{r}\,'). \qquad (3.4) \end{aligned}$$

Combining equations Equation (3.3) and Equation (3.4), the following equation can be obtained for the correction terms on the inner and outer surfaces $(i = 1 \ldots K-1, K+1 \ldots L)$:

$$\begin{aligned} (\sigma_i^- + \sigma_i^+)\phi'(\vec{r}) &= \frac{1}{2\pi} \sum_{j=1}^{L} (\sigma_j^- - \sigma_j^+) \int_{S_j} \phi'(\vec{r}\,') \frac{\vec{R}}{R^3} \cdot d\vec{S}_j(\vec{r}\,') \\ &- \frac{\sigma_K^+}{2\pi} \int_{S_K} \phi''(\vec{r}\,') \frac{\vec{R}}{R^3} \cdot d\vec{S}_j(\vec{r}\,'). \qquad (3.5) \end{aligned}$$

On the K^{th} surface S_K, $\bar{\sigma}(\vec{r}) = (\sigma_K^- + \sigma_K^+)/2$, and $\bar{\sigma}''(\vec{r}) = \sigma_K^-/2$. Combining equations Equation (3.3) and Equation (3.4) results in the following equation for the corrections on the K^{th} surface S_K:

$$\begin{aligned}(\sigma_K^- + \sigma_K^+)\phi'(\vec{r}) &= \frac{1}{2\pi}\sum_{j=1}^{L}(\sigma_j^- - \sigma_j^+)\int_{S_j}\phi'(\vec{r}\,')\frac{\vec{R}}{R^3}\cdot d\vec{S}_j(\vec{r}\,') \\ &- \sigma_K^+\phi''(\vec{r}) - \frac{\sigma_K^+}{2\pi}\int_{S_K}\phi''(\vec{r}\,')\frac{\vec{R}}{R^3}\cdot d\vec{S}_K(\vec{r}\,'). \qquad (3.6)\end{aligned}$$

Note that the second term on the right hand side of Equation (3.6) is due to the fact that the conductivity of the isolated model on which $\phi''(\vec{r})$ is computed is zero outside the K^{th} layer. Equations Equation (3.5) and Equation (3.6) are equivalent to the IPA expressions derived by Meijs *et al* [48]. By discretizing these integral equations, the following matrix equation can be obtained:

$$\Phi' = \mathbf{g}' + \mathbf{C}\Phi' \qquad (3.7)$$

where Φ' is the $N \times 1$ vector of the correction terms, and $\mathbf{g}'$ is an $N \times 1$ vector representing the modified version of the source term. This equation uses the same $\mathbf{C}$ matrix computed for Φ. Using equations Equation (3.5) and Equation (3.6) the modified source term $\mathbf{g}'$ can be written in block-matrix form as

$$\mathbf{g}' = \begin{bmatrix} \mathbf{g}'_1 \\ \vdots \\ \mathbf{g}'_{K-1} \\ \mathbf{g}'_K \\ \mathbf{g}'_{K+1} \\ \vdots \\ \mathbf{g}'_L \end{bmatrix} = \begin{bmatrix} \frac{\beta}{\beta-1}\mathbf{C}_{1K}\Phi''_K \\ \vdots \\ \frac{\beta}{\beta-1}\mathbf{C}_{(K-1)K}\Phi''_K \\ \frac{\beta}{\beta-1}\mathbf{C}_{KK}\Phi''_K - \frac{\beta}{\beta+1}\Phi''_K \\ \frac{\beta}{\beta-1}\mathbf{C}_{(K+1)K}\Phi''_K \\ \vdots \\ \frac{\beta}{\beta-1}\mathbf{C}_{LK}\Phi''_K \end{bmatrix}, \qquad (3.8)$$

where $\beta = \sigma_K^+/\sigma_K^-$. In this representation, $\mathbf{g}'_i$ and Φ''_i are the sub-vectors of $\mathbf{g}'$ and Φ'', respectively, where the subscript i stands for the ith surface. Similarly, $\mathbf{C}_{ij}$ represents a sub-matrix of $\mathbf{C}$:

$$\mathbf{C}_{ij} = \frac{1}{2\pi}\frac{\sigma_j^- - \sigma_j^+}{\sigma_i^- + \sigma_i^+}\int_{S_j}\frac{\vec{R}}{R^3}\cdot d\vec{S}_j(\vec{r}\,'). \qquad (3.9)$$

An alternative representation for $\mathbf{g}'$ can be obtained by multiplying both sides of Equation (3.3) with $\beta/(\sigma_i^- + \sigma_i^+)$, and discretizing the integral equations as follows:

$$\mathbf{g}' = \begin{bmatrix} \mathbf{g}'_1 \\ \vdots \\ \mathbf{g}'_{K-1} \\ \mathbf{g}'_K \\ \mathbf{g}'_{K+1} \\ \vdots \\ \mathbf{g}'_L \end{bmatrix} = \begin{bmatrix} \beta\mathbf{g}_1 + \beta\mathbf{C}_{1(K+1)}\Phi''_{K+1} + \ldots + \beta\mathbf{C}_{1L}\Phi''_L \\ \vdots \\ \beta\mathbf{g}_{K-1} + \beta\mathbf{C}_{(K-1)(K+1)}\Phi''_{K+1} + \ldots + \beta\mathbf{C}_{(K-1)L}\Phi''_L \\ \beta\mathbf{g}_K - \frac{2\beta}{\beta+1}\Phi''_K + \beta\mathbf{C}_{K(K+1)}\Phi''_{K+1} + \ldots + \beta\mathbf{C}_{1L}\Phi''_L \\ \frac{\beta}{\beta-1}\mathbf{C}_{(K+1)K}\Phi''_K \\ \vdots \\ \frac{\beta}{\beta-1}\mathbf{C}_{LK}\Phi''_K \end{bmatrix}. \tag{3.10}$$

where $\mathbf{g}_i$ can be written as

$$\mathbf{g}_i = \frac{2g(\vec{r})}{\sigma_i^- + \sigma_i^+} \tag{3.11}$$

For a three layer head model, there is only a single layer inside the skull and $K = L = 3$. Thus, the expression given in Equation (3.10) becomes:

$$\mathbf{g}' = \begin{bmatrix} \mathbf{g}'_1 \\ \mathbf{g}'_2 \\ \mathbf{g}'_3 \end{bmatrix} = \begin{bmatrix} \beta\mathbf{g}_1 \\ \beta\mathbf{g}_2 \\ \beta\mathbf{g}_3 - \frac{2\beta}{\beta+1}\Phi''_3 \end{bmatrix} \tag{3.12}$$

which is the same expression derived previously [49]. The integration of the generalized IPA formulation to the BEM solution will be described in the following sections.

3.3 Accelerated BEM for EEG

The accelerated BEM formulation that incorporates the IPA was given for a three layer model in chapter 2. In this section the formulation is updated to cover the IPA formulation explained in the previous section. When the IPA is applied, the right hand side vector $\mathbf{g}$ must be modified using Equation (3.8). This modification requires Φ''_K that must be calculated for every source configuration using the isolated model:

$$\begin{bmatrix} \Phi''_K \\ \vdots \\ \Phi''_L \end{bmatrix} = (\mathbf{A}_s)^{-1} \begin{bmatrix} \mathbf{g}_K \\ \vdots \\ \mathbf{g}_L \end{bmatrix}. \tag{3.13}$$

In this equation, $\mathbf{A}_s$ is in the form of $(\mathbf{I} - \mathbf{C_s})$, where $\mathbf{C_s}$ is the deflated coefficient matrix of the isolated inner layers. The vector $[\mathbf{g}_K \ldots \mathbf{g}_L]$ is the corresponding source vector. Note that, to compute the node potentials on the outer surface of the isolated model, only the first N_K rows of $(\mathbf{A}_s)^{-1}$ is required. (Here N_K denotes the number of nodes on that surface).

To summarize, the accelerated approach for potential field calculations using the IPA starts with the calculation of the transfer matrices $\mathbf{E}$ and $\mathbf{A}_s$. To modify the source vector, $\mathbf{C}_{1K}, \ldots, \mathbf{C}_{LK}$ matrices are also required. Once these matrices are calculated, the potentials due to an arbitrary source configuration can be obtained using the following steps: 1) calculate Φ''_K using Equation (3.13), 2) calculate $\mathbf{g}'$ using Equation (3.8), and 3) solve Φ_e using Equation (2.9).

3.4 Accelerated BEM for MEG

For a multi-compartment BEM model, the accelerated BEM formulation for the calculation of the magnetic field is extended as follows. When the IPA is applied, the equation Equation (2.8) is written as:

$$\begin{aligned} \mathbf{B} &= \mathbf{B}_0 + \mathbf{H}(\Phi' + \Phi'') \\ &= \mathbf{B}_0 + \mathbf{H}\Phi' + \mathbf{H}\Phi'' \\ &= \mathbf{B}_0 + \mathbf{H}\mathbf{A}^{-1}\mathbf{g}' + \mathbf{H}\Phi'' \end{aligned} \tag{3.14}$$

Since Φ'' is zero for the first $K-1$ layers, we can write $\mathbf{H}\Phi''$ as

$$\mathbf{H}\Phi'' = [\mathbf{H}_1 \ \ldots \ \mathbf{H}_K \ \ldots \ \mathbf{H}_L] \begin{bmatrix} 0 \\ \vdots \\ \Phi''_K \\ \vdots \\ \Phi''_L \end{bmatrix} = \mathbf{H}_K\Phi''_K + \ldots + \mathbf{H}_L\Phi''_L \tag{3.15}$$

Therefore, Equation (3.14) becomes

$$\mathbf{B} = \mathbf{B}_0 + \mathbf{M}\mathbf{g}' + \mathbf{H}_K\Phi''_K + \ldots + \mathbf{H}_L\Phi''_L. \tag{3.16}$$

In summary, to obtain magnetic field solutions, first the matrices $\mathbf{M}, \mathbf{H}_K, \ldots, \mathbf{H}_L$, $\mathbf{A}_s^{-1}$, and $\mathbf{C}_{1K}, \ldots, \mathbf{C}_{LK}$ are computed and stored. After this pre-computation stage, the magnetic field solutions for an arbitrary source distribution can be obtained using Equation (3.16) with simple matrix-vector multiplications.

3.5 Results

In this section, first, the accuracy of the numerical solutions obtained using the generalized form of the IPA is tested for a four layer spherical model. Using the realistic head model (chapters 4 and 5) and the generalized form of the IPA, the effect of the CSF layer and an inhomogeneity inside the brain on the scalp potentials are explored. The effect of the IPA is investigated using the realistic head model (with an inhomogeneity in the brain). Finally, the computation times for the realistic head model are presented.

3.5.1 Accuracy of the BEM solutions

To assess the accuracy of the solutions, a four-layer spherical model is used. The model represents the brain, CSF, skull and the scalp with conductivities 0.33, 1.0, 0.0042, and 0.33 S/m, respectively [93]. The radii of the spheres are chosen as 61, 65, 71, and 75 mm as described in Meijs *et al* [48].

The BEM mesh used in the simulations has 512 elements and 1026 nodes per layer. To improve the accuracy of the solutions, the recursive integration technique is employed [69]. Accuracy of the numerical solutions is tested with the analytical solutions provided by Kavanagh *et al* [32]. Table 3.1 shows the percentage RDM and RDM* values for various tangential (x directed) dipole locations on the z axis ($z = 1 - 6\ cm$). The numerical solutions are obtained twice (with and without the IPA). It is observed that application of the IPA improves RDM significantly. For deep dipoles RDM* is relatively small and it is not affected by the application of the IPA. For shallow dipoles, RDM* increases if the IPA is not applied. Table 3.2 presents the same information for radial dipoles. For the radial shallow dipoles, the increase in the RDM and RDM* is evident.

Table 3.1: The relative difference measures (%RDMs and RDM*s) for various tangential (x-directed) dipoles located on the z axis ($z = 1-6\ cm$) in a 4-layer spherical head model. The results are presented for solutions with and without the IPA.

Distance	with IPA		without IPA	
(cm)	%RDM	RDM*	%RDM	RDM*
1.0	0.50	0.0006	12.0	0.0060
1.5	0.49	0.0009	12.1	0.0062
2.0	0.49	0.0011	12.2	0.0064
2.5	0.49	0.0015	12.2	0.0066
3.0	0.49	0.0018	12.3	0.0068
3.5	0.48	0.0022	12.4	0.0072
4.0	0.48	0.0026	12.6	0.0087
4.5	0.48	0.0031	12.9	0.0141
5.0	0.49	0.0039	13.8	0.0263
5.5	0.53	0.0046	13.9	0.0384
6.0	1.29	0.0118	16.9	0.1170

Table 3.2: The relative difference measures (%RDMs and RDM*s) for various radial (z-directed) dipoles located on the z axis ($z = 1 - 6\ cm$) in a 4-layer spherical head model. The results are presented for solutions with and without IPA.

Distance	with IPA		without IPA	
(cm)	%RDM	RDM*	%RDM	RDM*
1.0	0.50	0.0009	11.9	0.0059
1.5	0.54	0.0023	11.8	0.0063
2.0	0.69	0.0050	11.7	0.0081
2.5	1.04	0.0093	11.5	0.0122
3.0	1.61	0.0154	11.3	0.0189
3.5	2.36	0.0232	11.2	0.0282
4.0	3.29	0.0325	11.2	0.0399
4.5	4.34	0.0431	11.7	0.0543
5.0	5.49	0.0545	11.9	0.0770
5.5	6.70	0.0640	26.7	0.2370
6.0	9.98	0.0321	227.9	1.8870

3.5.2 Results with the realistic model

The effects of different tissues on the forward problem are investigated using two simulations. Potentials for a reference BEM model are compared with the potentials for two different head models: the same model 1) without CSF, and 2) with an inhomogeneity inside the brain. The results are obtained using the generalized form of the IPA. The effect of the IPA is then investigated when there is an inhomogeneity in the brain. In all simulation studies, a reference head model is used that includes five tissue types. The conductivities of the scalp, skull, CSF, brain and eyes are 0.33, 0.0042, 1, 0.33 and 0.5 S/m, respectively. A 256-electrode Neuroscan cap is used to obtain realistic electrode positions on the scalp surface. The electrode positions are acquired using a Polhemus/Fastrak digitizer and registered to the BEM model.

For realistic models, the error measure MAG is also calculated (Meijs *et al* 1989):

$$\mathrm{MAG} = \sqrt{\frac{\sum_{i=1}^{m} V_i^2}{\sum_{i=1}^{m} V_i'^2}}. \tag{3.17}$$

When comparing realistic models, using RDM, RDM* and MAG, V' represents the potential field calculated using the reference head model.

3.5.2.1 The effect of the CSF layer on the potentials:

The effect of the CSF layer on the measurements is investigated by comparing the two models with and without the CSF layer. For the first (reference) model, the solutions are obtained using Equation (3.8). In the latter model, since there is a single layer in the skull, the IPA is applied as given in Equation (3.12). The calculations are performed for 6 dipole locations in both x- and z-directions. Table 3.3 presents the %RDM, RDM* and MAG. The first column gives the distance of the dipole from the top surface of the brain. It is observed that including the CSF layer in the head model changes the scale of the potentials considerably. However, relatively less change is observed in the field patterns.

Table 3.3: The %RDMs, RDM*s and MAG values for x- and z-directed dipoles located on the z axis. The potentials of the reference head model are compared with the potentials when there is no CSF layer in the head model.

Distance	x-directed			z-directed		
(cm)	%RDM	RDM*	MAG	%RDM	RDM*	MAG
5.6	32.5	0.13	0.69	446.2	0.18	5.44
4.6	33.4	0.13	0.68	440.2	0.13	5.39
3.6	518.5	0.12	6.18	439.5	0.08	5.39
2.6	507.7	0.12	6.07	445.2	0.04	5.45
1.6	493.4	0.11	5.93	461.9	0.03	5.62
0.6	475.5	0.10	5.75	523.4	0.07	6.23

3.5.2.2 The effect of an inhomogeneity in the brain:

The effect of an inhomogeneity is investigated when the generalized form of the IPA is applied. The inhomogeneity in the brain is modeled using a spherical region of 1 cm in radius. A cut-away view of the model containing the inhomogeneity is shown in Figure 3.2. The forward problem calculations are performed for a single dipole located at 0.5 cm near the inhomogeneity with parallel and perpendicular orientations with respect to the inhomogeneity surface (Figure 3.3). The comparisons are repeated for varying inhomogeneity conductivities. In Table 3.4, the %RDMs, RDM*s and MAG values are calculated between the forward problem solutions of the two head models with and without the inhomogeneity. It is observed that when the dipole is oriented toward the inhomogeneity, the change in the potential is significant as reflected by the RDM and RDM*. The RDM and RDM* values go through minimum values when the conductivity of the inhomogeneity is assigned as 0.165 S/m and 0.66 S/m. These values are the closest values to the brain conductivity among the other conductivity values. As the conductivity of the inhomogeneity differs from the conductivity of the brain, the error measures increase.

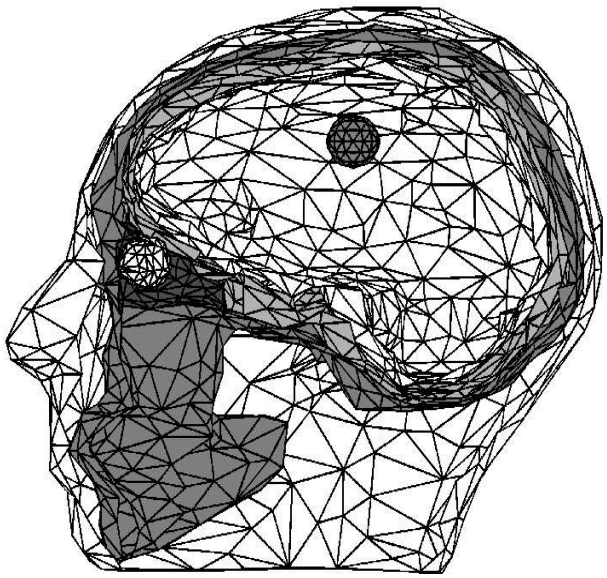

Figure 3.2: The cut-away view of the head mesh including the inhomogeneity.

Table 3.4: Effect of the inhomogeneity on the potential solutions. The potentials using the two head models are compared. %RDMs, RDM*s and MAG values for a dipole located 0.5 cm near the inhomogeneity are presented. The dipole is oriented parallel and perpendicular to the inhomogeneity.

Conductivity	parallel			perpendicular		
(S/m)	%RDM	RDM*	MAG	%RDM	RDM*	MAG
0.033	12.24	0.0062	1.12	49.70	0.51	0.87
0.066	10.31	0.0055	1.10	47.82	0.49	0.91
0.165	5.47	0.0037	1.05	44.28	0.44	0.99
0.660	7.83	0.0049	0.92	45.48	0.35	1.24
1.650	17.28	0.0126	0.83	54.97	0.29	1.42
3.300	22.52	0.0181	0.78	61.84	0.27	1.52

3.5.2.3 The effect of the IPA on the potentials when there is an inhomogeneity:

The effect of the IPA is investigated when there is an inhomogeneity in the brain. In Table 3.5, the %RDMs, RDM*s and MAG values are computed between solutions computed with and without the IPA (using the second head model). It is observed that in addition to a considerable change in the scale of the solutions (MAG), the RDM* implies topological differences especially for perpendicular dipoles. (Considering a maximum value of 2 for the RDM*, an RDM* value of 0.29 corresponds to a 15% change in the field pattern).

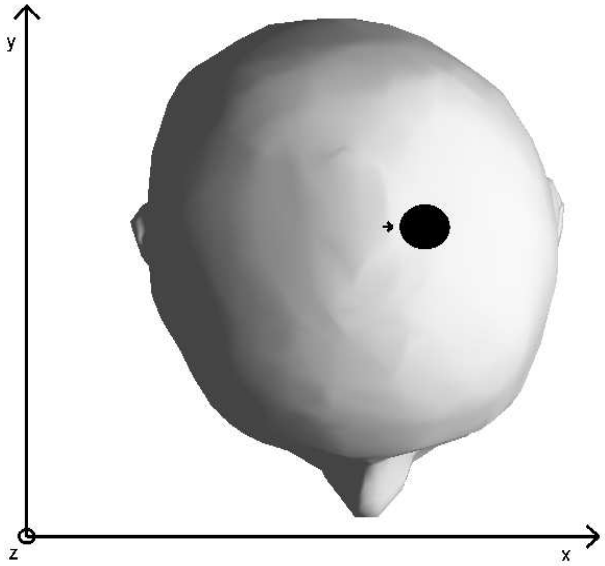

Figure 3.3: The top view of the head model to show the location of the inhomogeneity and the dipole.

Table 3.5: Effect of the IPA on the potential solutions when inhomogeneity is included. % RDM , RDM*s and MAGs for a dipole located 0.5 cm near the inhomogeneity are presented. The dipole is oriented parallel and perpendicular to the inhomogeneity.

Conductivity	parallel			perpendicular		
(S/m)	%RDM	RDM*	MAG	%RDM	RDM*	MAG
0.033	552.92	0.12	6.52	545.54	0.29	6.61
0.066	553.00	0.12	6.52	550.68	0.28	6.46
0.165	553.26	0.12	6.52	561.41	0.25	6.58
0.660	554.38	0.12	6.54	580.17	0.20	6.78
1.650	555.58	0.12	6.55	588.29	0.18	6.86
3.300	556.40	0.11	5.56	592.11	0.17	6.90

For illustrative purposes, the field patterns (the contour plots of the scalp potentials) are also presented for three cases: 1) the reference head model, 2) model with an inhomogeneity of conductivity 0.033 S/m, and 3) model with an inhomogeneity of 3.3 S/m. For all three cases, two figures are given (Figure 3.4). The potentials on the left-hand-side are computed with the generalized form of the IPA. In the right-hand-side, the IPA is not used. It is observed that when the conductivity of the inhomogeneity is low, the overall potential values are reduced. When the inhomogeneity is relatively more conductive, the potential values are increased. An inhomogeneity in the brain causes a

Table 3.6: Computational complexity for a realistic mesh with 9906 nodes, A_s matrix has 3828×3828 entries.

Matrix filling (**A** matrix)	12 minutes
Single solution ($\mathbf{A}\Phi = \mathbf{g}$)	3 minutes
Calculation of **E** (256 electrodes)	3.2 hours
Matrix filling ($\mathbf{A}_s$ matrix)	2 minutes
Calculation of $\mathbf{A}_s^{-1}$ matrix	50 s
Matrix filling (**H** matrix)	28 s
Calculation of **M** (256 sensors)	3.2 hours
Calculation of the modified right hand side (RHS)	3 s
Calculation of the electrode potentials using **E**	3.7 s
Calculation of the sensor fields using **M**	4 s

shift in the potential pattern towards the inhomogeneity. The inhomogeneity acts like a secondary source and affects the potential pattern accordingly. This behavior was also discussed previously [56], [79]. When the IPA is not applied, in general, the location of the extrema changes and there are additional unexpected contours (on the lower left side) that show numerical inaccuracies. It is concluded that when the IPA is not applied, the effect of inner layers on the surface potentials are suppressed.

3.5.3 Computation speed

In this section, the computation times are updated for a head model including five different tissue types: the eyes, scalp, skull, CSF and the brain. The corresponding BEM mesh has 9906 nodes and 4984 quadratic elements. To calculate the modified source vector in the IPA, equation Equation (3.8) is used. The sub-matrix corresponding to the K^{th} layer of the BEM mesh of the **C** matrix is 1910×9906. Table 3.6 shows the computation times of various stages.

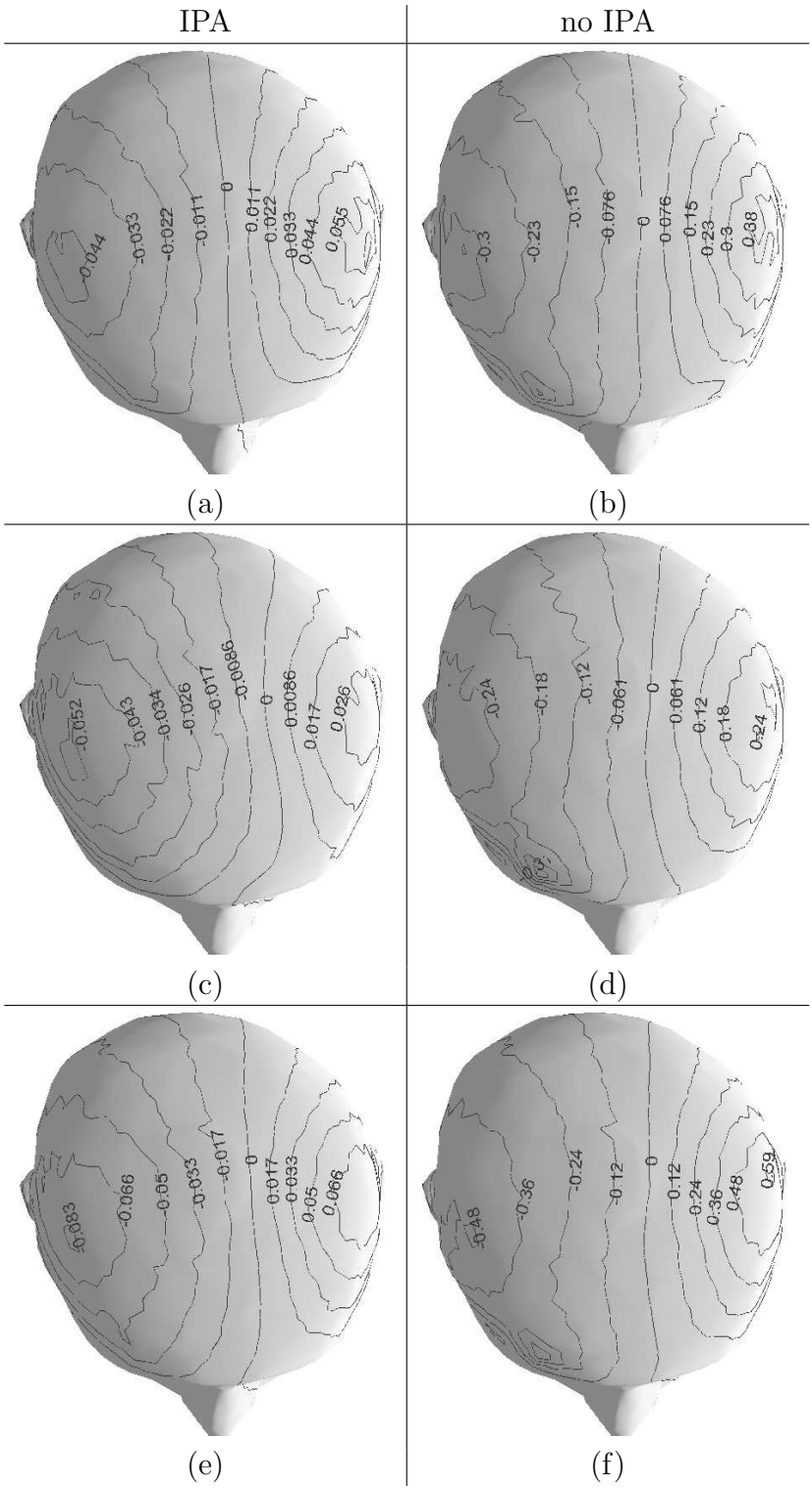

Figure 3.4: Contour plots on a realistic head mesh with and without IPA for various inhomogeneity conductivities: (a) and (b) no inhomogeneity, (c) and (d) inhomogeneity with low conductivity = 0.033 S/m, (e) and (f) inhomogeneity with high conductivity = 3.3 S/m.

CHAPTER 4

REALISTIC HEAD MODELING: THE SEGMENTATION PHASE

4.1 Introduction

To create an accurate model of the head, one must first identify the main tissues of the head from high resolution volume images. The process of classifying image elements that have the same properties is called *segmentation*. There are three major segmentation methods in the literature: 1) the deterministic methods that use classical image processing tools like thresholding, region growing, and morphological operations [94], [95], [96], [97], [98], [99], 2) the statistical methods based on probabilistic methods that may also estimate the inhomogeneity in the MR images [100], [101], [102] and, 3) methods that use a deformable atlas [103], [104], [105].

For realistic head modeling semi-automatic segmentation algorithms of MR slices using different techniques such as region growing, thresholding and morphological operations have been employed [106], [92], [61]. In general, the main tissues in the head, like scalp, skull and brain layers, are included in the realistic model [63], [107], [108], [64], [109], [110], [111], [112]. Usually, these tissues are classified from T_1–weighted MR images since it provides high soft tissue contrast. Different imaging modalities might be required to identify more tissue types. For instance, the cerebrospinal fluid can not be distinguished from the skull using T_1–weighted images. Similarly, skull cannot be separated from air using MR images, and computed X-ray tomography (CT) is used when the

correct modeling of the skull is important [113].

In this work, the scalp, skull, CSF, eyes, GM and WM are segmented from the 3–dimensional (3D) multimodal MR images of the head. A hybrid algorithm is developed that applies the snakes algorithm, region growing, thresholding, and morphological operations [114].

This chapter first summarizes the properties of the head MR images. Then the applied segmentation algorithm and the methods used in the segmentation process are described. Finally, the segmentation results are presented.

4.2 Properties of MR images

Magnetic resonance imaging is a dynamic and flexible medical imaging technique that allows one to study the anatomic properties of the body. Its dependence on the biologically variable parameters of proton density, longitudinal relaxation time (T_1), and transverse relaxation time (T_2), allows variable image contrast to be achieved by using different pulse sequences and by changing the imaging parameters. The signal intensity on the MR image is determined by three basic parameters: 1) proton density, 2) T_1 relaxation time, and 3) T_2 relaxation time. Proton density is the concentration of protons in the tissue in the form of water. The T_1 and T_2–relaxation times define the way that the protons revert back to their resting states after the initial radio frequency (RF) pulse. The contrast on the MR image can be manipulated by changing the pulse sequence parameters. A pulse sequence sets the specific number, strength, and timing of the RF and gradient pulses. The two most important parameters are the repetition time (TR) and the echo time (TE). The TR is the time between consecutive 90–degree RF pulses. The TE is the time between the initial 90–degree RF pulse and the echo. The most common pulse sequences are the T_1–weighted and T_2–weighted spin-echo sequences. The T_1–weighted sequence uses a short TR and short TE (TR $<$ 1000 ms, TE $<$ 30 ms). The T_2–weighted sequence uses a long TR and long TE (TR $>$ 1500 ms, TE $>$ 60 ms). The T_2–weighted sequence is usually employed as a dual echo sequence. The first or shorter echo (TE $<$ 30 ms) is weighted by proton density

Table 4.1: Summary of MRI Tissue Characteristics of Brain Structures

	Relaxation time		**Image contrast**		
	T_1	T_2	T_1	T_2	PD
CSF	long	long	dark	bright	gray
GM	inter.	inter.	gray	gray	gray
WM	short	short	bright	gray	gray
fat	short	inter.	bright	gray	bright
cortical bone	long	short	dark	dark	dark
air	long	short	dark	dark	dark
blood	long	short	dark	dark	dark
oedema	long	long	gray/dark	bright	bright/gray

(PD) or a mixture of T_1 and T_2–weighted images.

The primary determinants of signal intensity and contrast in the MR images are the T_1 and T_2–relaxation times. The contrast is distinctly different in T_1 and T_2–weighted images. In Table 4.1 the main characteristics of the tissues in the head are presented. In Figure 4.1 axial views of T_1–weighted, T_2–weighted and PD–weighted MR images are presented.

Most of the researchers in EMSI research, use T_1–weighted MR images for segmentation. However, it is difficult to isolate the skull from the background and air regions using MR images, as the skull has low water content. Fuchs *et al* [92] approximated the skull layer by expanding and smoothing the brain surface obtained from T_1–weighted MR images. Huiskamp *et al* [113] solved this problem by segmenting the skull from Computed Tomography (CT) images. However, it is costly to use both MR and CT images for segmentation and x-ray may be hazardous for the patient. In this thesis study, a hybrid algorithm is developed which use T_1–, T_2– and PD–weighted MR images for segmentation.

4.3 The Hybrid Segmentation Algorithm

The segmentation process begins by removing the background from the volume data. For this purpose, first a threshold is selected using the whole head PD images. The threshold is found automatically using Nobuyuki's method [115]. After obtaining the threshold for the background, the snakes algorithm

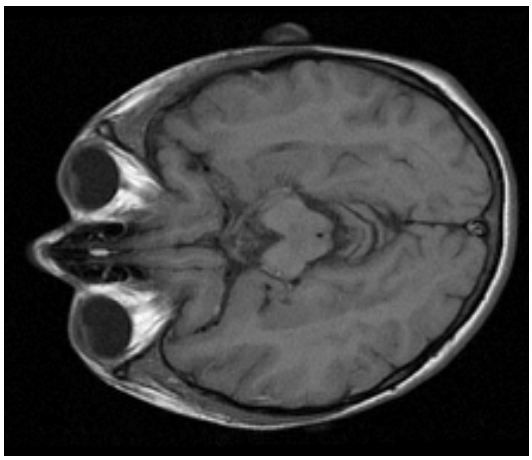

(a)

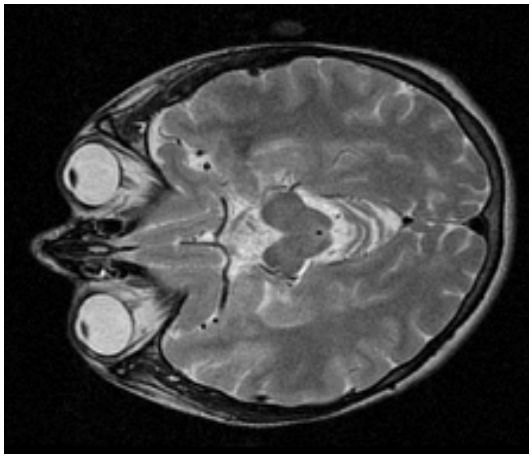

(b)

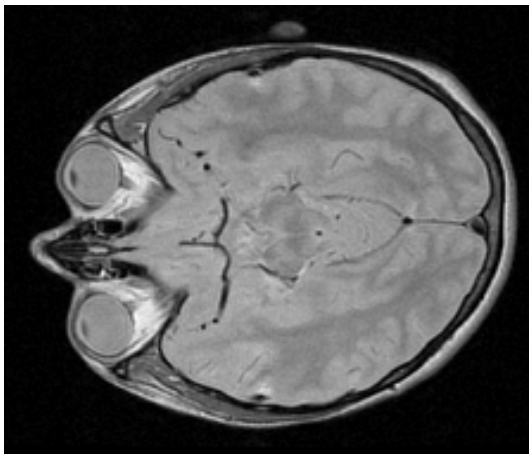

(c)

Figure 4.1: MR images of an axial slice in the head. (a) T_1–weighted, (b) T_2–weighted, (c) PD–weighted.

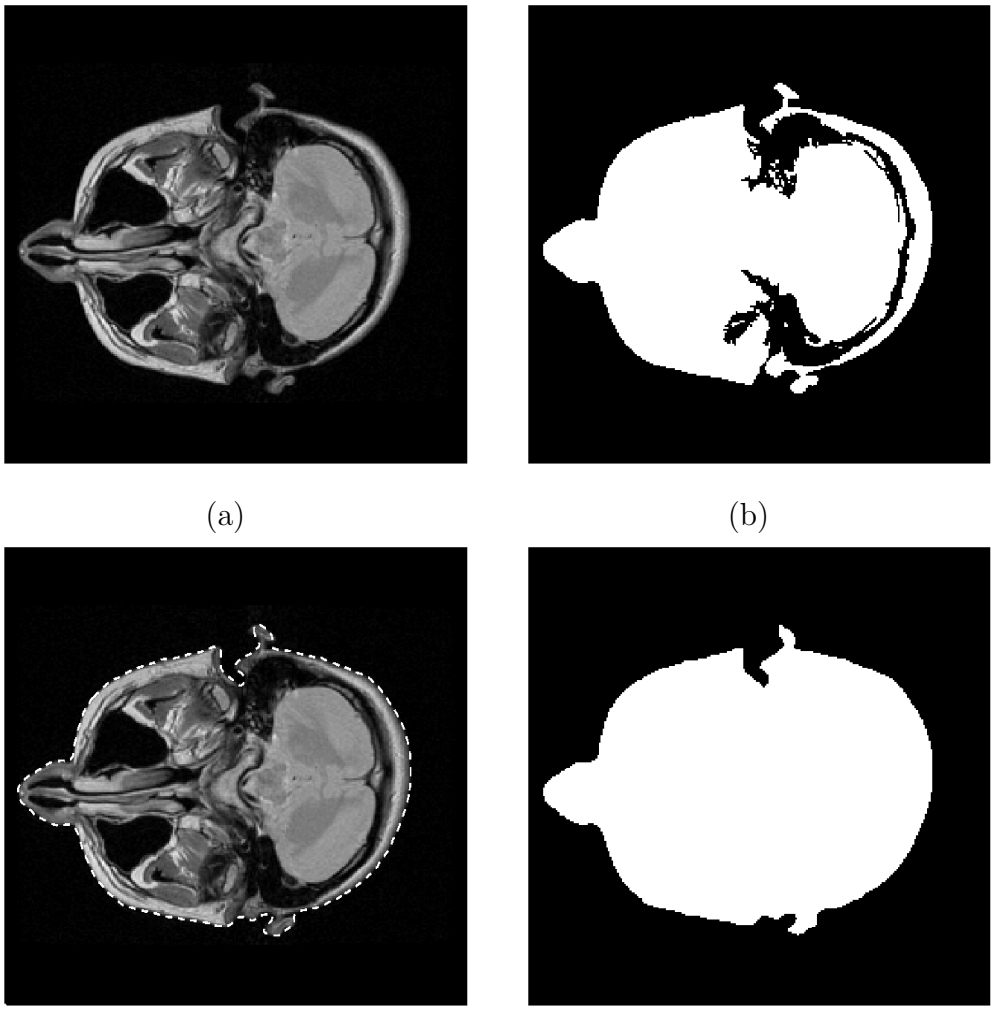

Figure 4.2: Obtaining the scalp surface. (a) A slice in PD images, (b) the slice after simple thresholding of this slice, (c) the snakes algorithm is applied to the slice, (d) scalp is extracted using the snakes algorithm.

[116] with the gradient vector flow [117] is applied to each slice. The snakes algorithm is used to obtain the scalp as a closed surface. A demonstration for one slice is shown in Figure 4.2.

After removing the background, the skull and the sinus regions are extracted from each PD image using thresholding. To identify the eye tissues (i.e., the eyeballs, fat and muscle tissues connected to the rear surface of the eyeballs) an eye template is obtained from a T_1–weighted slice where the eyes have the largest cross-section. The use of this template confines the region over which the region growing algorithm is applied at each slice. Using this

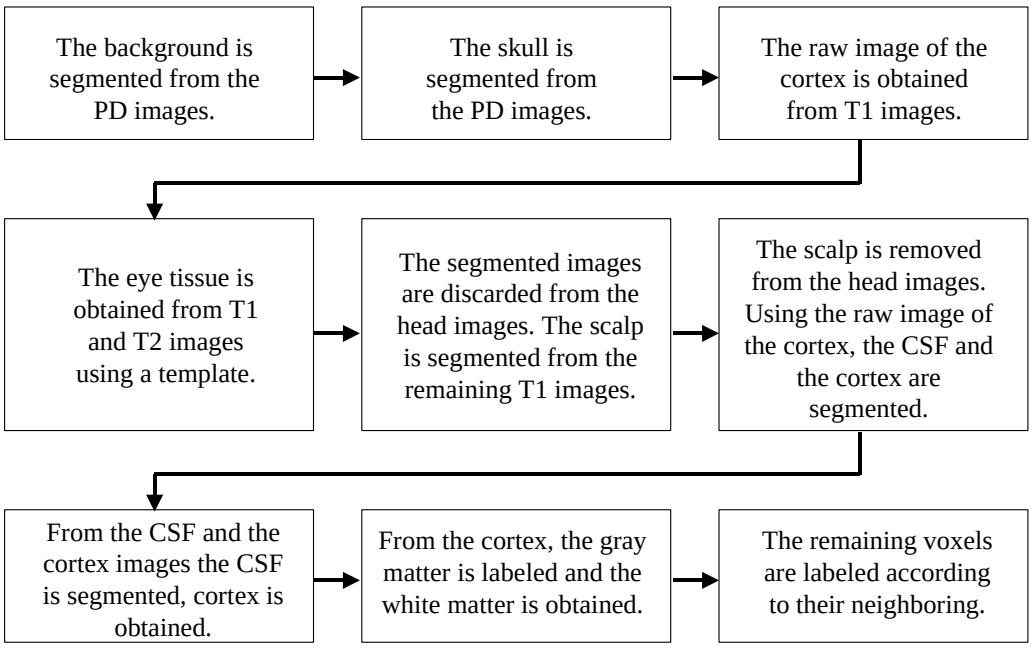

Figure 4.3: Flowchart of the segmentation algorithm.

template, the fat and muscle tissues are segmented from the T_1–weighted images. The eyeballs are then extracted from the T_2–weighted images. The scalp is segmented from the unlabelled voxels using the thresholding, region growing and morphological operations. When the segmented regions are removed from the images, the remaining regions include the CSF, WM and GM. To determine the CSF-GM and the GM-WM boundaries two thresholds are chosen from the T_1–weighted images. After thresholding, the GM and WM are obtained by region growing. The remaining voxels are then labelled according to their neighbors. The flowchart of the segmentation algorithm is presented in Figure 4.3.

To represent the inner and outer layers of the skull as a single surface, the holes in the skull must be removed. After the segmentation process, the snakes algorithm is used from the inside and outside of the segmented skull for each layer.

In the following sections, the snakes algorithm, threshold selection, morphological operations, and region growing will be explained.

4.3.1 The Snakes Algorithm

The snakes algorithm originates from the work done by Kass *et al* [116]. It is a technique of matching a deformable model to an image by means of energy minimization. The energy functional that is minimized is a weighted combination of the following three forces or energies:

1. the internal contour energy which emerges from the shape of the snake and enforces smoothness,
2. the image force which attracts the contour to the desired features, and
3. external constraint forces.

A snake model has the ability to deform elastically, however, any deformation increases its internal energy causing a *restitution force* which tries to bring it back to its original shape. The snake is also assumed to be immersed in a potential energy field (created by the image) which applies a force on the snake. These two forces balance each other and the snake contour actively adjusts its position and shape until it reaches a local minimum. The snake is parametrically defined as $v(s) = (x(s), y(s))$ where $x(s)$, $y(s)$ are x, y coordinates along the contour and s is $[0, 1]$. The energy functional to be minimized is

$$\begin{aligned} E_{snake} &= \int_0^1 E_{snake}(v(s))ds \\ &= \int_0^1 \left[E_{int}(v(s)) + E_{image}(v(s)) + E_{con}(v(s))\right] ds. \end{aligned} \tag{4.1}$$

The internal spline energy, E_{int}, can be written as

$$E_{int} = \alpha(s) \left|\frac{dv}{ds}\right| + \beta(s) \left|\frac{d^2v}{ds^2}\right|^2, \tag{4.2}$$

where $\alpha(s)$ and $\beta(s)$ specify the elasticity and stiffness of the snake. Note that setting $\beta(s_k)$ at a point s_k allows the snake to become discontinuous at that point and develop a corner. The second term, E_{image}, of the energy integral is derived from the image data over which the snake lies. The third term of energy function serves as an external control over the system. In general this

component is used to draw the snake from a local energy minimum that a higher level process determines as incorrect. In our snake model, the third term E_{con}, is not used and the following combination of forces are used to pull the snake towards lines, and edges:

$$E_{image} = w_{line}E_{line} + w_{edge}E_{edge} + w_{balloon}E_{balloon} + w_{GVF}E_{GVF} \tag{4.3}$$

The line-based functional, E_{line}, is simply defined as:

$$E_{line} = I(x, y) \tag{4.4}$$

where $I(x, y)$ denotes intensity level at image location (x, y). The sign of w_{line} specifies whether the snake is attracted to light or dark lines. The edge-based functional attracts the snake to contours with large image gradients, that is to locations of strong edges:

$$E_{edge} = -\left|\nabla I(x, y)\right|^2. \tag{4.5}$$

Balloon force is an additional pressure force to make snake inflate as a balloon with air inside [118]. It makes the contour have a more dynamic behavior. Balloon force pushes the contour outward until it reaches a strong gradient.

$$E_{balloon} = w_{balloon}\vec{n}(s) \tag{4.6}$$

where $\vec{n}(s)$ is the normal unitary vector to the curve at point $v(s)$. If we change the sign of $w_{balloon}$ or the orientation of the curve, it will have an effect of deflation or inflation. $w_{balloon}$ is chosen smaller than edge weight, w_{edge}, so that an edge point can stop the inflation force.

The gradient vector flow (GVF) was introduced by Xu and Prince [117], [119]. The need for such a force stems from the following deficiencies of a regular edge map. First, the gradient of an edge map has vectors pointing toward the edges, which are normal to the edges on the boundaries. Second, these vectors generally have large magnitudes only in the immediate vicinity of the edges. Third, in the homogeneous regions, where $I(x, y)$ is nearly constant, the gradient of an edge map is nearly zero. The GVF force keeps the gradients

near the edges and extends the gradient map farther away from the edges, improving the convergence in homogeneous regions.

The gradient vector flow field is defined to be the vector field $\mathbf{GVF}(x, y) = (u(x, y), v(x, y))$ that minimizes the energy functional,

$$\varepsilon = \int\int \mu(u_x^2 + u_y^2 + v_x^2 + v_y^2) + |\nabla f|^2 |\mathbf{GVF} - \nabla f|^2 dxdy. \tag{4.7}$$

The snake behavior may be controlled by adjusting w_{line}, w_{edge}, $w_{balloon}$, and w_{GVF}. It was found experimentally that a single setting of these parameters, $\alpha = 0.1$, $\beta = 0.3$, $w_{line} = 1.5$, $w_{edge} = 0.4$, $w_{balloon} = 0.2$ and $w_{GVF} = 0.4$ produced good results on the segmentation of the background.

4.3.2 Automatic Threshold Selection

Thresholding provides us to convert a gray-level image to a binary image. The thresholding operation is defined as

$$I_o(x, y) = \begin{cases} A & \text{for } I(x, y) > \text{Threshold} \\ 0 & \text{otherwise} \end{cases} \tag{4.8}$$

The automatic threshold selection technique used in this study is based on the Nobuyuki's method [115]. To select a threshold for separating the different contents that have small intensity variations, a modified version of the Nobuyuki's threshold selection method is used [98]. In this version, a different separation measurement function is defined to evaluate the "goodness" of the threshold to select an optimal threshold. The pixels of the image that are located in the region of interest (ROI) $(I_{x,y})_{ROI}$ are selected. Suppose there are N gray levels in the ROI of the image I_{ROI}, which is from I_{min} to I_{max}. The gray level distribution (histogram) of the image of ROI is:

$$\begin{aligned} \text{Histogram}(i) = n_i, \quad i \in [I_{min}, I_{max}], \quad I_{min} = \text{MIN}(I_{ROI}), \\ I_{max} = \text{MAX}(I_{ROI}), \end{aligned} \tag{4.9}$$

where n_i is the number of pixels at gray level i. To separate the pixel into two classes ($I_{min} \leq I_1 \leq k$, $k < I_2 \leq I_{max}$), the mean level of each class should be:

$$\text{mean}_1(k) = \sum_{i=I_{min}}^{k} \text{Histogram}(i)/N_1, \quad N_1 = \sum_{i=I_{min}}^{k} \text{Histogram}(i), \tag{4.10}$$

$$\text{mean}_2(k) = \sum_{i=k+1}^{I_{max}} \text{Histogram}(i)/N_2, \quad N_2 = \sum_{i=k+1}^{I_{max}} \text{Histogram}(i). \tag{4.11}$$

The mean level of the ROI is given by

$$\text{mean}_{ROI} = \sum_{i=I_{min}}^{I_{max}} \text{Histogram}(i)/N, \tag{4.12}$$

$$N = \sum_{i=I_{min}}^{I_{max}} \text{Histogram}(i). \tag{4.13}$$

Thus, the probability of each class in the ROI should be

$$P_1(k) = N_1/N, \quad P_2(k) = N_2/N. \tag{4.14}$$

To determine whether k is the best threshold to separate the two classes, a criterion was introduced and named as the *separation measurement function* by the following equation [98]:

$$\begin{aligned} \text{Separation}(k) \quad = \quad & P_1(k) \times P_2(k) \times [(\text{mean}_1(k) - \text{mean}_{ROI})^2 + \\ & (\text{mean}_2(k) - \text{mean}_{ROI})^2], \\ & \text{where } k = I_{min}, \ldots, I_{max}. \end{aligned} \tag{4.15}$$

In the separation measurement function, if k is the best separation threshold, Separation(k) will be at its maximum value. Thus, the threshold selection is an automatic procedure, which searches for a threshold k that maximizes the above function. The optimal $k_{threshold}$ satisfies the following:

$$\text{Separation}(k_{threshold}) = \max_{I_{min} \le k \le I_{max}} \text{Seperation}(k). \tag{4.16}$$

4.3.3 Morphological Processing

The term *morphology* originally comes from the *study of forms* of plants and animals. In our context, we mean study of topology or structure of objects from their images. Morphological processing refers to certain operations where an object is *hit* with a *structuring element* and thereby reduced to a more revealing shape.

Most morphological operations can be defined in terms of two basic operations, *erosion* and *dilation* [120]. Suppose the image $I(x, y)$ and the structuring element $\mathbf{B}$ are represented as sets in two-dimensional space. Let $\mathbf{B}_{x,y}$ denote the translation of $\mathbf{B}$ so that its origin is located at (x, y). Then the erosion of I by $\mathbf{B}$ is defined as the set of all points (x, y) such that $\mathbf{B}_{x,y}$ is included in I, that is,

$$\text{Erosion:} \qquad I \ominus \mathbf{B} \triangleq \{x, y : \mathbf{B}_{x,y} \subset I\}\{x, y : \mathbf{B}_{x,y} \subset I\} \tag{4.17}$$

Similarly, the dilation of I by $\mathbf{B}$ is defined as the set of all points (x, y) such that $\mathbf{B}_{x,y}$ hits I. Thus, they have a nonempty intersection:

$$\text{Dilation:} \qquad I \oplus \mathbf{B} \triangleq \{x, y : \mathbf{B}_{x,y} \cap I \neq \varnothing\} \tag{4.18}$$

Figure 4.4 shows examples of erosion and dilation. Erosion is a shrinking operation, whereas dilation is an expansion operation. It is also obvious that erosion of an object is accompanied by the enlargement or dilation of the background.

In the segmentation algorithm, morphological operations are applied to binary images after thresholding. Erosion and dilation operations are applied sequentially to smooth the boundaries of the segmented objects. They are also used to find the seeds for the segmentation of neighboring tissues from the segmented objects.

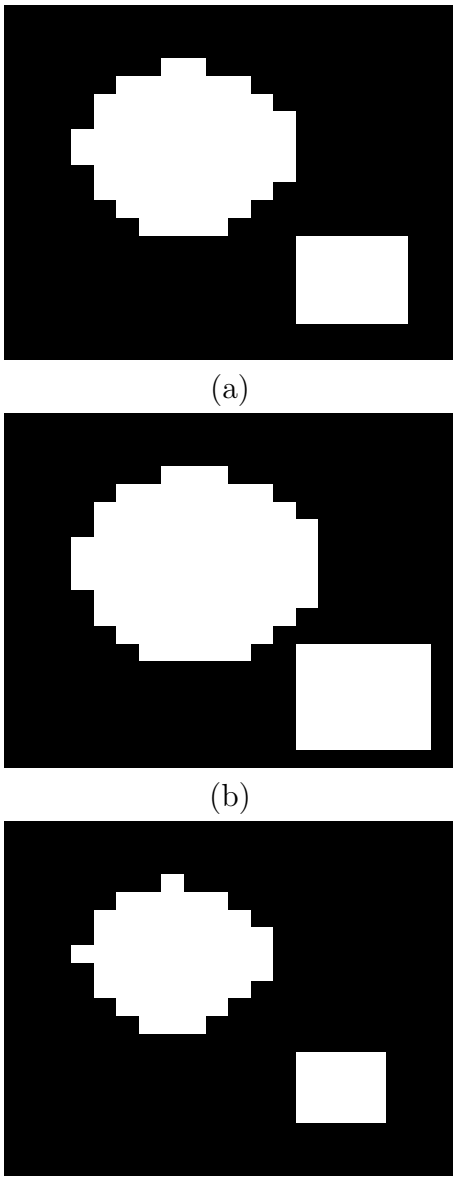

Figure 4.4: Dilation and erosion operations. (a) the original image, (b) dilated image, (c) eroded image.

4.3.4 Region Growing

The basic concept of region growing is to grow a *seed* to combine similar pixels into the region. The input image I is partitioned into subsets $R_1, R_2, \ldots, R_n$ such that [121]:

1. The sets are disjoint, that is, the intersection of sets R_i and R_j is the empty set; and

2. The union of the R_i is I; that is, we classify all pixels through the development of regions..

The image is divided into atomic regions of constant gray levels. Similar adjacent regions are merged sequentially until the adjacent regions become significantly different.

In our segmentation algorithm, the region growing algorithm is applied to binary images. The snakes algorithm, threshoding and morphological operations are applied to 2-D images, that is slices of MR data. To form an image in 3-D, the segmented tissues in all slices are connected by the region growing algorithm.

4.4 Results

The segmentation procedure explained in Section 4.3 was developed using the simulated MR images downloaded from the BrainWeb ([122]). Once the algorithm became capable of identifying the basic features of the head from the simulated images, it is applied to real multimodal MR images. The images were acquired axially using a 1.5 T magnet. The corresponding MR sequence parameters are as follows: TR=540 ms, TE=12 ms for T_1–weighted images, TR=3140 ms, TE=24.9 ms for T_2–weighted images, and TR=3140 ms, TE=87 ms for PD images. All three images were acquired on a single run which removes the need to co-register the images. 12 bit, 256×256 pixel images corresponding to 72 slices of 3 mm thickness are processed.

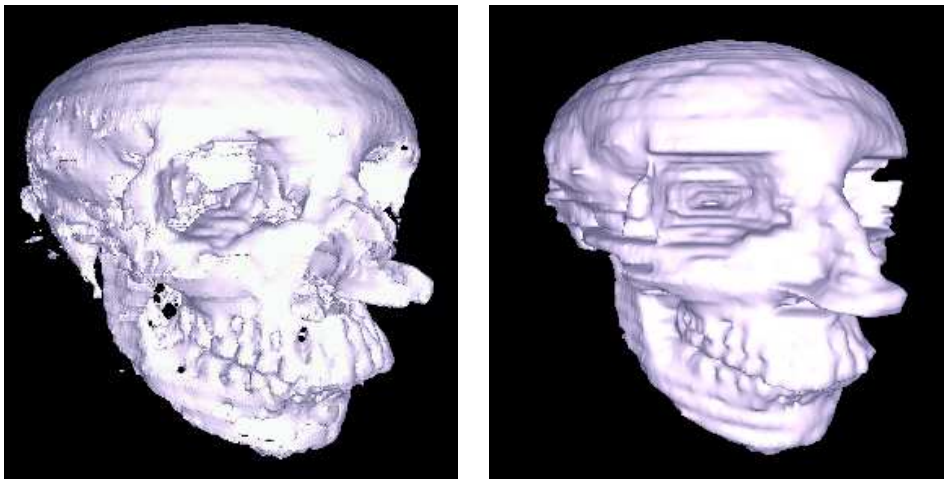

(a) (b)

Figure 4.5: Segmentation of the skull (a) before removing the holes, (b) after removing the holes.

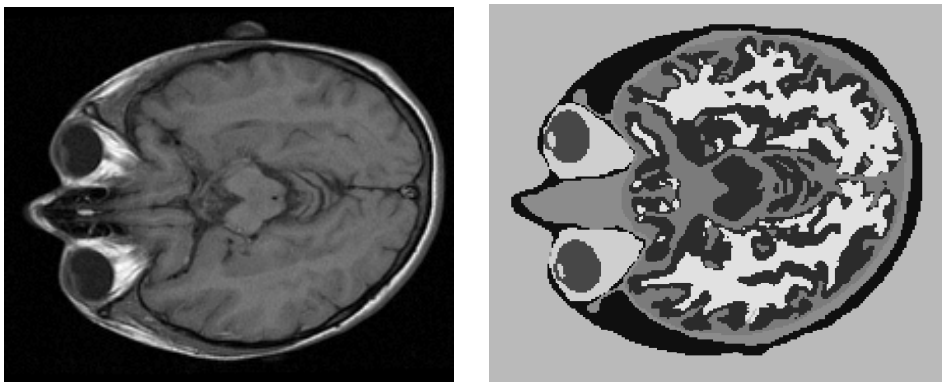

(a) (b)

Figure 4.6: Segmentation of a slice. (a) A slice from T1 image, (b) segmented slice. The sinuses and the skull are segmented together.

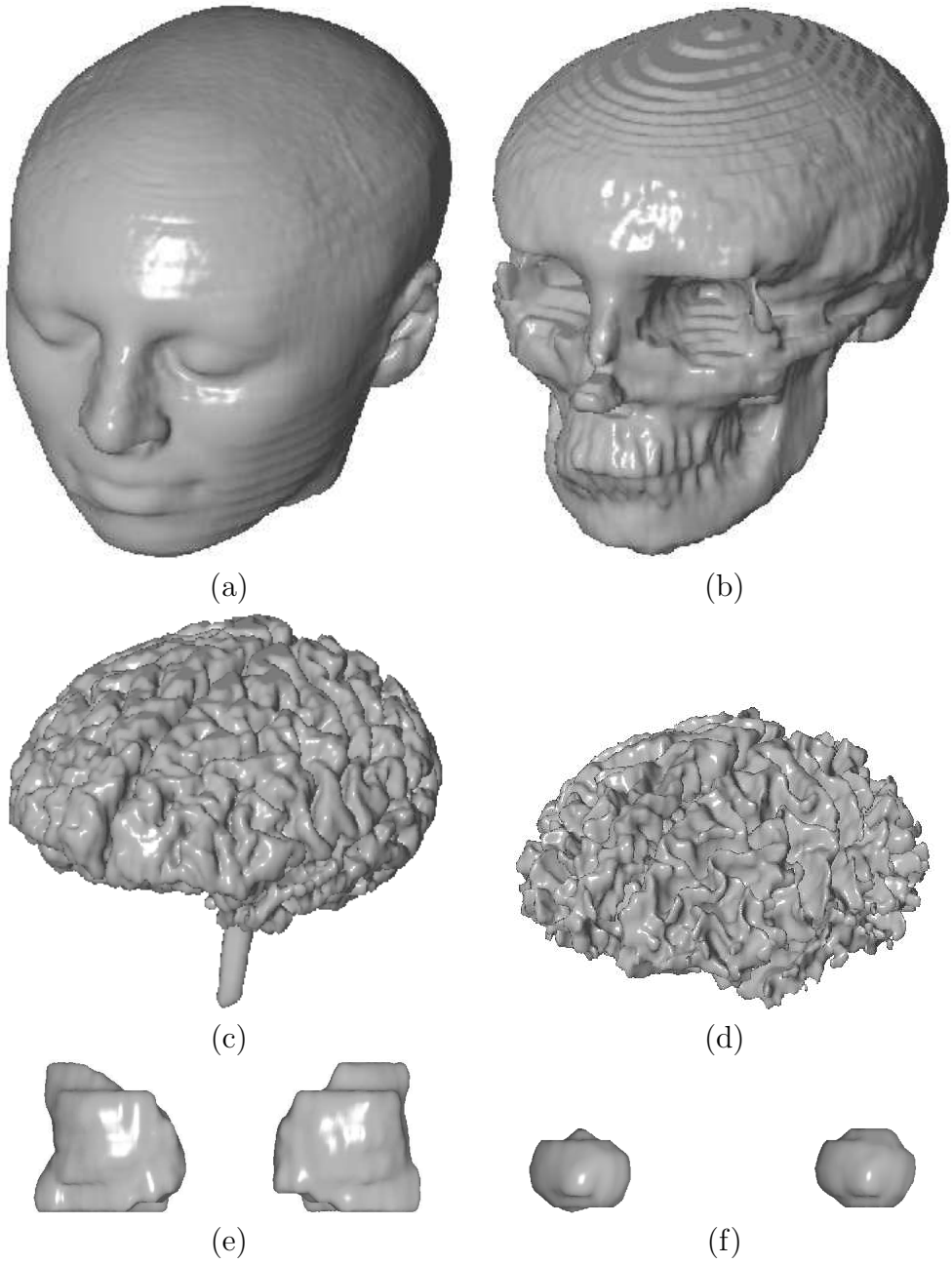

Figure 4.7: Segmented tissues of the whole head (a) scalp, (b) skull, (c) cortex, (d) WM, (e) eyes, (f) eyeballs.

In Figure 4.5, the segmentation of the skull is shown before and after removing the holes. In Figure 4.6, an axial slice from the segmented head is presented. The segmented scalp, skull, cortex, WM, eyes and eyeballs are presented in Figure 4.7. It is observed that the segmentation algorithm is capable of detecting the main tissues of the head with their characteristic features.

CHAPTER 5

REALISTIC HEAD MODELING: THE MESH GENERATION PHASE

5.1 Introduction

Another important step for the forward problem solutions is to obtain numerical meshes that model the head geometry accurately. The geometry information is usually obtained from tomographic images. The meshes used for the BEM solutions model the surfaces (interfaces) between tissues of different conductivities. Usually, they represent the interfaces between the major tissues of the head, such as scalp, skull, and the brain.

In the previous EMSI studies, the meshes are generated by first placing equally distributed nodes on the tissue boundaries and then triangulating these nodes [92], [106]. In those studies, semi-automatic segmentation algorithms were applied to extract the surfaces of scalp, skull, and brain. Some researchers meshed the contour points of the layers at consecutive slices [107], [64], [63], [109]. Early studies constructed BEM meshes by triangulating manually-selected points from T_1–weighted Magnetic Resonance (MR) images [63], [107]. A third group of researchers used free [61] or commercial software packages for mesh generation [110], [111], [113]. In all these models, the first-order (linear) elements were used and the tissues were assumed to be non-intersecting. In this work, we used Adaptive Skeleton Climbing (ASC) [123], filtering and coarsening operations to obtain a mesh with linear elements. We obtained quadratic elements during a second coarsening process. To include

eye tissues into the model, we generated intersecting meshes for outer skull and eyes.

5.2 The Mesh Generation Algorithm

In this section, first the generation of the individual meshes for each layer then the mesh generation algorithm used for intersecting surfaces will be presented.

5.2.1 Generation of Individual Meshes

The flowchart of the mesh generation algorithm is shown in Figure 5.1. To obtain a mesh from the segmentation data, first the ASC algorithm is used for triangulation. This algorithm places one or more triangles in each boundary voxel. The triangulated surface is then smoothed using a surface signal low-pass filter algorithm [9]. Thus, the high frequencies caused by noise and the slice effect of the MR images are suppressed. During the smoothing process, the vertices of the triangulated surface are moved but the connectivity of the faces remains unchanged. The number of triangles is reduced using a coarsening algorithm based on iterative edge contraction and quadric error metrics [10]. At every step of coarsening, the neighbor nodes with lowest errors are connected together and a coarse mesh is obtained. The resulting mesh may contain some undesirable topological artifacts, such as disconnected or multiply connected components and singular nodes. These artifacts are corrected to create a single manifold surface that represents the given boundary [124].

To obtain a coarse mesh with second-order elements from a dense mesh with first-order elements, a modified coarsening process is applied. For this purpose, additional nodes are generated at the edges of each first-order element. The modified coarsening algorithm takes these additional nodes into account and fits them to the original surface defined by the dense mesh. When the common edge of the two elements contracts (i.e., an edge becomes a node), the middle nodes of the neighboring elements are moved to fit the original surface. As a result, the element groups of the fine mesh are represented by a fewer number of quadratic elements.

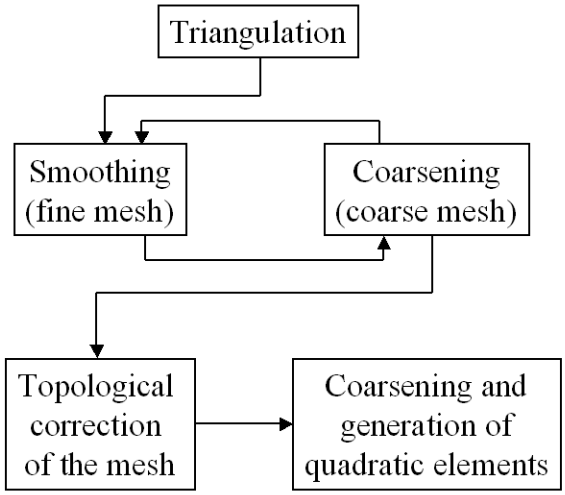

Figure 5.1: The flowchart of the mesh generation algorithm.

In the head geometry, where the CSF is very thin, the cortex and the skull may touch each other. Thus, those regions may intersect during mesh generation. Such regions are automatically detected and the corresponding nodes are perturbed in their normal directions to prevent intersections.

5.2.2 Mesh Generation for Intersecting Surfaces

In the previous BEM studies, the boundaries have been represented as closed, non-intersecting surfaces. However, in the actual head, this is not always the case (for example, eyes, tumors, implanted plaques, etc.). In this section, the mesh generation approach for intersecting surfaces will be explained for eye tissues.

When the eyes are to be included in the model, the skull-scalp interface can no longer be assumed as a closed surface. In such a case, there are skull-eye, skull-scalp, and eye-scalp interfaces. In this study, the outer and inner surfaces of the skull are obtained (using the snakes algorithm) as closed surfaces from the segmented image data. Meshes are then created for the inner and outer surfaces of the skull, and for the two eyes, separately. An automatic algorithm is applied to the intersecting surfaces of the outer-skull and eyes to form a single mesh of skull and eyes [125].

The flowchart of intersecting meshes algorithm is given in Figure 5.2.It can

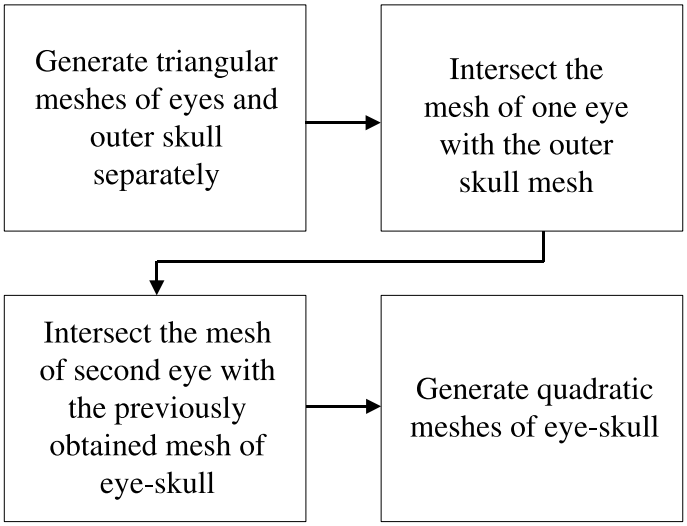

Figure 5.2: The flowchart of the algorithm for intersecting meshes.

be summarized as follows :

1. Find the intersections between the surfaces of skull and one eye,
2. determine a closed loop from the intersection of the line segments,
3. remove all the triangular elements of the intersection loop,
4. generate intermediate nodes along the intersection loop,
5. identify disjointed patches of the triangular elements,
6. remove the elements of the skull that remain in the eye region,
7. generate new elements using advancing front technique [126] by selectively picking individual surface parts.

To obtain the mesh of the skull and eyes, first one eye is intersected with the skull, and then the other eye is intersected with the previously obtained skull-eye mesh.

5.3 The Algorithms used in Mesh Generation

To explain the algorithms used in mesh generation we have to make some definitions. We represent a triangular surface as a pair of lists $S = \{V, F\}$, a

list of n vertices V, and a list of triangular faces F. Both for curves and for surfaces, a *neighborhood* of a vertex v_i is a set i^* of vertex indices. If the index j belongs to the neighborhood i^*, we say that v_j is a *neighbor* of v_i.

The most widely used neighborhood structure is the *first order neighborhood*. In this structure, each pair of vertices that share a face (or an edge, for a curve) are assigned as neighbors of each other. This is the neighborhood structure used in this work.

5.3.1 Triangulation

Triangulation is the process of generating an iso-surface from the volume data. A well-known algorithm for triangulation is the marching cubes algorithm [127]. The algorithm places one or more triangles into each boundary voxel. For this reason very large number of triangles are generated at the end of the triangulation step. This study uses the ASC algorithm to form the initial triangular mesh for each surface [123]. ASC generates 4 to 25 times fewer triangles compared with the marching cubes algorithm.

By climbing from vertices (0-skeleton) to edges (1-skeleton) and to faces (2-skeleton), the algorithm construct boxes which adapt to the geometry of the true iso-surface. The algorithm consists of four steps: 1) Volume analysis, 2) construction of simple boxes, 3) sharing information between adjacent boxes, and 4) iso-surface extraction.

The first step of the ASC algorithm is volume analysis to determine smooth regions in the volume. The volume is analyzed first in 1D, by trying to find a linear sequence of voxels with a *simple structure*. Then the structures are investigated in 2D to locate size-maximal rectangular regions of voxel samples with simple structure. The result of the volume analysis step is a set of data structures that describe 2D maximal rectangular regions within each layer of the volume.

The next step is the construction of simple boxes from 1D and 2D data. The rectangles computed in the previous step are considered in layers to form a set of maximal boxes. The boxes contain information to generate iso-triangles

within each box. The algorithm contains a parameter N that defines the maximum height of a box. This parameter limits the maximum size of a box, thus providing an indirect control on the detail of the mesh.

At this step, it is possible to generate a triangular mesh using the boxes, the mesh may contain *cracks* due to mismatches between the rectangles. To prevent the cracks in the mesh, information must be shared among adjacent boxes.

The final step of ASC is to generate iso-surfaces from the computed data structures. First 3D vertices and edges are computed, forming edge-loops. Possible ambiguities that may arise when generating the edges are resolved by sub-sampling. The insides of the edge-loops are then triangulated to form the triangular iso-surface.

The triangular mesh generated from the volume data from ASC still needs to be processed and further coarsened to be useful as a BEM mesh. These operations are described in the following sections.

5.3.2 Smoothing

Smoothing is a low pass filtering process that is used to reduce the noise and other artifacts, such as the staircase effect of MRI after the segmentation and triangulation processes. This process results in a more continuous mesh surface, and improves the quality of the subsequent coarsening process. In this study, the smoothing algorithm of Taubin [9] is used. Taubin represented a polyhedral surface as a two-dimensional discreet surface signal and by applying Fourier analysis he reduced the problem of smoothing to surface signal low-pass filter algorithm.

A discrete surface signal is a function $v = (v_1, \ldots, v_n)^t$ defined on the vertices of a polyhedral surface. We define the discrete Laplacian of a discrete surface signal by weighted averages over the neighborhoods

$$\triangle v_i = \sum_{j \in i^*} w_{ij}(v_j - v_i), \tag{5.1}$$

where the weights w_{ij} are positive numbers that add up to one for each i. The

weights can be chosen in many different ways taking into consideration the neighborhood structures.

One particularly simple choice that produces good results is to set w_{ij} equal to the inverse of the number of neighbors $1/|i^*|$ of vertex v_i, for each element j of i^*. In our implementation, a more general way is used for choosing weights. For a surface with a first order neighborhood structure, a positive function $\phi(v_i, v_j) = \phi(v_j, v_i)$ is defined on the edges of the surface:

$$w_{ij} = \frac{\phi(v_i, v_j)}{\sum_{h \in i^*}} \phi(v_i, v_j). \tag{5.2}$$

The function ϕ can be the surface area of the two faces that share the edge, or some power of the length of the edge $\phi(v_i, v_j) = |v_i - v_j|^\alpha$. In this study, edge length is used with $\alpha = -1$, which according to [9], produces good results.

Figure 5.3 presents a triangulated spherical surface, where noise is added to one half of the sphere. As iterations progress, the half surface without noise does not change significantly and noise is removed from the noisy part.

5.3.3 Coarsening

The triangulation results in a surface mesh that has a large number of vertices. Directly using these surfaces as the BEM mesh is not possible due to memory and computation constraints. Therefore, the number of triangles and vertices must be reduced to an acceptable size, without destroying the structure and details of the mesh in the process.

The coarsening algorithm used in this work is an iterative edge contraction method. Every edge is assigned a cost which is the error resulting from its contraction. At each iteration, the lowest-cost edge is extracted and contracted. The error metric offers a compromise between very fast low quality methods and very slow high-quality methods [10], [128]. The coarsening implementation is based on QSlim software [129].

The fundamental operation of the algorithm is edge contraction, which we will write $(\mathbf{v}_1, \mathbf{v}_2) \rightarrow \bar{\mathbf{v}}$. To perform this simple contraction, we need to perform the following three steps: (1) move vertices $\mathbf{v}_1$ and $\mathbf{v}_2$ to the position $\bar{\mathbf{v}}$, (2)

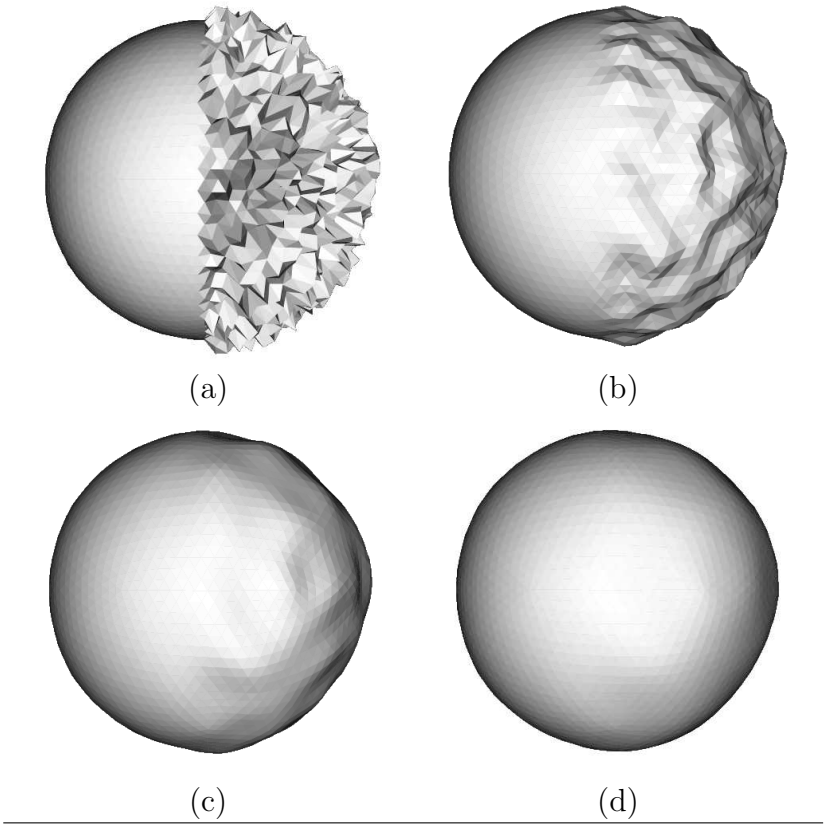

Figure 5.3: (a) Spherical surface partially corrupted by white noise, (b) after 10 steps of smoothing, (c) after 50 steps of smoothing, (d) after 200 steps of smoothing. (This figure is reproduced from [9].)

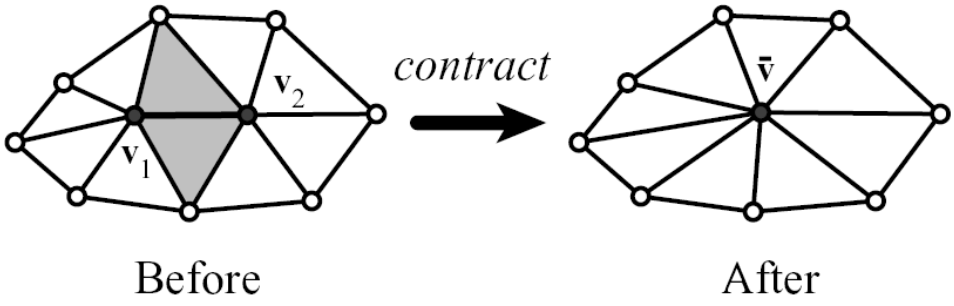

Figure 5.4: Contraction of an edge. (This figure is reproduced from [10].)

replace all occurrences of $\mathbf{v}_2$ with $\mathbf{v}_1$, and (3) delete $\mathbf{v}_2$ and any degenerate faces. Figure 5.4 illustrates the effect of a single edge contraction.

5.3.3.1 Basic Quadric Error Metric

The error at each vertex is defined to be the sum of squared distances of the vertex to all planes in its set. Each set is initialized with the faces incident to the corresponding vertex in the original model. When an edge is contracted into a single vertex, the resulting set is the union of the two sets associated with the endpoints. Each face in the original model defines a plane which satisfies the equation $\mathbf{n}^T\mathbf{v} + d = 0$, where $\mathbf{n} = [n_x \ n_y \ n_z]^T$ is a unit normal and d is a constant. The squared distance of a vertex $\mathbf{v} = [x \ y \ z]$ to this plane is given by

$$D^2 = (\mathbf{n}^t\mathbf{v} + d)^2 = \mathbf{v}^T(\mathbf{n}\mathbf{n}^T)\mathbf{v} + 2d\mathbf{n}^T\mathbf{v} + d^2. \tag{5.3}$$

This can also be represented conveniently using the *quadric* Q:

$$Q = (\mathbf{A}, \mathbf{b}, c) = (\mathbf{n}\mathbf{n}^T, d\mathbf{n}, d^2)$$
$$Q(\mathbf{v}) = \mathbf{v}^T\mathbf{A}\mathbf{v} + 2\mathbf{b}^T\mathbf{v} + c.$$

The addition of quadrics can be naturally defined componentwise: $Q_1(\mathbf{v}) + Q_2(\mathbf{v}) = (Q_1 + Q_2)(\mathbf{v})$, where $(Q_1 + Q_2) = (\mathbf{A}_1 + \mathbf{A}_2, \mathbf{b}_1 + \mathbf{b}_2, c_1 + c_2)$. Thus, to compute the sum of squared distances to a set of planes, only one quadric which is the sum of the quadrics defined by each of the individual planes is sufficient.

And when contracting the edge $(\mathbf{v}_1, \mathbf{v}_2)$, the resulting quadric is merely the sum $Q = Q_1 + Q_2$. Furthermore, the cost of a contraction $(\mathbf{v}_1, \mathbf{v}_2) \rightarrow \bar{\mathbf{v}}$ can be defined as the error at $\bar{\mathbf{v}}$ which is $Q(\bar{\mathbf{v}}) = Q_1(\bar{\mathbf{v}}) + Q_2(\bar{\mathbf{v}})$.

5.3.3.2 Vertex Placement

When considering the contraction of an edge $(\mathbf{v}_1, \mathbf{v}_2)$, there is a need to choose the target position $\bar{\mathbf{v}}$. For that purpose, there are two primary policies and these will be explained next.

Subset placement is the simplest strategy that can be adopted. In this technique, one of the endpoints is selected as the target position. In other words, one endpoint is contracted into the other. To choose between the endpoints, finding the smaller of $Q(\mathbf{v}_1)$ and $Q(\mathbf{v}_2)$ is sufficient. Under this policy, any approximation will use a subset of the original vertices in their original positions.

A better approximation can be produced using the *optimal placement* technique. For a given quadric Q, the point $\bar{\mathbf{v}}$ is located such that $Q(\bar{\mathbf{v}})$ is minimal. Since $Q(\bar{\mathbf{v}})$ is quadratic, finding its minimum is a linear problem; the minimum occurs where $\partial Q/\partial x = \partial Q/\partial y = \partial Q/\partial z = 0$. By solving this system of equations, the optimal position and its error are given by:

$$\bar{\mathbf{v}} = -\mathbf{A}^{-1}\mathbf{b} \qquad \textit{and} \qquad Q(\bar{\mathbf{v}}) = -\mathbf{b}^T\mathbf{A}^{-1}\mathbf{b} + c \tag{5.4}$$

Of course, the matrix $\mathbf{A}$ may not be invertible. In other words, there may be infinitely many minimal points. In this case, subset placement can be used as a fall-back strategy. Also other intermediate policies such as selecting between the endpoints and the midpoint, or searching for the optimal position along the edge can be considered.

For the BEM mesh generation, since geometrical accuracy is important, the *optimal placement* strategy is used. The basic coarsening procedure is enhanced to keep track of the mid points of the edges, thus generating curved, quadratic elements through successive coarsening steps. This makes it possible to further reduce the number of elements through coarsening without

sacrificing geometrical accuracy.

5.3.4 Topological correction

Topological singularities and inconsistencies may arise during the course of mesh generation process. An example of singularity is a *singular edge* where more than two triangles are incident on the edge. Smoothing and mesh intersection steps require topologically correct surfaces and may produce undesirable results if presented with a non-manifold surface. Furthermore the accuracy of the BEM solution may suffer when the underlying mesh has singularities. The aim of the topological correction step is to generate a single manifold surface for each component of the BEM mesh.

An efficient method for automatically converting a non-manifold surface to a manifold surface was described by Guéziec *et al* [124]. The method consists of two high-level algorithms: cutting and stitching. Cutting identifies the singular vertices and edges in the mesh, and removes the singularities by duplicating necessary edges, in effect cutting through the mesh. At the end of cutting, the mesh may contain disconnected components. The stitching step reconnects these components while making sure that the result is a manifold surface. The algorithms only use the surface connectivity information and do not depend on the underlying physical coordinates.

In this work, the local version of the *cutting* algorithm described by Guéziec *et al* is used [124]. The local cutting algorithm proceeds as follows:

Identify singular edges: In this step, all edges are recorded, and singular edges, i.e., edges with more than two adjacent faces, are marked.

Identify isolated singular vertices: On an isolated singular vertex, it is not possible to reach all adjacent faces when moving from face to face, around the vertex. To identify such vertices, for each vertex v, the v^*, i.e. the set of all adjacent faces is constructed. Then, starting with an arbitrary face f in v^* the adjacent faces are traversed. If the number of traversed faces is less than the size of v^* then the vertex is singular.

Local Cutting Algorithm: Starting with the singular edges marked in the first step, the endpoints of the edges are added to the list of singular vertices computed in step 2. For each marked singular vertex v, faces in v^* are classified into reachable sets. In this context, reachable means that two faces in a set share an unmarked edge. Once the number of sets is known, the vertex is *multiplied* and each set is associated with a different copy of the vertex. The algorithm ends when every marked vertex is multiplied.

Correct Orientation of the Faces: The orientation (direction of the surface normals) of the faces must be correct, for BEM computations. For orientation to be consistent, the vertices of each edge must be listed twice in different orders. After cutting, this is verified and incorrectly oriented faces are flipped.

The stitching part of the method is not used in this study. Small disconnected mesh components are discarded as they correspond to the noise in the segmented volume, or errors in triangulation. The remaining parts are joined by the coarsening process.

5.4 Results

The mesh generation algorithm that use triangulation, smoothing, and coarsening operations are applied to the segmented volumes of scalp, skull, cortex, eyes and eyeballs. The meshes of the scalp, skull, cortex and WM with 4000 elements are shown in Figure 5.5. The algorithm described in Section 5.2.2 is applied for the intersecting surfaces of the eyeballs and skull layers. Figure 5.6 (a) shows the skull and the eye meshes. In Figure 5.6 (b) the intersected mesh of skull and eyes is presented. After coarsening and quadratic mesh generation steps, the mesh for the whole head is generated. An axial figurative representation of the layers in the head is given in Figure 5.7. Note that, while the boundaries of the outer skull and the eye tissues intersect, the individual surface segments form closed boundaries for each tissue, which allows the tissue

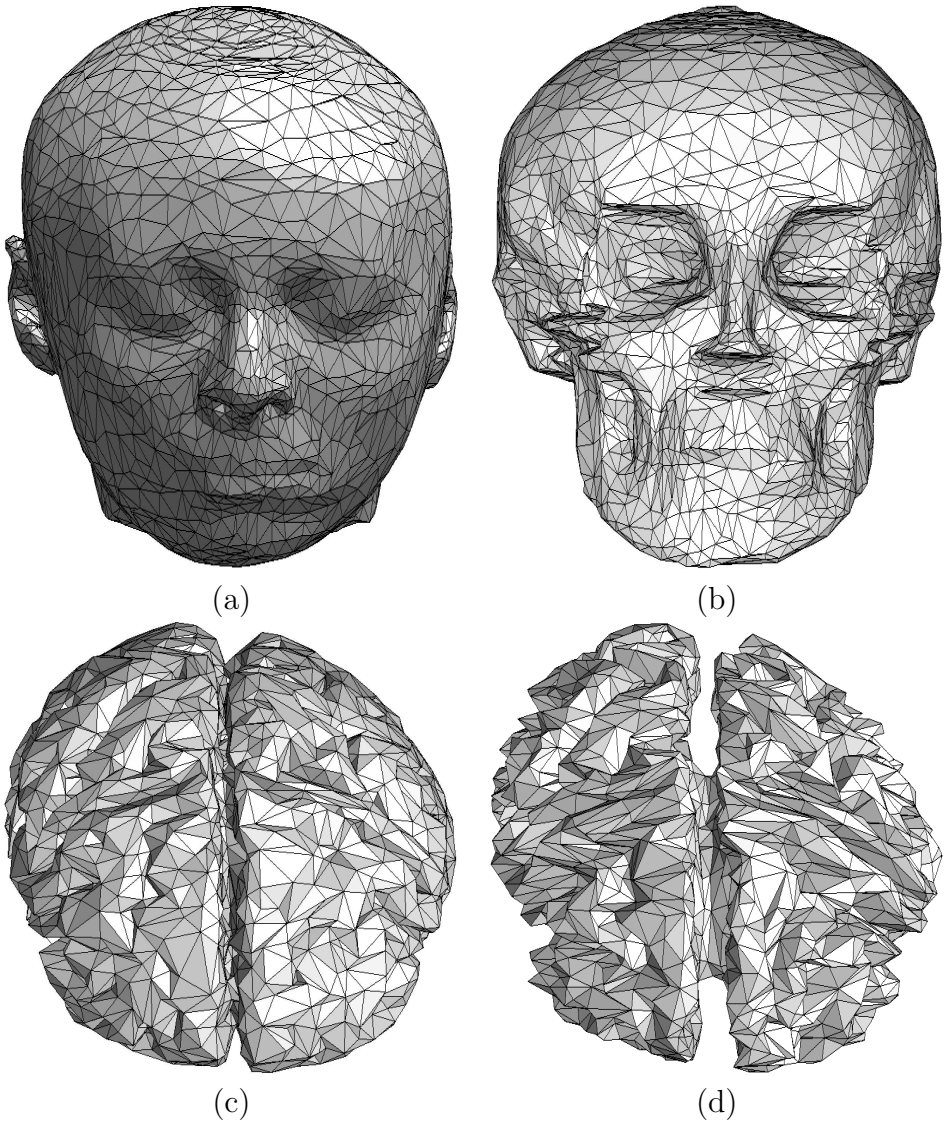

Figure 5.5: The meshes generated for (a) scalp, (b) skull, (c) cortex and (d) white matter. All layers are represented using 4000 elements.

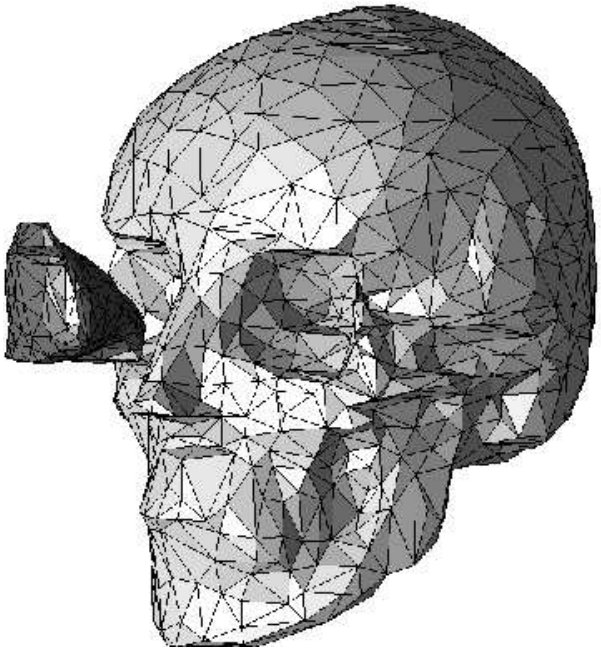

(a)

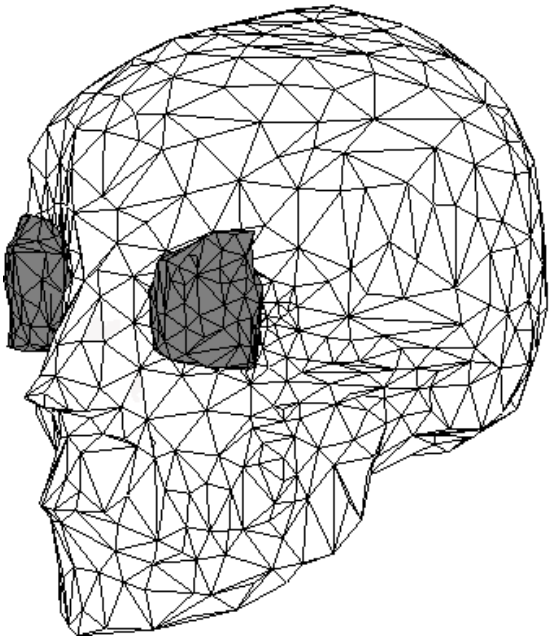

(b)

Figure 5.6: The mesh of the outer skull and eye tissues (a) before intersection (b) after intersection. The mesh contains 2003 elements.

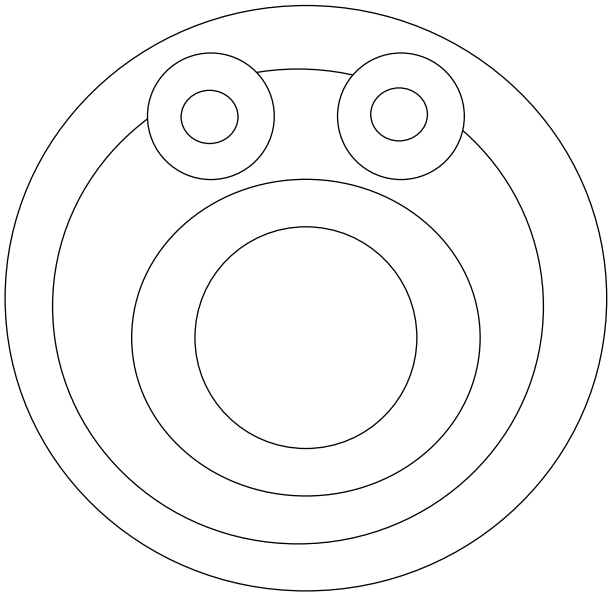

Figure 5.7: A figurative representation of the head mesh.

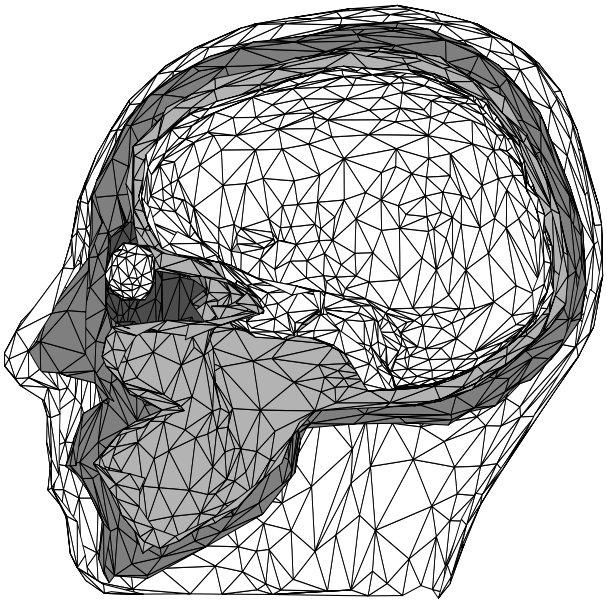

Figure 5.8: Cut-away view of the BEM mesh showing the inner layers. For simplicity in illustrations the quadratic elements of the mesh are displayed as linear elements.

compartments to be represented by the BEM formulation.

Figure 5.8 shows the cut-away view of the mesh that models eyes, scalp, skull, CSF and brain. The mesh contains 9906 nodes and 4984 elements, and is the most detailed and complete BEM mesh that have been published. The quadratic curved elements of the mesh, generated using the successive-coarsening process, and the ability to model intersecting tissue boundaries are the distinguishing features of the mesh generation process and contributes to the improved accuracy of the BEM solution.

CHAPTER 6

REGISTRATION OF MRI AND EEG DATA

6.1 Introduction

Registration of MEG/EEG data with 3D MRI data is an important step in the EMSI problem. The combination of EEG/MEG and MRI data, requires the registration of both modalities, i.e. the transformation of electrode positions and MRI data into a single coordinate system. The registration step is a source of error which, for the worse cases, may be greater than errors related to the localization algorithms.

Several registration methods are proposed in the literature. One of them is based on matching the reference points marked during the acquisition of both EEG and MRI [130]. A standard approach is the use of well known anatomical points as landmarks or placing fiducial landmarks as reference points. The anatomical landmarks are chosen as nasion, left and right preauricular points, or inion [131]. The external fiducial markers are generally chosen as rigid devices containing oil-filled markers attached to the head, masks, dental bite bars, etc. [132]. These methods are computationally fast however, due to the small number of reference points, even a small measurement error can result in a considerable error of transformation. And this small measurement error is unavoidable because they deal with a large area in the MR image to align. Use of fiducial markers may also cause discomfort to the patient.

Another approach utilizes the visualization of electrode positions during the MRI by temporarily positioning MRI visible markers at the electrode sites

[133]. This approach does not require the alignment routine. However, it is time consuming and requires that the MRI scan be done soon after the EEG session. Furthermore, a new MRI scan is needed for every EEG recording.

A third approach for registration of EEG and MRI data is based on matching a set of digitized head-surface points to the segmented volume images of the head surface [134], [135], [71]. Points, lines or surfaces of the two data sets are used to find the best fit between the two objects. The advantage of this method is that only one MRI data set is needed, even with multiple EEG sessions. It does not require any fiducial markers and it does not suffer from difficulties or uncertainties of locating anatomical landmarks.

In this study the third approach is adopted. A fully automatic surface matching method is implemented and it is verified with simulation studies and using experimental data. The registration procedure matches the skin surface, segmented from MRI, and a digitized version of the head obtained using a Polhemus Fastrak digitizer. An optimization problem is solved to minimize the total distance between the two data sets, by changing the relative position and orientation of the sets. Six parameters, which are rotations around x, y and z axis, and three translation parameters along these axes, are determined that minimize the distance between the models.

6.2 The method

In our notation, the rotation parameters are represented by α_x, α_y, and α_z and the translation parameters by t_x, t_y, and t_z. The formulation for the translation and rotation can be given as follows:

Translation:

$$\begin{aligned} x' &= x + t_x \\ y' &= y + t_y \\ z' &= z + t_z \end{aligned} \tag{6.1}$$

Rotation around x axis:

$$\begin{bmatrix} x' \\ y' \\ z' \end{bmatrix} = \begin{bmatrix} 1 & 0 & 0 \\ 0 & cos(\alpha_x) & -sin(\alpha_x) \\ 0 & sin(\alpha_x) & cos(\alpha_x) \end{bmatrix} \begin{bmatrix} x \\ y \\ z \end{bmatrix} \tag{6.2}$$

Rotation around y axis:

$$\begin{bmatrix} x' \\ y' \\ z' \end{bmatrix} = \begin{bmatrix} cos(\alpha_y) & 0 & sin(\alpha_y) \\ 1 & 0 & 0 \\ sin(\alpha_y) & 0 & cos(\alpha_y) \end{bmatrix} \begin{bmatrix} x \\ y \\ z \end{bmatrix} \tag{6.3}$$

Rotation around z axis:

$$\begin{bmatrix} x' \\ y' \\ z' \end{bmatrix} = \begin{bmatrix} cos(\alpha_z) & -sin(\alpha_z) & 0 \\ sin(\alpha_z) & cos(\alpha_z) & 0 \\ 1 & 0 & 0 \end{bmatrix} \begin{bmatrix} x \\ y \\ z \end{bmatrix} \tag{6.4}$$

The rigid body transformation F of an object is defined as follows:

$$F(p) = \mathbf{R}(p - \mathbf{c}) + \mathbf{c} + \mathbf{t} \tag{6.5}$$

for each point $p = [x, y, z]^T$ of the object. The matrix $\mathbf{R}$ is the rotation matrix, the vector $\mathbf{c} = [c_x, c_y, c_z]^T$ is the center of rotation, and $\mathbf{t} = [t_x, t_y, t_z]^T$ is the translation. The rotation matrix $\mathbf{R}$ is the product of the three matrices given in equations Equation (6.2), Equation (6.3) and Equation (6.4).

Let us denote the head surface derived from MRI volume as S_r, the reference object, and S_d as the digitized head surface points. For registration, we will try to find a transformation F such that $F(S_d) = S_r$. The alignment error that will be minimized is defined as follows:

$$e(\Pi) = \sum_{i=1}^{N} d^2(S_d, S_r) = \sum_{i=1}^{N} d^2(F(p_i, \Pi), S_r) \tag{6.6}$$

where $\Pi = (t_x, t_y, t_z, \alpha_x, \alpha_y, \alpha_z)$ is a vector of transformation parameters in 3D space and p_i is the set of points of S_d, where $i = 1, \ldots, N$. The function $d^2(S_d, S_r)$ is the squared minimum distance between the transformed digitizer points and the reference model.

To minimize the function $e(\Pi)$ we used the steepest descent method for the least squares estimation of non-linear parameters.

Table 6.1: Simulated Registration Results: The average error after registration using different number of sensors with different orientation and noise.

no of sensors	SNR	translation (mm)	rotation (degrees)	average error
48	∞	tx=-20, ty=20, tz=20	0	12.9 nm
48	∞	0	$\alpha_x = 20$	50 nm
485	∞	0	$\alpha_x = 20$	1.1 nm
48	20	0	$\alpha_x = 20$	0.35 mm
485	20	0	$\alpha_x = 20$	0.42 mm

6.3 Results

This section presents the results related to the registration of the electrode positions with the head model, using the described algorithm. First, simulated electrode coordinates are used to develop and test the algorithm. Then, real electrode positions obtained using a digitizer are registered to the scalp surface obtained from the segmentation and mesh generation steps (as described in Chapters 4, 5).

6.3.1 Simulations

During the development and testing of the algorithm, first, simulated electrode coordinates are used. The digitizer points are simulated using the nodes of the scalp mesh. These nodes are rotated and translated to generate mismatch between sensor locations and MRI data. The generated sensor coordinates are perturbed by adding uniform noise with an SNR of 20, where SNR is defined as the ratio of the standard deviation of coordinates, to the variance of the noise. Registration is done with noisy and noise free digitizer points. The effect of the number of digitizer points is investigated by using different number of points in the registration. In Table 6.1 the results of the simulation study are presented. Figure 6.1 illustrates the first case (row) in Table 6.1 showing the simulated digitizer points and the head mesh. It can be seen that the registration algorithm successfully reconstructed the original points.

The results show that the registration algorithm is capable of reversing translation and rotation even when the sensor coordinates are perturbed by

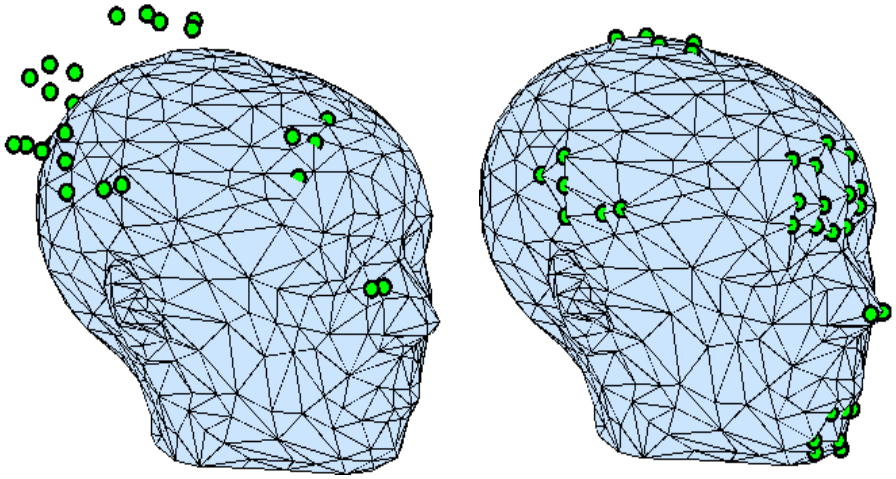

(a) (b)

Figure 6.1: Illustration of registration of simulated noise free digitizer points to MRI data. (a) Before registration, (b) after registration.

noise. The accuracy is below 1 mm for a signal to noise ratio of 20. As long as the sensors are uniformly distributed over the head surface, a small number of digitized points is sufficient for correct registration.

6.3.2 Realistic mapping

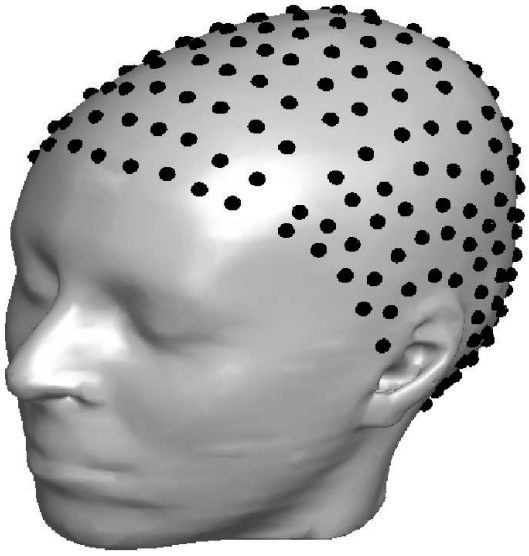

Figure 6.2: Registration of measured electrode positions to the segmented scalp surface. The locations of the 256 electrodes on the head surface.

The electrode positions are acquired using a Polhemus/Fastrak digitizer from a 256-electrode Neuroscan cap fitted onto the subject's head. The dig-

itized points are fitted onto the scalp surface of the head model using the algorithm described on the previous sections. When minimizing the distance from the electrodes to the scalp mesh, the minimum distance to the quadratic element surfaces is computed at each step for each electrode.

The electrode positions registered on the head are shown in Figure 6.2. It can be seen that the head model constructed from MR images through segmentation and mesh generation stages fits into the digitized electrode coordinates acquired from the same subject. The average distance between the head surface and electrodes is less than 1 mm after the registration. After the registration is complete, the electrodes are moved onto the nearest mesh surface.

CHAPTER 7

THE INVERSE PROBLEM OF EMSI

7.1 Introduction

Localization of the electrical sources from measured scalp potentials and magnetic field measurements are called the inverse problems of the Electrical Source Imaging and Magnetic Source Imaging, respectively. In this study, a specific inverse problem technique, the genetic algorithm (GA) is adopted in solving the inverse problem. The basic operations of the GA and the improvements to the basic GA are introduced. The GA is a global optimization algorithm which requires a large number of forward problem solutions during the course of the execution. The use of the accelerated BEM formulations, described in the previous chapters (Chapters 2 and 3), make it possible to use the GA with realistic BEM head models despite the high number of solutions required by GA. The advantage of GA, compared with other search based methods, is the ability to avoid local minima to find the global optimum solution. Furthermore, the GA operations act on independent chromosomes allowing the GA to scale to large number of processors, with minimum overhead. This work attempts to further improve the convergence speed of the GA by adding a local optimization step at the end of each iteration (generation). This improves the parameters of the best member and accelerates convergence. In addition, only the location of the dipoles are searched, effectively placing three orthogonal dipoles at each location parameters. The orientation of the dipole is derived linearly by searching the optimum magnitudes for the triad of dipoles. When

using the GA with experimental data (i.e., the auditory evoked potentials, the a priori knowledge that the dipoles are symmetric around the axis that divides the two hemispheres of the brain further reduces the number of parameters in the search (i.e., only three parameters are searched for each dipole pair).

The GA has been previously applied to EMSI source localization by several researchers. The details of these studies are summarized in Section 7.4. The GA was implemented for ESI [136] and MSI [137], [138], [139]. Single layer BEM models [137], [138] or homogeneous sphere [136] were used as a head model. Nagano *et al* used two cubic lattices as a search space [139]. This work uses both analytical concentric spheres model and a detailed multilayer realistic BEM model as forward models to GA for solving the ESI inverse problem.

In this chapter, different EEG/MEG source localization procedures are reviewed. The inverse problem solution approaches and algorithms are presented in two categories: parametric methods and imaging methods. Choice of the number of sensors and the choice of the reference electrode in electrical source imaging are discussed. In the results section, first, the performance of the GA is exploited using simulated data with Monte-Carlo simulations. Next, the results for experimental data (i.e., ESI for auditory evoked potentials) will be presented.

7.2 The Inverse Problem Approaches

The functional organization and the working mechanisms of the brain has been an intriguing research area. Various techniques, such as the Single Photon Emission Tomography (SPECT), Positron Emission Tomography (PET), and Functional Magnetic Resonance Imaging (fMRI) have been developed for understanding the functions of different brain regions [140]. This research is complicated by the fact that in a functional process more than one region of the brain is active. Furthermore, some brain regions have more than one task. The functions are results of interactions between large neural networks, and the role of a brain region in this network is determined by dynamic interaction

between several regions. To investigate this dynamical nature of the brain, the neural activity must be measured in real time. The main problem of the existing functional imaging techniques is the low time resolution. For instance, PET images have spatial resolutions as high as 2 mm. The temporal resolution, however, can be as high as several minutes. fMRI identifies the functional regions by measuring blood oxygenation level dependent (BOLD) changes. In addition to limited temporal resolution, regions of BOLD changes in fMRI images do not necessarily correspond one-to-one with regions of electrical neural activity [14].

MEG and EEG are two complementary techniques that measure, respectively, the magnetic field outside the head and the scalp electric potentials produced by electrical activities of the human brain due to body functions. EEG and MEG can be used via function related experiments to identify regions of related brain activity [14], [72], [73], [74]. Since EEG and MEG directly measure electrical brain activity, they offer superior temporal resolution when compared to PET or fMRI. Unfortunately, the spatial resolution of EMSI is usually lower than that of PET and fMRI.

The source of the electrical activity in the brain is usually modelled by electrical dipoles and the purpose of EMSI is to obtain information about the spatio-temporal behavior of these dipoles. Assuming a head model, an essential part of obtaining EMSIs is the solution of the electric and magnetic fields (the forward problem) for a given dipole configuration . The solution of the inverse problem (i.e., given the measured data, finding the location and direction of dipoles) is based on the comparison of the measured and calculated fields. The relation of these two problems are shown in Figure 7.1.

In 1853, Helmholtz claimed that a number of source configurations may give rise to the same potential distributions over the scalp [66]. On the other hand, different field distributions can only be achieved by different sources. Thus, the first step in understanding the activity of different neural groups is to measure the difference in the field distributions. The only way to eliminate the non-uniqueness of the problem is to postulate a priori information for the

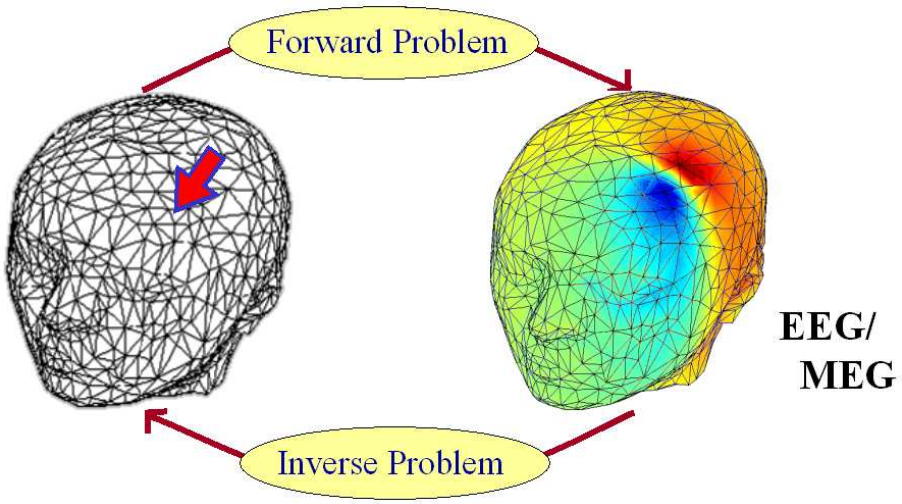

Figure 7.1: The forward and inverse problems of EMSI. The forward problem computes fields from the sources. The inverse problem locates sources from the measurements.

underlying sources. Use of more appropriate a priori information results in more reliable solutions. Over the past two decades, depending on mathematical, biophysical, statistical, anatomical and functional limits, various a priori models have been applied.

For a successful source localization the following considerations must be accounted: 1) a reliable a priori information, 2) the position and number of sensors, 3) choice of the reference electrode in EEG source localization, 4) numerical head model, 5) choice of the appropriate instant or period from the EEG/MEG data, 6) registration of MRI data and EEG/MEG data and 7) choice of the inverse problem algorithm.

Choice of the number of electrodes is investigated in [68], [141]. Michel *et al* showed that localization precision of epileptic sources drastically increased from 31 to 63 electrodes and also, though less drastically, from 63 to 123 electrodes, using a spherical three layer model [68]. However, in their study they assumed a single dipole and concluded that distributed inverse solutions would benefit from a larger number of electrodes. This thesis also investigates the effect of the number of sensors on EEG and MEG, on source localization for 64, 128 and 256 electrodes. While the accuracy improves with the increased number of sensors, no large improvements have been observed when going from

128 to 256 sensors, especially for MEG.

The choice of the reference electrode is another important consideration in EEG source localization. Gençer *et al* determined that the spatial sensitivity of the measurement system is improved for sources close to the reference electrode [141]. Thus, for cortical areas away from the reference the noise in the measurements increases, reducing the spatial resolution in these areas [141]. Consequently, the common assumption that the solution of the inverse problem is independent of the reference turns out to be incorrect [142].

The literature on source localization is diverse and rich. The suggested methods range from genetic algorithms to artificial neural networks. For comprehensive reviews on EEG/MEG source localization the following references may be suggested: [14], [67], [68], [143], [73], [144], [145], [146], [147], [148]. The inverse problem methods are usually investigated under two main categories: the parametric methods and the imaging methods [14]. These two methods will be introduced next.

7.2.1 Parametric methods

The parametric methods search for the parameters (location, orientation and magnitude) of a number of equivalent current dipoles to model the underlying source distribution. These methods are also called as dipolar (overdetermined) models [68]. The basic a priori assumption is that the surface measurements can be modelled with a small number of current sources in the brain. To guarantee a unique solution, the number of unknown parameters should be less than or equal to the number of sensors. The parametric approaches use non-linear optimization techniques for determining the unknown dipole parameters by minimizing the difference between the computed and the measured data in a least squares sense. A general risk of these methods is that they can get stuck on undesirable local minima. When searching for the dipole parameters, it is possible to separate nonlinear (location and orientation) and linear (magnitude) parameters, reducing the search space considerably [149]. Different optimization algorithms have been used for this search. Global opti-

mization algorithms such as simulated annealing or genetic algorithms search the whole parameter space [137] [150]. Nelder-Mead downhill simplex search is also widely used for source localization [151] [152] [153]. Descent based algorithms such as the Levenberg-Marquardt algorithm use the gradient information to converge quickly to a minimum [154]. However as the number of parameters increase, the risk of converging to a local minimum increases. The effect of this problem can be reduced by stochastic or multistart search strategies [155]. Other approaches include neural network based systems which were used successfully for locating dipole parameters from EEG data [150].

The main problem with the parametric approach is the estimation of the number of dipoles. Several researchers investigated how important to use a priori knowledge about the number and possible location of the dipoles in simulation and experimental studies [156], [157], [158]. Usually, the localization process is restarted with different number of dipoles and the most physiologically appropriate solution is selected. The number of independent sources can also be estimated from the statistical analysis of the measured data. Beamforming based methods such as MUSIC, and RAP-MUSIC [159] [149] [160] [161] and statistical methods such as the independent component analysis (ICA) [162] [163] can be used to identify signals coming from independent sources, and make it possible to search for these sources one by one by separating these signals. This considerably reduces the complexity of the search.

7.2.2 Imaging methods

Imaging based approaches, on the other hand, assume a large number of dipoles (typically tens of thousands) with fixed location inside the head. The brain electrical activity is reconstructed in each point of a 3D grid of solution points. The sources are usually placed according to physiological constraints on the cortex, and oriented normal to the surface of the cortex. Imaging methods are also called as distributed (underdetermined) source models [68]. These methods do not need a priori knowledge of the number of dipoles. Physiologi-

cally, the pyramidal cells, which are assumed to be the sources of the electrical activities, are normal to the cortical surface. This imposes currents to flow parallel to the surface normal of the cortex. Since the potentials and magnetic fields are linear with respect to the dipole magnitude, the resulting problem of finding dipole magnitudes is linear. However, since the number of sensors is much smaller than the number of dipoles, the problem is underdetermined, and must be constrained in some other way. The task is to find a unique configuration of activity at these solution points. However, an infinite number of distributions can lead to exactly the same field distribution at the sensors. To obtain a unique solution a priori assumptions have to be applied. These a priori assumptions can be mathematical, physiological or can be a functional information that is obtained from other imaging modalities. The reliability of the a priori model determines the accuracy of the solutions. To reduce the effect of the noise in the measurements regularization methods are applied. Many approaches for regularization have been investigated including expectation maximization, Bayesian approaches, Tikhonov regularization and Wiener filtering [164]. Algorithms for obtaining focused source images have also been proposed [165]. A summary of the imaging methods for ESI is given below based on the study of Michel *et al* [68].

The minimum norm (MN) solution assumes that the overall intensity of the current distribution should be minimum (L2-norm) [143]. It is applied in the absence of any a priori assumption. However, the restriction of having minimum intensity for the source distribution is not physiologically valid. With a MN solution, weak and localized activations are preferred instead of the strong activation of a large number of points.

The weighted Minimum Norm (WMN) algorithm is proposed to compensate for the tendency of the MN solution to favor weak and localized sources. Different weighting strategies have been proposed. The simplest one is based on the norm of the columns of the lead field matrix [166]. In the FOCUSS (Focal Underdetermined System Solution) the weight is estimated according to the solutions of the previous step and changed iteratively [165].

In Laplacian Weighted Minimum Norm (LORETA), the solution with a smooth spatial distribution is selected by minimizing the Laplacian of the weighted sources [167]. However, smooth spatial distribution can be defined in different ways for the vectors and this can yield different solutions. The physiological reasoning of this constraint is that activity in neurons in neighboring patches of cortex is correlated. However, functionally distinct areas can be anatomically very close.

The local autoregressive average (LAURA) method assumes that the activity will fall off with the inverse of the squared distance for the potential fields when you move away from the source [168].

EPIFOCUS has been developed for the analysis of focal epileptic activity [168]. In this method a single, dominant source with a spatial extent can be assumed. Because of its simplicity it is well suited for realistic head models. It does not require a certain time period of EEG/MEG for the analysis, and can be applied to instantaneous data. EPIFOCUS has demonstrated a remarkable robustness against noise [168].

Beamformer methods are designed as a spatial filter to discriminate between the signals of the data that arrive from a region of interest and those originating from other points. They can estimate source changes over time for any arbitrary voxel [169]. The beamformer approaches try minimize the interference from other simultaneously active sources to estimate the activity at a specific site of the brain. However, they have the same basic limitations as the other linear inverse solutions.

The Bayesian approaches estimate the sources by integrating a priori information into the model using statistical methods. Linear and non-linear estimators can be used. The non-linear Bayesian approaches that use functional and/or anatomical a priori information has been shown to be very successful [68].

7.2.3 Choice of the inverse method

Considering the large number of inverse problem approaches described above, the main problem is choosing a suitable source localization algorithm. Ideally, an inverse problem solution must reflect the electrical activity inside the brain accurately. Unfortunately, it is very difficult to actually know the true location of the sources inside head. Thus, there is no established gold standard method to determine the accuracy of a given inverse problem algorithm. While other functional imaging methods, such as fMRI, also provide information about the brain functions, they can not be used to asses the performance of EEG and MEG inverse problems since the relationship between the electrical and haemodynamic responses are not known.

The most widely used approach for evaluating the accuracy of inverse solutions is to simulate the measurements by choosing a dipole and solving the forward problem. Then the inverse problem is solved with the simulated data, and a *localization error* is computed. By using this approach, several researchers examined the localization performance in different regions of the brain. It has been found that the basal sources experience larger errors compared with more superior locations [112] [170]. Also the dependency of equivalent dipoles on the source depth [171], noise level [172], [173], number of recording electrodes [171], and on the head model [112] [174] has been investigated.

When choosing an inverse problem algorithm the intended application or experiment is also important. The interpretation of the results is affected by the algorithm. In case of highly focal activation, such as somatosensory simulations [133], or epileptic brain activity [175], dipole methods result in quite precise and accurate results. On the other hand, when studying more complex activities where large regions of the brain are involved, imaging methods may be more appropriate. The imaging approach lacks the precision of a multiple dipole fit, but avoids the potentially overrestrictive nature of the dipole model. The precision of the imaging solutions can be improved using more a priori information. However, this increased precision reflects increased accuracy only so far as the prior reflects the true complexity of brain activation [68].

7.3 Auditory experiments

The auditory system has been an active research area. The response to auditory stimuli has been investigated in relation to learning, and various psycholgical disorders such as autism and schizophrenia. Furthermore, auditory experiments are relatively easy to construct and execute.

The auditory system provides information about the development and structure of the brain. Furthermore, auditory experiments are relatively easy to conduct, even on infants, and for patients that are unable to respond to other stimuli. The research on auditory system includes perception of sound including binaural hearing and cognition [176], [177], maturation of the auditory systems [178], [179], detection and identification of neurological and hearing disorders in the newborns and infants [180] and hearing loss [181].

Auditory evoked potentials (AEPs) are a subclass of evoked response potentials where the "event" is a sound. The recorded AEPs originate from structures within the brain, mainly the auditory cortex, the auditory brainstem structures, and the auditory VIIIth cranial nerve. AEPs are weak signals (Cortical AEPs are 2–10 μV; signals arising from deeper brainstem structures are less than 1 μV). Depending on the latency of the response, the AEP's are usually investigated in five categories [182]:

The Auditory Brainstem Response (ABR) 1.5–15 ms post stimulus: This response originates in the 8th cranial nerve (VIII) and brainstem auditory structures.

The Middle Latency Response (MLR), 25–50 ms post stimulus: This response includes the Na and Pa waves. Na wave is the negative wave following ABR. It originates from the upper brainstem and/or auditory cortex. Pa is the positive wave at about 30 ms, originating bilaterally in the auditory cortex.

The "Slow" cortical auditory ERPs: These include the P1-N1-P2 sequence (50–200 ms poststimulus; originating in auditory cortex). N1 is the large

negative wave that occurs about 80-100 ms after the stimulus. It originates primarily in the auditory cortex bilaterally.

The "Late" cortical auditory ERPs: This response mainly consists of the Mismatch Negativity (MMN) beginning around the time of N1 and later. The MMN is a response of the brain reflecting a change in the stimulus. Other "late" ERPs include N2b and P3, however, these cortical ERPs are not from auditory structures.

Auditory Steady-State Responses (ASSR): These are the responses to stimuli presented at rates when the brain response to one stimulus is overlapped with responses to other stimuli. Responses to slower modulation rates (less than 20 Hz) appear to originate largely from cortical structures; responses to faster rates (70 Hz and higher) appear to reflect brainstem processes.

Huotilainena *et al* 1998 compared EEG and MEG using these three responses to standard, deviant and novel sounds. The sources are localized from measurements from 122 MEG coils [183]. It was determined that a considerable part of the EEG signal can be explained by the localized sources. It was also concluded that source-current components not detectable by MEG also contribute to the EEG signal. In a recent study, the neuromagnetic analysis of auditory evoked fields in frequency and time domains suggest that the phases of several oscillators within the cortex are locked at around the timings of N100m, but fluctuated randomly at the other timings [184].

The replicability of EEG and MEG source localization for evoked N1 (EEG) and N1m (MEG) signals have also been investigated [185]. It has been determined that the standard deviation (SD) of the source coordinates was about 2mm for contralateral N1m, and 4mm for N1 and ipsilateral N1m. The SD of the computed amplitudes and latencies are almost equal for EEG and MEG. The researchers concluded that EEG and MEG can be used for investigating the simultaneous activity of the left and right auditory cortex, and determined that MEG is superior in certain experimental setups.

Different inverse problem approaches have been applied to the auditory experiments, such as dipole models [178] and LORETA, which is an imaging based method [186]. Recently, several researchers have been investigating psychological disorders such as autism [187] and schizophrenia [188] in relation to the auditory system. Teder *et al* determined that there is a fundamental deficit in the spatial focusing of auditory attention in autism, and concluded that this be a factor that impedes social interactions and sensory-guided behavior, particularly in noisy environments [187].

Ducommun *et al* investigated the processing of the cortical networks related to the motion of the sound [189]. In particular whether the same pathways are involved when identifying the location and the motion of a sound source. They have analyzed 1000 ms duration of recorded AEP's, generated through bursts of white noise with different location and motion characteristics. The sources are localized using the LAURA algorithm. The study concluded that there is a partly segregated network within the auditory cortex for processing location and motion of sound.

It has been determined that sounds with temporal pitch produces activation in the anterolateral Heschl's gyrus [11]. Gutschalk *et al* investigated this activity using MEG [190]. By alternating regular and irregular click trains without interruption which is called a "continuous stimulation" paradigm, the authors isolated the cortical response specific to the pitch from the intensity related response. It was observed that the onset of the pitch was accompanied by a transient field and a strong sustained field. Both of these fields were associated with sources in the lateral Heschl's gyrus. Due to the high latency in the examined pitch response, it was concluded that the processing occurs in a subcortical structure, and the measured cortical responses reflect subsequent processes involving the measurement of pitch values and changes in pitch.

7.4 Genetic Algorithms

Genetic algorithms are iterative optimization techniques inspired by the biological mechanisms of genetics and natural selection. GA starts with a randomly

selected population of potential solutions. These individual solutions, called chromosomes, are used for creating new generations through operations such as selection, crossover and mutation. While the initial population is randomly selected, subsequent generations evolve towards better solutions by selecting and combining parts of better fitting chromosomes.

Several researchers have previously applied GA to EMSI source localization. Uutela *et al* studied global optimization methods that find the minimum of the least-squares error function of the current dipoles using simulated magnetic fields [137]. They used a single layer BEM model with 864 triangles and 2-4 dipole models. They investigated clustering method, simulated annealing, and genetic algorithms. They observed that the genetic algorithms were the most effective method in terms of accuracy. McNay *et al* used a genetic algorithm search for the localization of 2 dipole sources from simulated potentials with SNRs of 2, 5, and 10 [136]. They used a spatio-temporal model in which the error function is described by the sum of the squared errors between the measured and modeled fields over the time points of interest. They used a homogeneous sphere with a radius of 10 cm with 64 electrodes for the simulation studies. The localization accuracy ranged from 0.01 to 0.07 cm with an SNR of 10; 0.02 to 0.26 cm with an SNR of 5; and from 0.06 to 0.73 cm with an SNR of 2. Li *et al* suggested to use a gradient-based algorithm after finding a rough estimate of the current dipoles with genetic algorithm to speed up global optimization algorithm [138]. A spherical head model is used for the rough estimation. This rough estimate is then used as a starting point for a fine search using a gradient-based algorithm, in which a BEM solution for a realistic-shaped brain model with 2588 triangles. They searched for 2 dipoles using simulated magnetic fields. They claim this hybrid algorithm increased convergence rate 3-4 times [138]. Nagano *et al* used genetic algorithm for source localization using simulated MEG data [139]. They used 2 current dipoles in each hemisphere of the brain as a source model, and observed an accuracy within 1 cm when the SNR was 20. Ungan *et al* applied GA followed by a simplex algorithm for ESI. They used experimental 124 channel EEG data

obtained by applying auditory stimulus and performed source localization at N1 latency. They used a four layer spherical head model and estimated one dipole in each hemisphere of the brain.

In this work, the performance and characteristics of GAs are investigated in EMSI. In addition to the basic GA, some improvements such as micro-GA (μGA) real-μGA and intergenetation projection are also implemented and tested [191], [1]. The next section describes the properties of GAs and the improvements used in this work. The GA implementations are first evaluated using a simple test function.

7.4.1 Basic Concept of GAs

Consider the following optimization problem to present the basic concept of the Genetic Algorithms:

$$Maximize\ f(\mathbf{x}) \tag{7.1}$$

$$subject\ to\ \mathbf{x}^L \leq \mathbf{x} \leq \mathbf{x}^U \tag{7.2}$$

where $\mathbf{x}$ is the vector of parameters, the superscripts L and U represent the lower and upper bands of the parameters respectively. In GA each parameter, $\mathbf{x}_i (i = 1, 2, \ldots, N)$, of a given problem should be coded into a finite-length string. There are several coding methods, among which binary coding is the simplest and most popular. A GA program starts with a population of chromosomes (individuals) that is selected randomly from the entire search space. Each of the chromosome's fitness values are evaluated by computing the objective function $f(\mathbf{x})$. Simulated genetic operators are applied to simulate the evolution process, which leads to the most fit chromosome that is the solution to the optimization problem.

7.4.2 Genetic operators

Three basic genetic operators – selection, crossover, and mutation – are performed in that order on these chromosomes of the current generation to produce child generations that better fit the simulated evolution process. These

three basic operations are described below:

7.4.2.1 Selection

The selection operation is an artificial emulation of the *natural selection* process of the Darwin's survival theory [192]. During the selection process, a group of chromosomes from the current generation is chosen for reproduction. This selection is based on the fitness values of the chromosomes and aims to improve the average quality of the population. Due to the selection process, the individuals of higher fitness will have a higher probability of being copied to produce new individuals of the next generation. Since the selection depends on the fitness value of the individuals, the selection process focuses on the more promising regions of the search space.

7.4.2.2 Crossover

Once the chromosomes are selected, new chromosomes of the child generation are formed using the crossover operation. Crossover is the most important operation in GA. It exchanges part of the genes in the chromosomes of two selected parents to create new individuals for the child generation. Individuals are picked in pairs from the selected chromosomes to become "parents". With a certain crossover probability, two new individuals, or "children", are created based upon the chromosomes of the parents.

7.4.2.3 Mutation

The mutation operator is designed so that one or more of the chromosome's genes will be mutated with a small probability. The goal of the mutation operator is to prevent the genetic population from converging to a local minimum and to introduce some new possible solutions to the generation. During mutation, one of the bit values of a chromosome is flipped from 1 to 0 or vice versa with a certain probability. The probability of mutation is typically chosen to be very small, on the order of 0.001-0.005. High values of the probability tend to destroy valuable information in highly fit sequences. The mutation

phase serves to maintain diversity in the population by forcing the algorithm to search in new regions of the decision space. However, mutation is only of secondary importance compared to the selection and crossover operations.

After the mutation process, the next iteration in the GA begins with a new generation of individuals copied from the previous individuals. Through the repeated application of the selection, crossover, and mutation operators, the initial population is translated into new populations in an iterative manner. Each new population will tend to contain better strings of bits and will eventually converge to an optimal population.

7.4.3 Comparison of GA with other algorithms

Genetic algorithms differ from other optimization techniques in several respects:

- The GA operates on a population of potential solutions rather than a single solution candidate.

- The genetic operators that guide the population of potential solutions introduce probabilistic rather than deterministic transitions. This characteristic greatly enhances the capability of the algorithm to search for global rather than local minima in the error function, regardless of the initial guesses.

- GA only uses the value of the objective function for each chromosome. No derivatives or other auxiliary information is needed, thus, it is able to handle nondifferentiable, noncontinuous problems.

- GA operations have inherent parallelism, and can easily be implemented in parallel architectures.

- Unlike other optimization procedures that operate directly on the parameters to be optimized, genetic algorithms typically operate on coded representations of these parameters [136], [1].

Table 7.1: Comparison between GA and Gradient-Based Optimization and Search Procedures [1]

Items	GA	Gradient-Based Optimization
Search bases	Groups of points	Single point
Initial guess	No	Yes
Function information	Objective function only	Objective function and its derivatives
Search rule	Probabilistic in nature	Deterministic laws
Convergence	Fast at beginning, slow at later stage	Relatively slow at initial stage, very fast at later stage
Applicability	Global search for complex problems with many local optima	Local search for simple problem with single optimum
Computing efficiency	Computationally expensive	Efficient

The main differences between GA and gradient-based optimization methods are summarized in Table 7.1.

All these features make GAs a powerful tool for solving the complex optimization problems. However, the convergence of GAs are sometimes very poor, especially when the searching has reached a local region near the global optimum [191].

7.4.4 Improvements to basic GA

To improve the convergence performance and enhance the searching capability, it has been recommended to incorporate GAs with the conventional optimization techniques [138]. As GAs are good at global searching but slow at converging, while the conventional optimization techniques are good at fine-tuning but lack a global perspective, the hybrid algorithms of incorporating GAs with the conventional optimization techniques can combine the advantages of both methods. In this study a hybrid genetic algorithm is used which is based on Levenberq-Marquard search in each iteration of the GA. After each iteration, a local optimization step is used to improve the best individual of the population. This process speeds up the convergence of the GA especially

on regions with uniform conductivity where the potential changes are continuous. As an alternative to this approach, the optimization step is implemented as a mutation operator, which optimizes a random individual, with a given probability. While this also provided some improvements, applying local optimization once in each generation with the best individual, provided better convergence characteristics.

Another consideration in using GA was the determination of the convergence criteria. In addition to an upper limit on the number of generations, several criteria, such as the diversity of the population, minimum, maximum and mean scores of individuals have been used when determining convergence. For realistic data, a manually specified target fitness is also being considered. A possible improvement would be to derive the target fitness score from the statistics of the measurements and noise.

7.5 Results

The first step after developing an inverse problem solver is to test the performance and accuracy of the algorithm, and check whether the algorithm matches the expected localization error bounds. For this purpose, first the algorithm is tested using Monte-Carlo simulations. Results from the simulated source localization experiments are presented. The source localization results using experimental EEG data is then shown.

7.5.1 Performance of GA for source localization

The accuracy of GA on source localization problems is tested using a spherical head model with Monte-Carlo simulations. A 4-layered model is used in the simulations [48]. The radii of the layers are 6.1, 6.5, 7.1, and 7.5 cm for brain, CSF, skull and scalp layers respectively. The conductivities of the layers are 0.33 S/m for brain and scalp, 0.0042 S/m for skull and 1 S/m for the CSF layer. Due to the large number of trials required by the monte-carlo simulation, the forward problem is solved analytically.

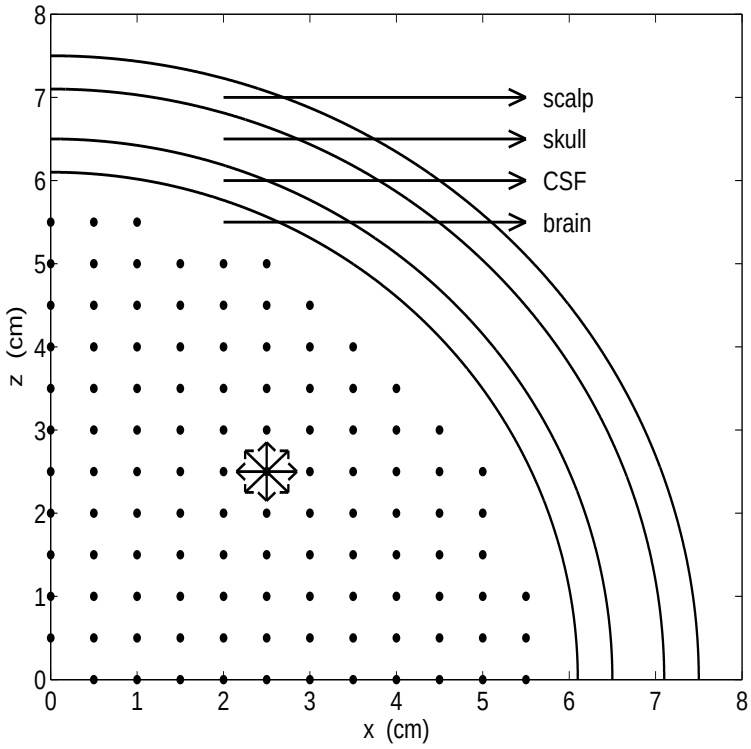

Figure 7.2: A grid of dipole locations are shown on the x-z plane for a four-layer spherical model. The dipole orientations projected onto the x-z plane are also displayed for a specific grid point.

A grid of 111 dipoles are placed on the positive x-z plane of the sphere (Figure 7.2). At each dipole location 14 different uniformly distributed dipole orientations are assumed. The SNR of the fields is taken as 10 and 5, where the SNR is defined as the ratio of the standard deviation of the signal to the standard deviation of the noise. The solutions are repeated at each point for a total of 1400 trials per location. The effect of number of sensors/electrodes is also investigated by using 64, 128 and 256 sensors. The sensor positions are illustrated in figure 7.3. Mean localization and orientation errors are computed for both potentials and magnetic fields. The localization error is plotted as a function of source position.

Localization error graphs for EEG are given in figures 7.4, 7.5 and 7.6 for 64, 128 and 256 electrodes respectively. These figures have the same basic pattern. The errors increase for deep dipoles. The localization errors are also higher near the z=0 plane. This is also expected since the sensors only cover the upper hemisphere. The results are consistent with the Monte-Carlo

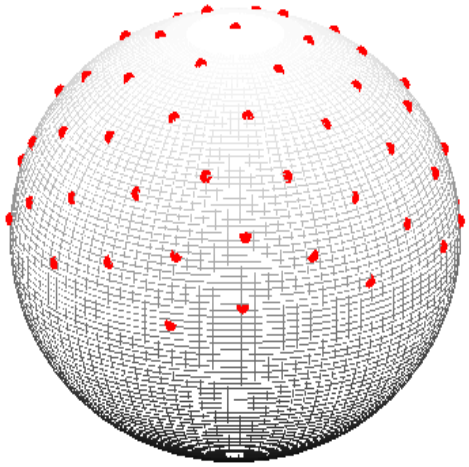

(a)

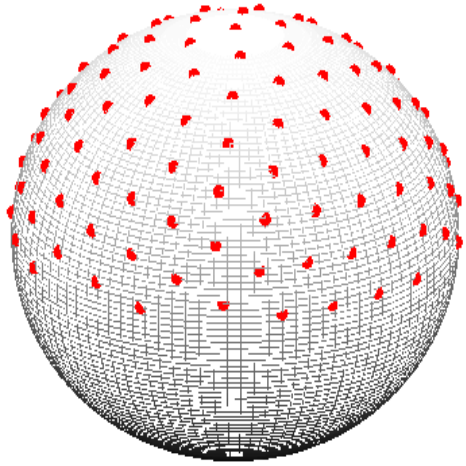

(b)

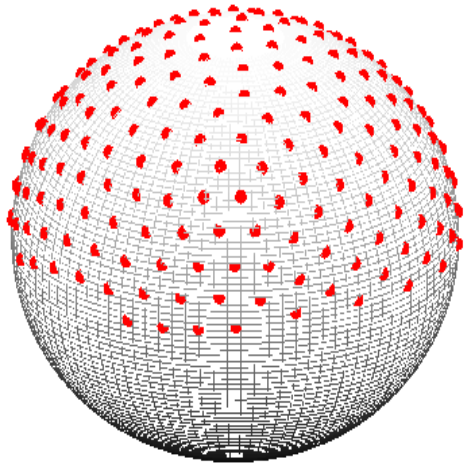

(c)

Figure 7.3: Electrode locations on the spherical surface. (a) 64 electrodes, (b) 128 electrodes, (c) 256 electrodes.

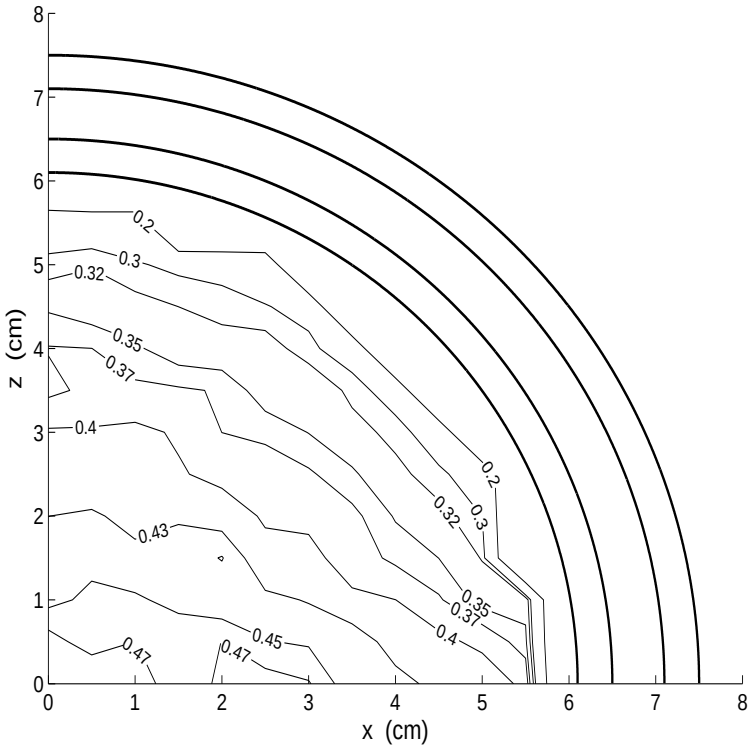

(a)

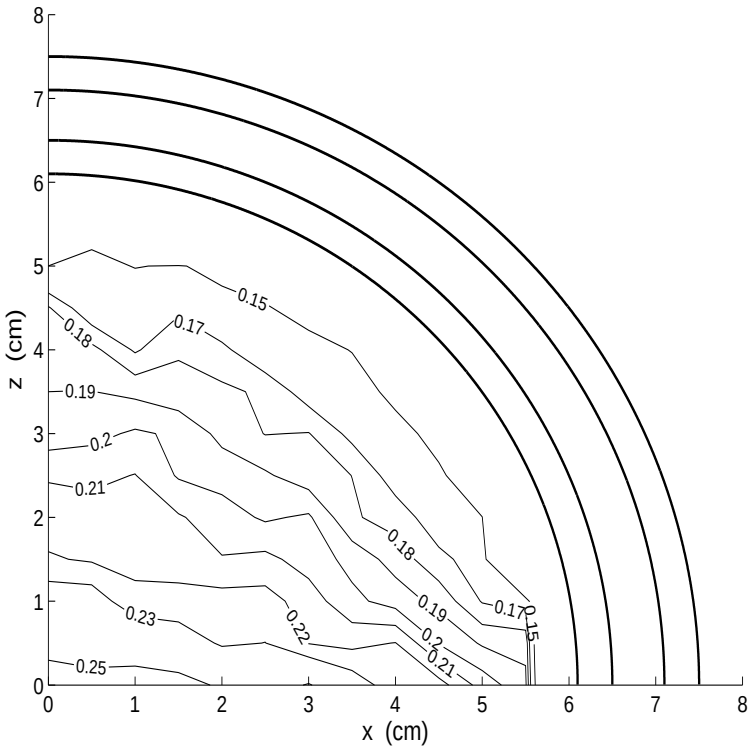

(b)

Figure 7.4: Localization errors (mm) for a grid of dipoles when there are 64 electrodes. The potential field is calculated analytically. (a) SNR=5, (b) SNR=10.

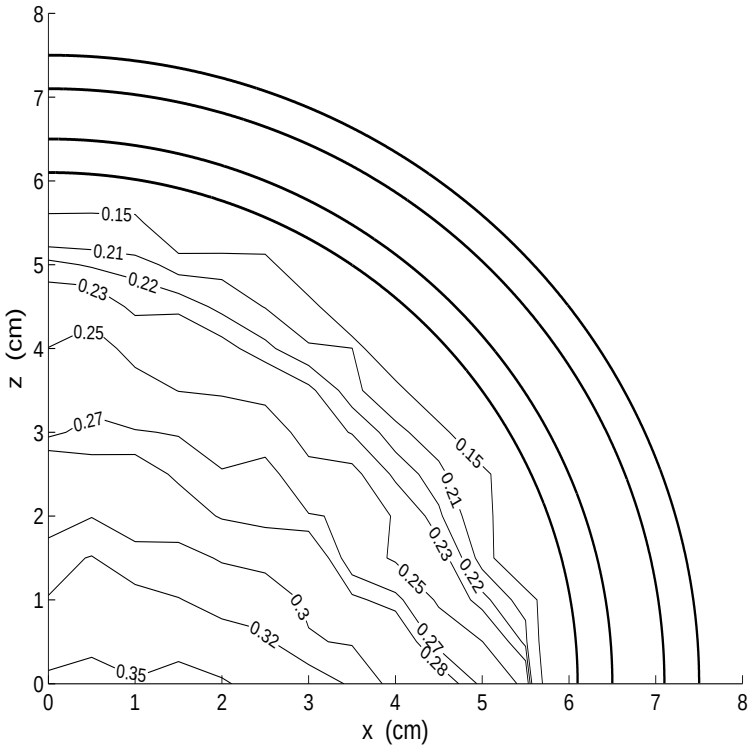

(a)

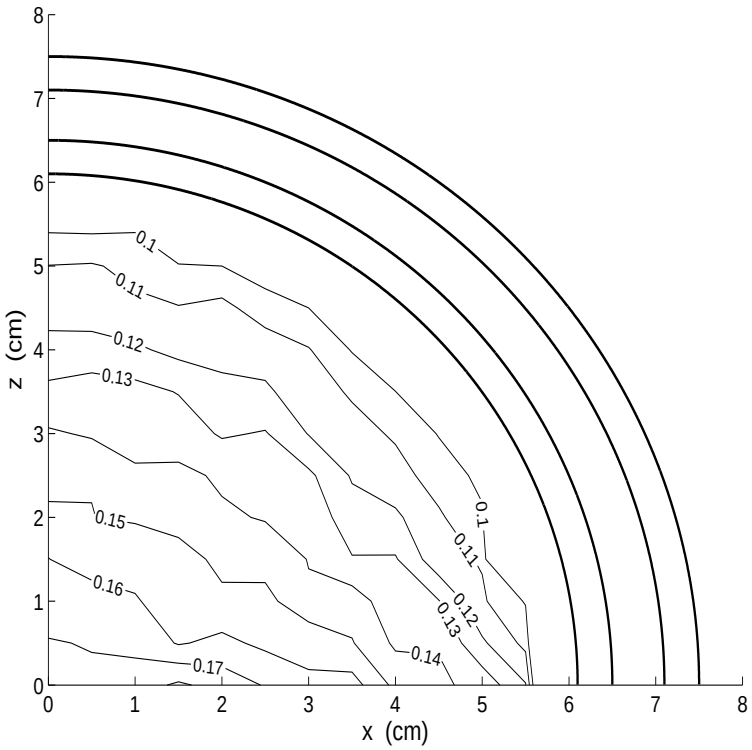

(b)

Figure 7.5: Localization errors (mm) for a grid of dipoles when there are 128 electrodes. The potential field is calculated analytically. (a) SNR=5, (b) SNR=10.

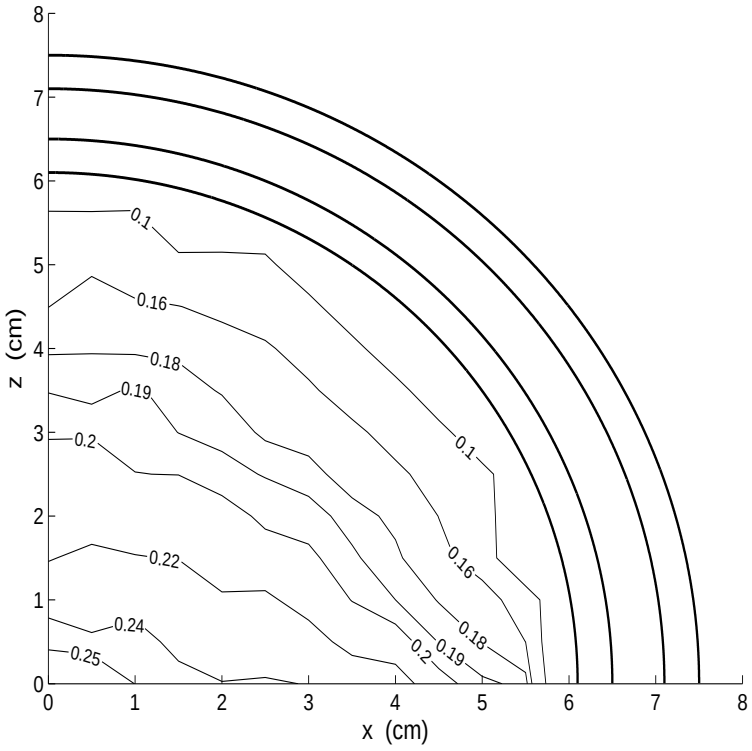

(a)

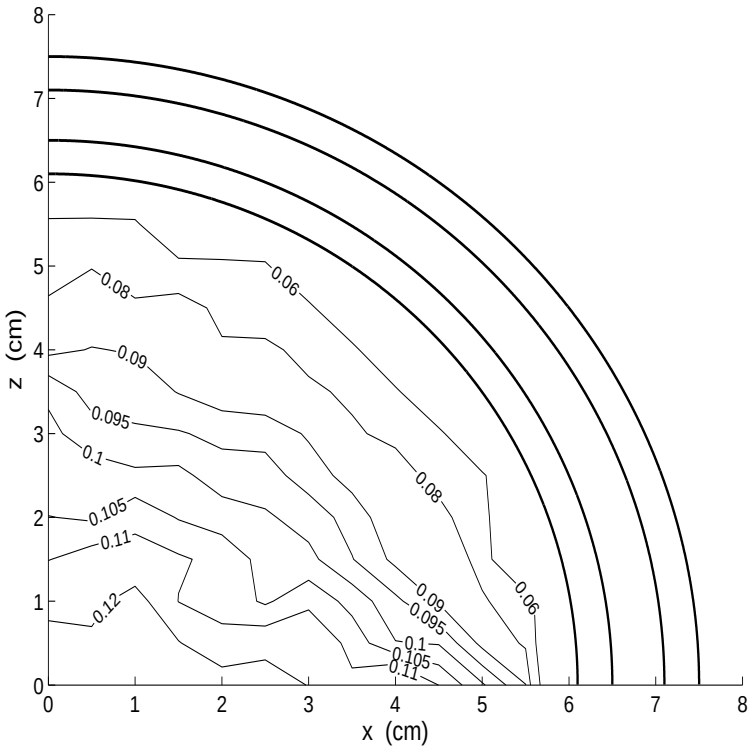

(b)

Figure 7.6: Localization errors (mm) for a grid of dipoles when there are 256 electrodes. The potential field is calculated analytically. (a) SNR=5, (b) SNR=10.

Table 7.2: Mean localization (LE, mm) and orientation errors (OE, degrees) for the dipoles placed on the grid shown in Figure 7.2. The results are obtained using the analytical solutions of the potential field.

Electrodes	SNR	LE (mm)	OE (deg.)
64	5	3.81	0.42
128	5	2.65	0.05
256	5	1.89	0.40
64	10	1.92	0.05
128	10	1.32	0.37
256	10	0.95	0.02

Simulation results presented by Mosher *et al* [193].

Table 7.2 presents mean EEG localization and orientation errors, computed using the locations in the grid (Figure 7.2). At each grid position, localization and orientation errors for 14 different dipole orientations are computed and mean values are presented. It is observed that the localization error decreases when the number of electrodes and the SNR increases. The orientation error is always less than 1 degrees, and the average localization error decreases from 3.81 mm to 1.89 mm (SNR=5) and 1.92 mm to 0.95 mm (SNR=10) when the number of electrodes increases from 64 to 256.

To validate the numerical solutions, the Monte-Carlo simulations are repeated using a spherical BEM mesh. The mesh has 2048 quadratic elements and 4104 nodes. Each of the four shells contain 512 elements and 1026 nodes. The radii and the conductivities of the BEM model match the geometry used in the analytical simulations. Figure 7.7 shows the localization error bounds assuming 64 electrodes and an SNR value of 10. Simulations using numerical and analytical forward solutions exhibit the same localization error characteristics.

The Monte Carlo simulations are also repeated for MEG source localization. Localization error graphs for the three sensor sets (64, 128, and 256 sensors) are given in Figures 7.8, 7.9 and 7.10, respectively. The errors increase for deep dipoles. The localization errors are also higher near the z=0 plane. This is also expected since the sensors only cover the upper hemisphere. There is also high localization error along the z-axis, near the origin. The reason for

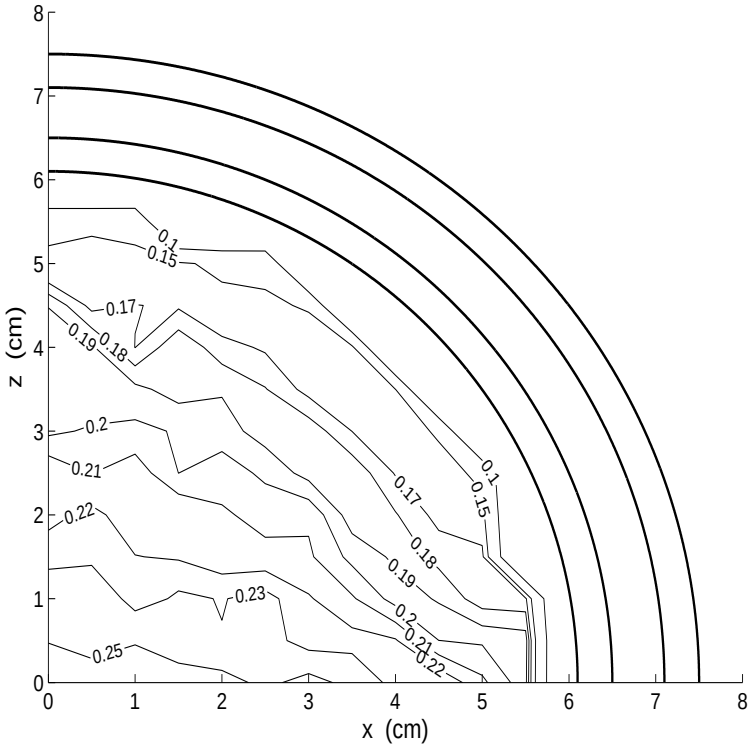

Figure 7.7: Localization errors for a grid of dipoles when there are 64 electrodes. The forward problem solutions for the potential field are obtained numerically. SNR=10.

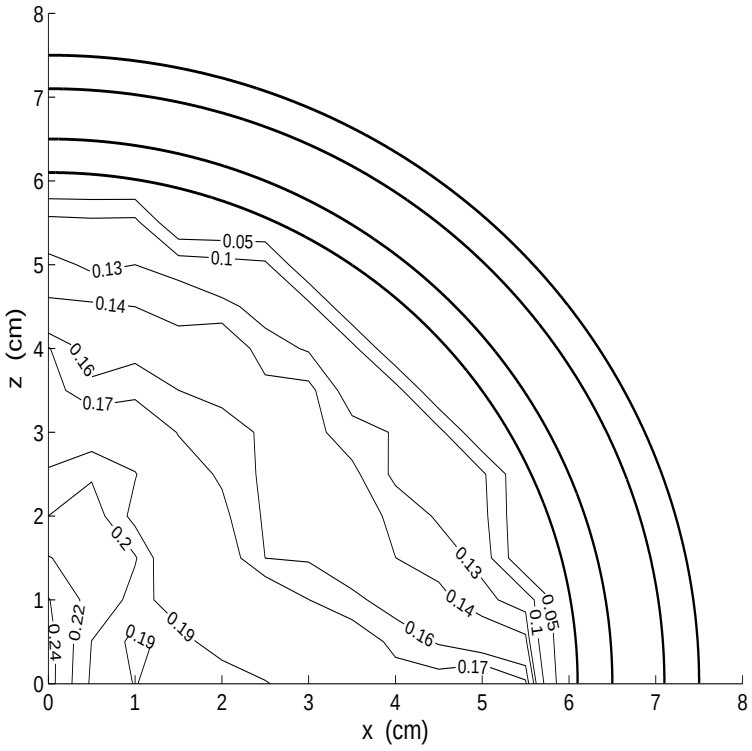

(a)

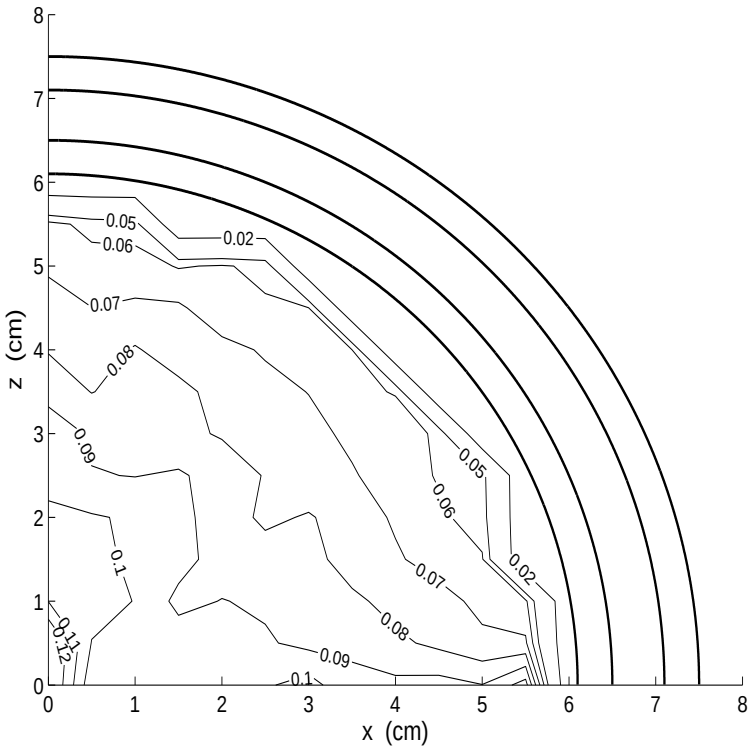

(b)

Figure 7.8: Localization errors (mm) for a grid of dipoles when there are 64 sensors. The magnetic field is calculated analytically. (a) SNR=5, (b) SNR=10.

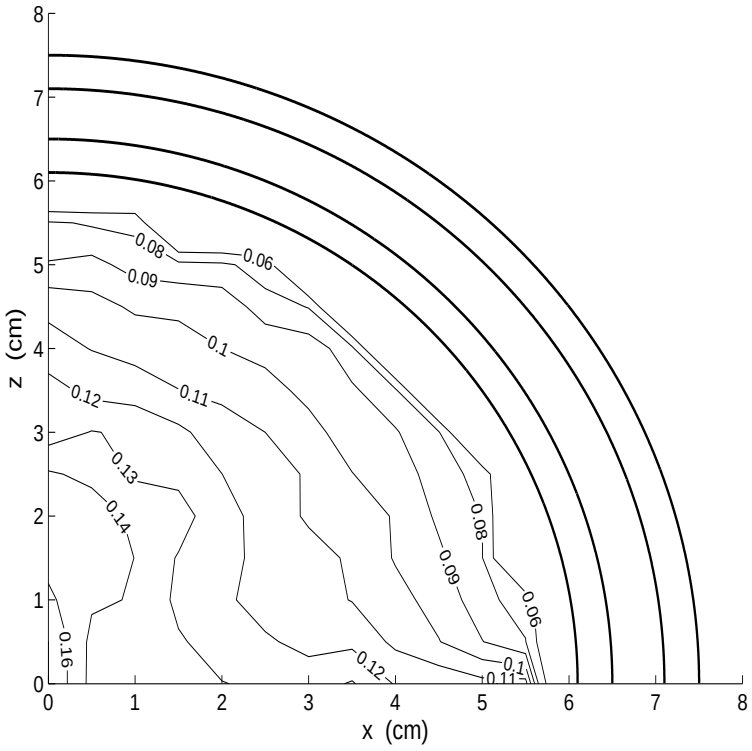

(a)

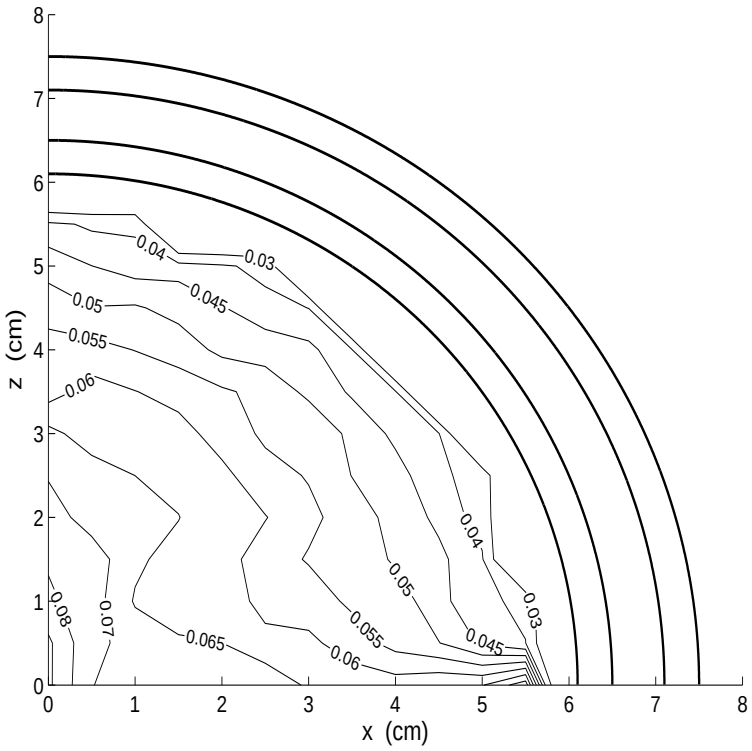

(b)

Figure 7.9: Localization errors (mm) for a grid of dipoles when there are 128 sensors. The magnetic field is calculated analytically. (a) SNR=5, (b) SNR=10.

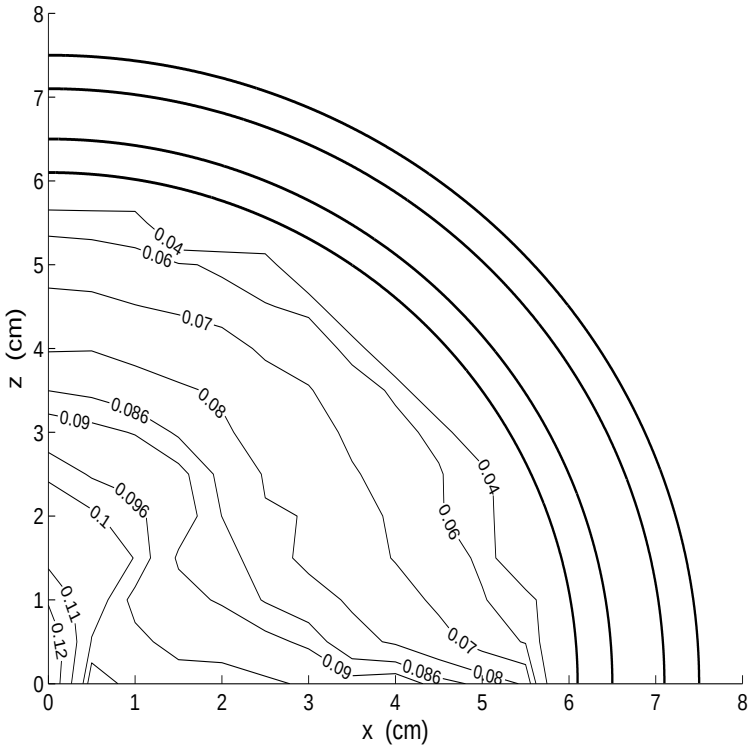

(a)

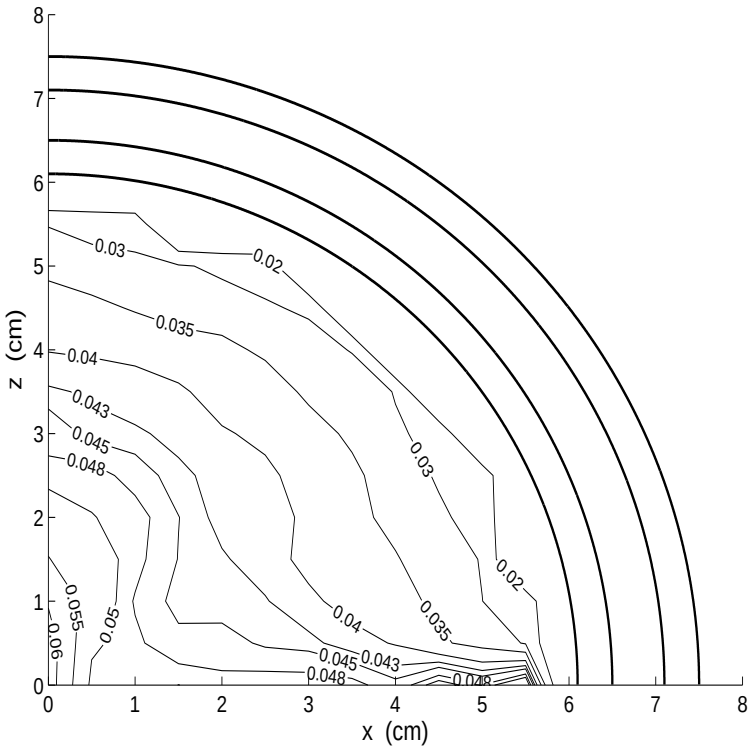

(b)

Figure 7.10: Localization errors (mm) for a grid of dipoles when there are 256 sensors. The magnetic field is calculated analytically. (a) SNR=5, (b) SNR=10.

Table 7.3: Mean localization (LE, mm) and orientation errors (OE, degrees) for dipoles placed on the grid shown in Figure 7.2. The results are obtained using the analytical solutions of the magnetic field.

Sensors	SNR	LE (mm)	OE (deg.)
64	5	1.60	0.60
128	5	1.10	0.25
256	5	0.79	0.01
64	10	0.80	0.22
128	10	0.56	0.04
256	10	0.34	0.11

this error is due to the fact that the radial dipoles have zero magnetic field in spherically symmetric geometries, since the dipoles near the origin are almost radial, the field values, thus the effective SNR is lower, and errors increase in these regions.

Table 7.3 presents mean localization and orientation errors for the MSI simulations. At each grid position, the localization and orientation errors for 14 different dipole orientations are computed and mean values are presented. It is observed that the localization error decreases when the number of sensors and the SNR increases. The orientation error is always less than 0.6 degrees, and the average localization error decreases from 1.6 mm (SNR=5, 64 sensors) to 0.34 mm (SNR=10, 256 sensors).

7.5.2 Simulation studies with realistic head models

In this section, the effects of the eye tissues, and the CSF on the IP solutions are explored. For this purpose, three different realistic BEM head models are generated having different number of tissues. The first mesh is taken as the reference model representing five types of tissues: scalp (0.33 S/m), skull (0.0042 S/m), CSF (1 S/m), brain (0.33 S/m) and eyes (0.5 S/m). In the second mesh, the eyes are removed, and in the third mesh the CSF and eyes are removed from the reference model. These models are shown in Figure 7.11.

The first model contains 9906 nodes and 4984 elements. Model 2 with the eyes removed has 9330 nodes and 4662 elements. Further removing the CSF

layer results in Model 3 with 7412 nodes and 3704 elements.

9 dipoles are located in the brain (Figure 7.12) and the inverse problem solutions are performed for horizontal and vertical dipole orientations. The electrode positions are the digitizer points, obtained using a Polhemus Fastrak digitizer, as explained in the previous chapter. The location of the magnetic sensors are computed such that the sensors are 5 mm above the electrodes, along the direction of the surface normal. The potential and magnetic fields are calculated using the reference model and the inverse problem is solved assuming an SNR value of 10.

To test the effect of the head model, a three layer spherical model is generated. For the spherical model, the center and radius for a best-fitting sphere should be computed. For that purpose, a set of points is selected from the scalp surface that covers the top and back of the head. The radius and the center of the sphere are calculated that minimizes the distance between the selected points and the sphere. Figure 7.13 shows the selected points on the scalp surface used in the calculation of the radius and the center of the sphere. Figure 7.14 presents the scalp surface and the best fit sphere. The inner radii of the sphere are calculated using the ratio of the concentric spheres model as described in [48].

The simulation results for EEG and MEG localization with different head models is shown in Table 7.4. For the first model, the average localization error is computed as 1.1 mm for EEG and 1.2 mm for MEG. Model 2 removes the eyes from the first model and the errors increase to 3.15 mm for EEG and 1.4 mm for MEG. With Model 3, removing the CSF layer, the localization errors become 6.07 mm and 3.95 mm for EEG and MEG respectively. It is observed that, for the inverse problem solutions using the EEG measurements the effect of the eye conductivity is more important than for the inverse problem solutions using the MEG measurements. Modeling the CSF affects the IP solutions using both EEG and MEG measurements. However, the localization error is greater when the solutions are obtained using the EEG measurements. When the spherical model is used for source localization, the errors increase to

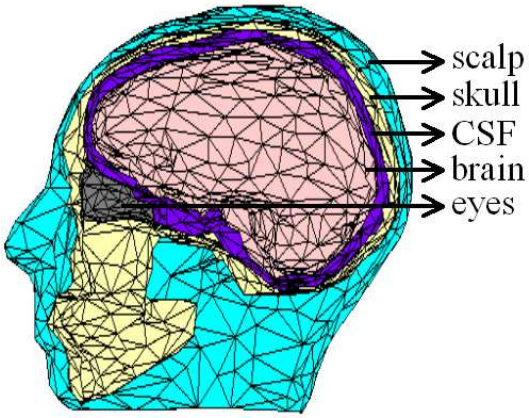

(a)

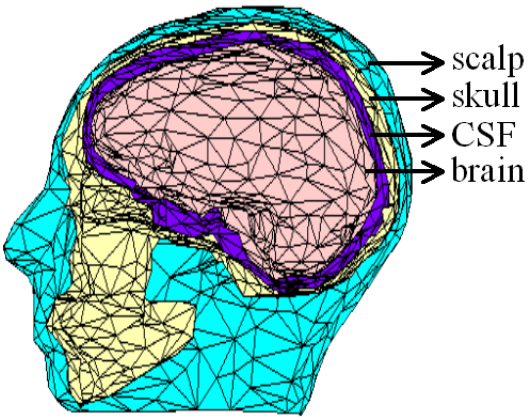

(b)

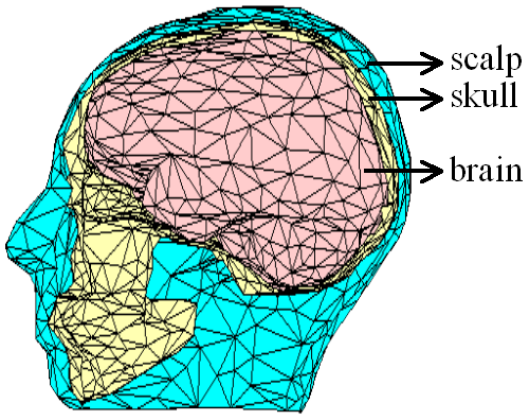

(c)

Figure 7.11: Realistic models. (a) Model 1, the reference model, (b) Model 2, the eyes are removed from the reference model (the eye conductivities are assumed to be equal to the skull conductivity), (c) Model 3, the eyes and the CSF are removed from the reference model (CSF conductivity is assumed to be equal to the brain conductivity).

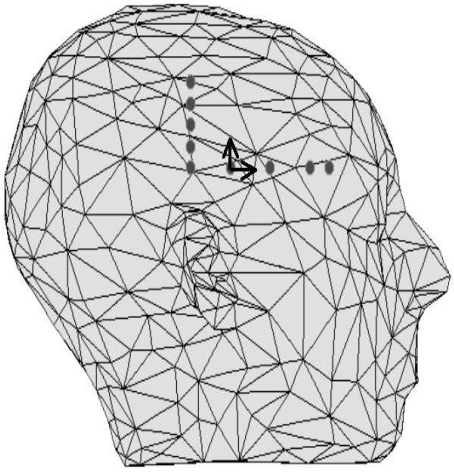

Figure 7.12: Position of the dipoles used in realistic head simulations. The inverse problem solutions are done for two directions: horizontal, towards the face, and vertical, towards the top.

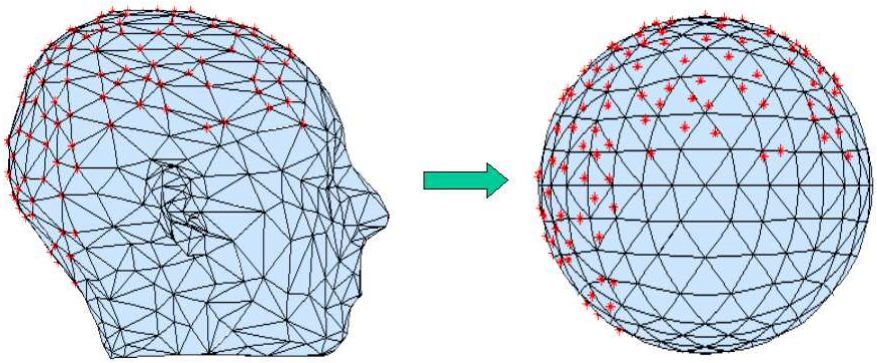

Figure 7.13: Selection of the scalp points to find the best-fit sphere.

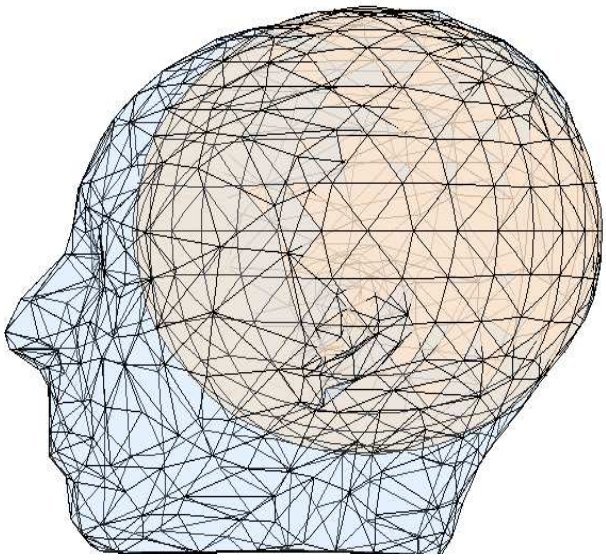

Figure 7.14: The scalp surface and the best fit sphere.

Table 7.4: Mean EEG and MEG localization errors (mm) for the dipole setup shown in Figure 7.12. The simulated data is generated from Model1 by adding sensor noise with SNR=10.

	Model 1 (Realistic)	Model 2 (Realistic)	Model 4 (Realistic)	Model 4 (Spherical)
EEG	1.1	3.15	6.07	8.48
MEG	1.2	1.4	3.95	7.0

8.48 mm for EEG, and 7.0 mm for MEG, showing the importance of realistic head modeling.

To test the accuracy in multiple dipole localization, a face-to-face dipole configuration is selected. This simulation represents a worst-case configuration when the dipoles are close to each other since the corresponding potentials cancel each other. The dipole configurations are shown in Figure 7.15. There are two face-to-face dipole groups placed symmetrically, for a total of four dipoles. The simulated data is generated using the realistic model by adding sensor noise yielding SNR of 10. The experiment is repeated for two different dipole separations, 1 cm and 4 cm. The simulation results are shown in Table 7.5.

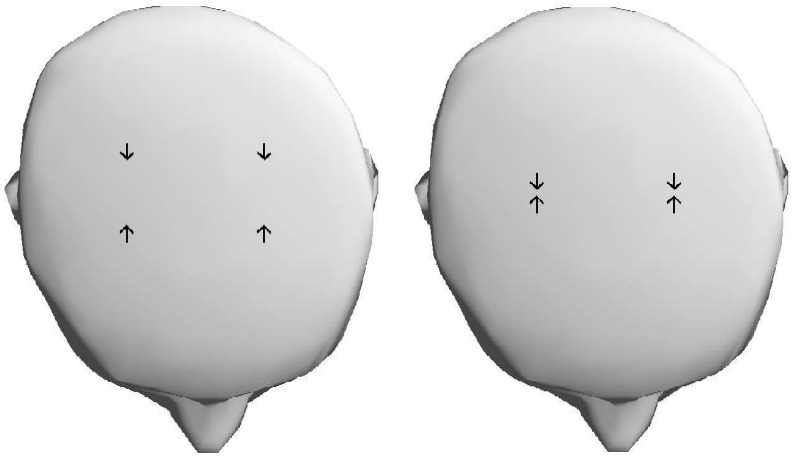

(a) (b)

Figure 7.15: Face-to-face dipole configuration for multiple dipole localization simulations. The dipole separation between the face-to-face dipoles is (a) 4 cm and (b) 1 cm.

Table 7.5: Mean and maximum EEG localization errors (mm) when dipoles are located face-to-face, with different separations (mm). The simulated data is generated from the realistic model by adding sensor noise with SNR=10.

	Dipole separation (mm)	Mean LE (mm)	Max LE (mm)
realistic	40	1.54	2.77
spherical	40	9.22	9.38
realistic	10	3.17	4.80
spherical	10	9.58	10.91

When the dipole separation is large (4 cm), the performance in localization is quite similar to a single dipole case, i.e., the mean error is 1.5 mm. As the dipoles get closer, the realistic model still provides better results, however, its performance degrades. For an extreme case, when the distance between the dipoles approaches to zero, using a realistic or a spherical model will not be important as the potentials will completely cancel each other.

7.5.3 Source localization using experimental EEG data

The adopted inverse problem solution approach, ie. the GA, is also applied to experimental (EEG) data. Auditory evoked potentials are measured and source analysis is performed for a specific time instance. The selected time

instance corresponds to the N1 component of the recorded AEP and comprises the highest peak in the measurements. The following subsections describe the details of the experiment and the results of source localization process.

7.5.3.1 Stimulation and recording

The auditory experiment setup is shown in Figure 7.16. The experiment was carried out by repeatedly applying a tone-pip of 100 ms duration and collecting stimulus locked samples (200 samples are recorded at each signal). The experiment is repeated for two signal tones, 1 kHz and 5 kHz. For the 1 kHz tone, data corresponding to 517 signal tones (trials) are collected. For the 5 kHz tone 311 trials were recorded.

The data was acquired using a 128–channel EEG system built in Hacettepe University, Faculty of Medicine, Biophysics Department. The EEG data are recorded in 800 ms with 250 samples per second sampling rate. Figure 7.17 shows the timing related to stimulus and data acquisition. The responses were measured in an electrically and acoustically shielded EEG experiment room. The common mode rejection ratio of the system is greater than 80 dB (typically 90 dB). Note that, in this specific experiment, a higher CMRR is achieved by connecting the patient directly to ground. Normally, in a clinical study, the patient must be isolated from the earth ground. The amplifiers shown in the block diagram consist of 16 cards with 8 channels. The gain of the amplifiers is 50000. Second order filters are used with 0.3 Hz–70 Hz band–pass frequency. The data acquisition is done using two 64–channel 12 bit National Instruments (NI) cards (PCI 6071E) mounted in the PC workstation. The stimulus is generated using another 16 bit NI card (PCI 6711) having an analog output.

256 channel Neuroscan electrode cap is used in the experiment and 128 of the channels are selected uniformly. The position of the electrodes are shown in Figure 7.18.

Figure 7.19 (a) shows the subject (me, the author of this thesis) with 128 electrodes attached on the head surface and Figure 7.19 (b) shows Süha Yağcıoğlu and Nevzat Gençer while injecting gel into each of these electrodes.

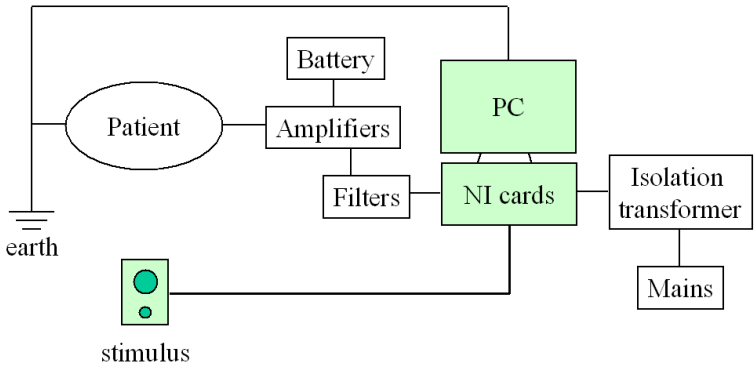

Figure 7.16: Block-diagram of the EEG system in the Biophysics Department of the Hacettepe University.

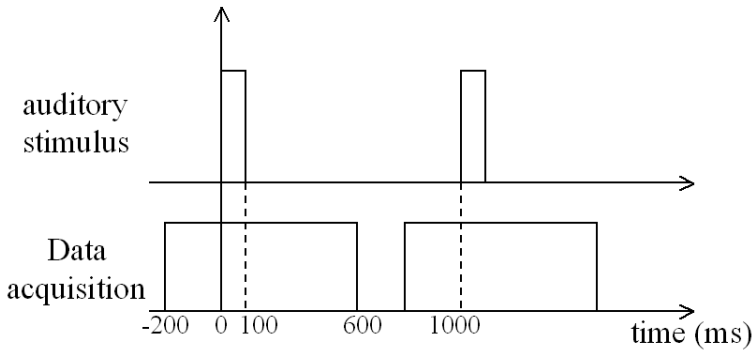

Figure 7.17: Timing related to stimuli and data acquisition during the AEP experiment.

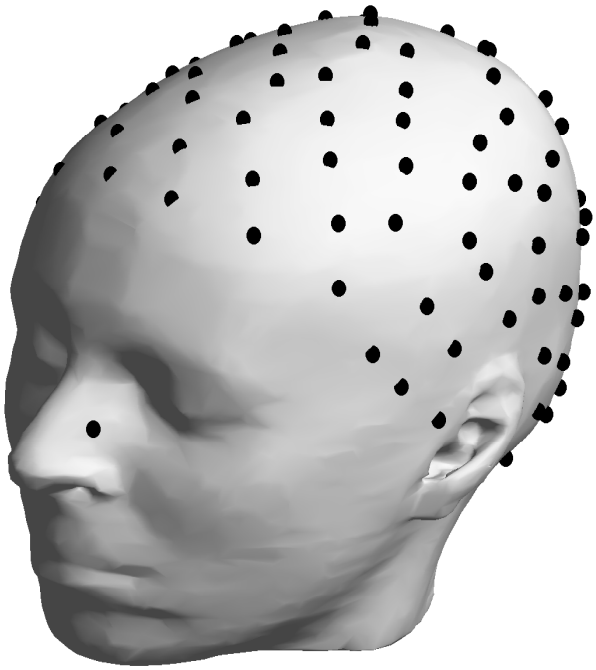

Figure 7.18: Position of the selected electrodes on the scalp surface, after applying the segmentation (Chapter 4) and registration (Chapter 6) processes.

7.5.3.2 Data processing

For rejection of the eye artifacts the signals having a value higher than 30 μV and lower than -30 μV are omitted. The rest of the signals are averaged and filtered using a 30 Hz low-pass filter. To remove the line noise, 50 Hz and 100 Hz band-stop filters are applied. For source localization, we have used the first peak located at 100 ms. This peak is determined using the global field power (GFP) of the data [194], where for each instance the variance of the potentials at the channels is calculated. The collected EEG data is presented in Figure 7.20 before and after filtering for 1 kHz stimulus. Figure 7.21 and Figure 7.22 shows the contour plots of the EEG data when the stimulus is 1 kHz and 5 kHz, respectively.

7.5.3.3 EEG dipole source analysis

In the auditory experiments, a symmetric two-dipole model explains most of the data with a small number of free parameters [137]. For this experiment, we have searched for two, four and six dipoles. The dipole locations were

(a)

(b)

Figure 7.19: (a) The subject (the author of this thesis) with the electrode cap. (b) Süha Yağcıoğlu and Nevzat Gençer injecting gel into the electrodes.

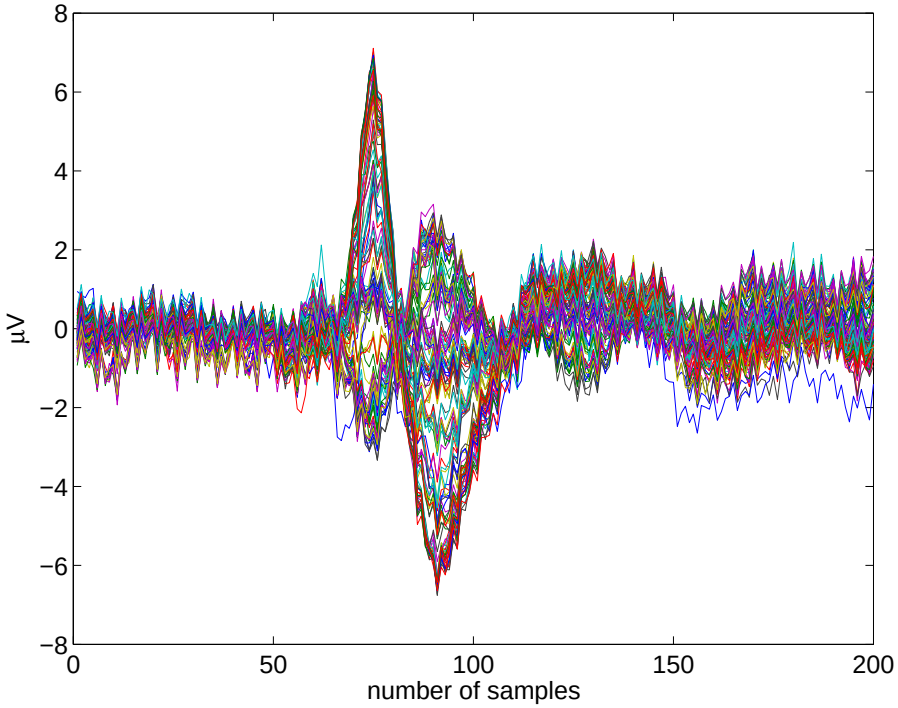

(a)

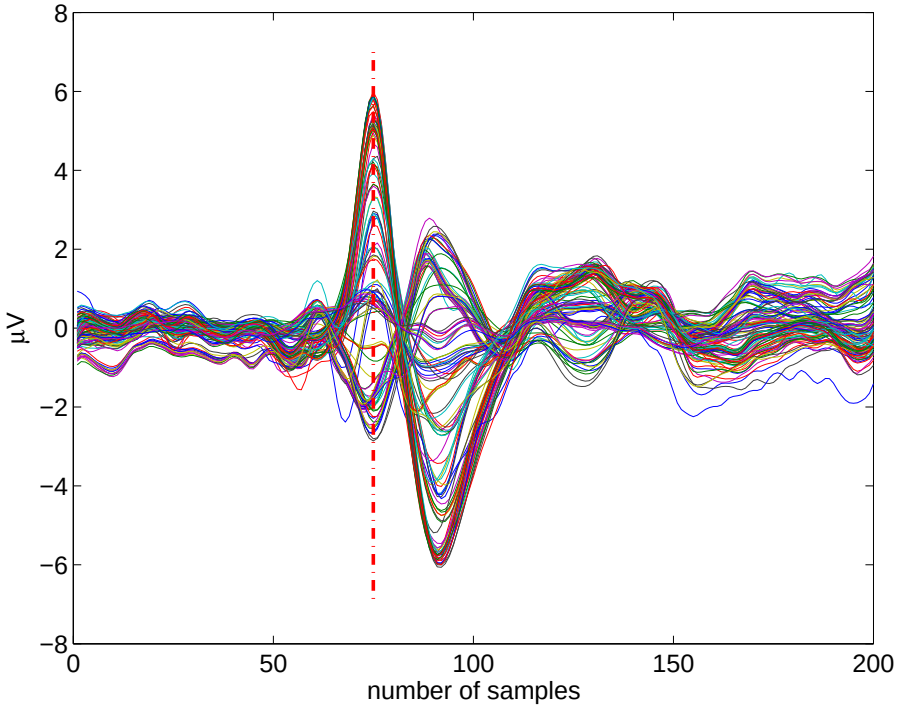

(b)

Figure 7.20: Acquired EEG data for all channels. Each channel is plotted with a different color. (a) Before filtering, (b) after filtering. The Red line shows the specific time instant where the data of 128 channels are used for source localization.

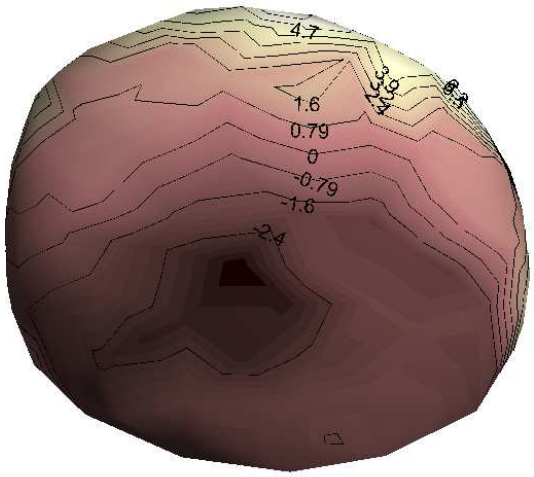

(a)

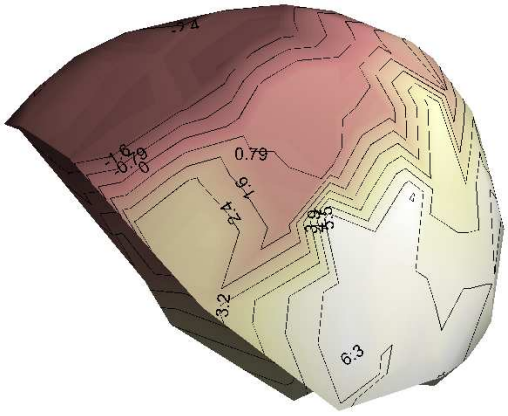

(b)

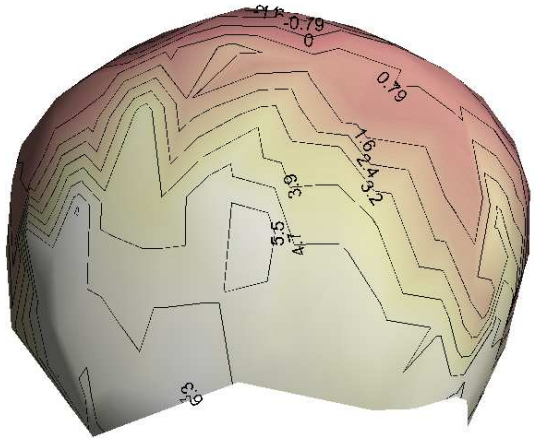

(c)

Figure 7.21: Topographic view of the electrode potentials on the scalp surface with 1 kHz stimulus, (a) top view, (b) left view, (c) back view. The time instant corresponding to this potential profile is shown in Figure 7.20(b)

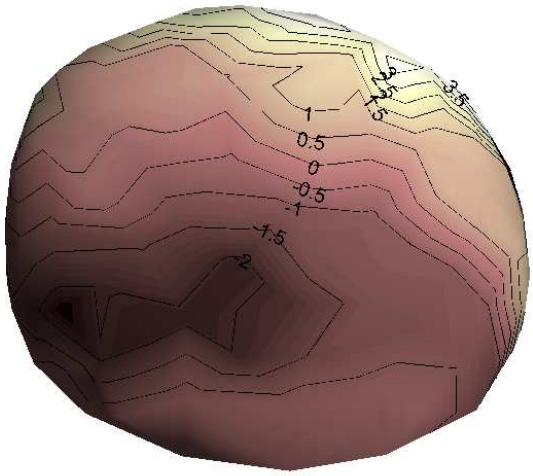

(a)

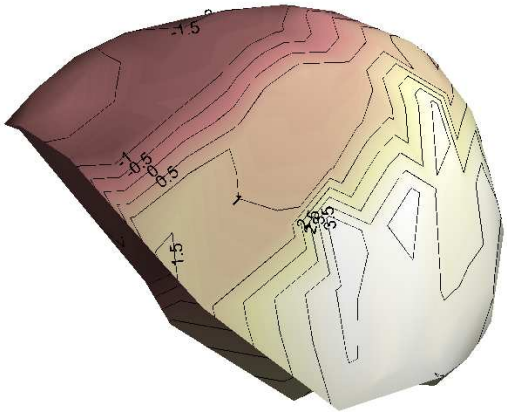

(b)

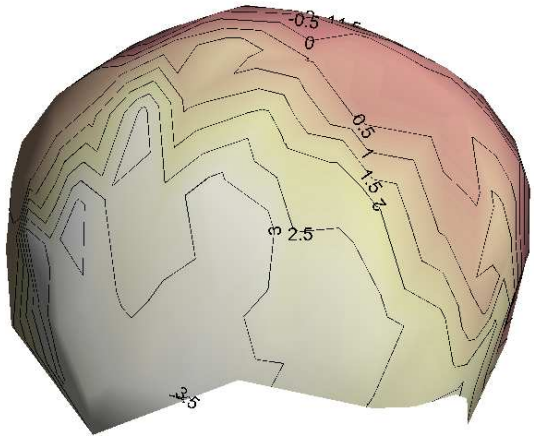

(c)

Figure 7.22: Topographic view of the electrode potentials on the scalp surface with 5 kHz stimulus, (a) top view, (b) left view, (c) back view. The time instant corresponding to this potential profile is shown in Figure 7.20(b)

Table 7.6: The RDM (%) values for the auditory experiment, showing the error between the measured data and field computed from the localized dipoles. The localization results for both spherical and realistic head models are shown.

Dipoles	Stimulus	Realistic	Spherical
2	1 kHz	35.81	41.11
2	5 kHz	40.27	47.09
4	1 kHz	26.15	32.87
6	1 kHz	23.41	24.72

constrained to be symmetric along the median of the brain.

The auditory data is localized using the GA implementation described in the previous sections. For the localization 2, 4 and 6 symmetric dipole pairs are searched using the realistic head model. The localized dipoles are plotted on the nearest MR slice, and on coronal, axial and sagittal mesh cross-sections. For the 2 dipole search the results are presented for 1 kHz and 5 kHz stimuli. Figures 7.23 and 7.25 illustrate the axial dipole locations for the 1 kHz and 5 kHz stimuli respectively. The corresponding (a) coronal and (b) sagittal views are presented in Figure 7.24 and Figure 7.26. These figures show that the localized sources for 1 kHz stimulus are deeper compared with the 5 kHz stimulus. For the 4 and 6 dipole localizations, the results for the 1 kHz stimulus is shown. For the 4 dipole case, figures 7.27 and 7.28 illustrate the source locations for all four views. The average dipole location is close to the sources located in the 2 dipole case. Similarly, locations of 6 dipoles are presented in Figure 7.27 and Figure 7.28. The localized sources are determined to be near the Heschl's gyrus (Figure 7.31) on which the auditory responses are detected in previous research [11], [137], [176], [195].

Table 7.6 presents %RDM between the localized sources and measurements, which indicates the amount source localizations explain the measured data. Localization results for both spherical and realistic head models are shown. When the number of dipoles is increased from 2 to 4, the difference between the measured and calculated data decreases from 35% to 26% for the realistic model. It decreases to 32% for the spherical model. Increasing the number of dipoles to 6 reduces the RDM by an additional 3% for the realistic case,

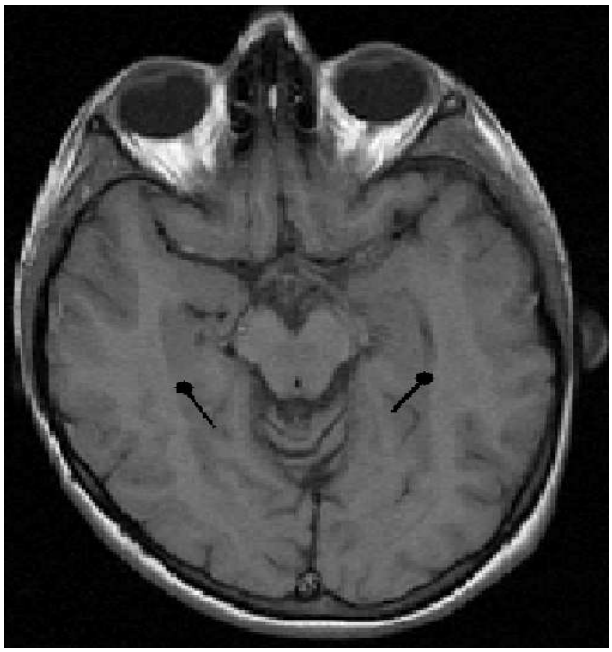

(a)

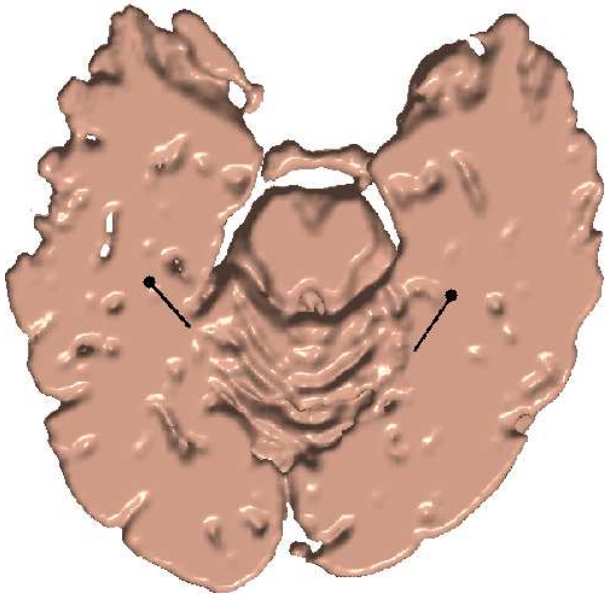

(b)

Figure 7.23: Location of the estimated dipoles for the 1kHz stimuli shown (a) on the axial MR slice, (b) on the segmented axial brain slice. Activities of each temporal lobe are presented using a single equivalent dipole.

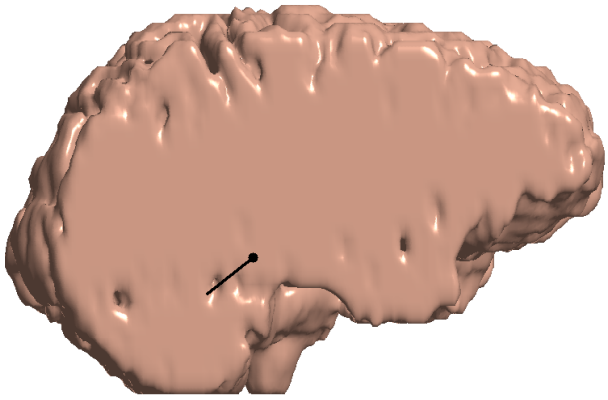

(a)

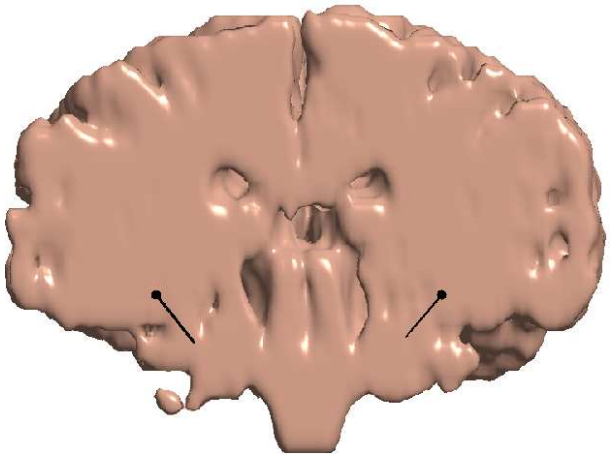

(b)

Figure 7.24: Location of the estimated dipoles for the 1kHz stimuli shown on the segmented brain slices (a) sagittal view, (b) coronal view. Activities of each temporal lobe are presented using a single equivalent dipole.

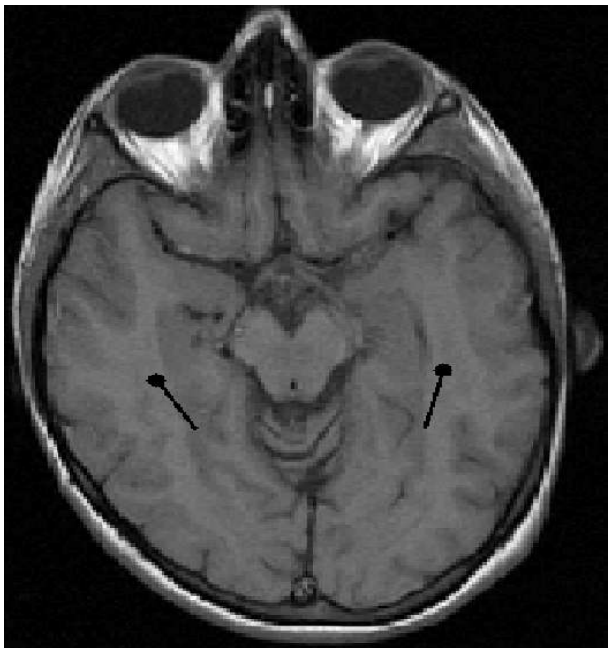

(a)

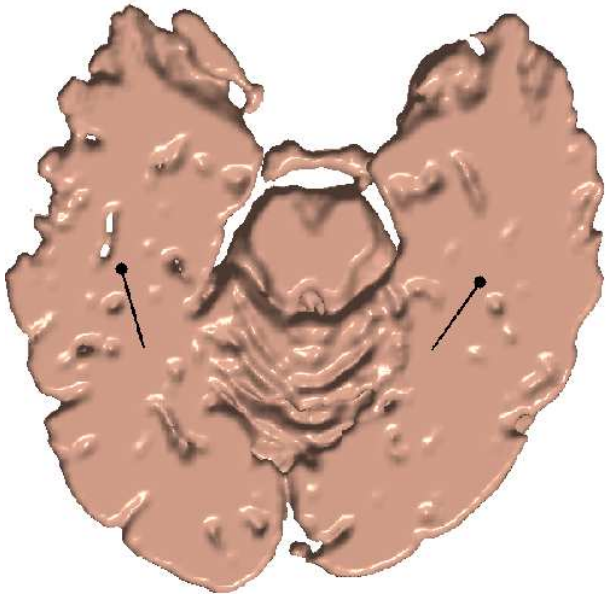

(b)

Figure 7.25: Location of the estimated dipoles for the 5kHz stimuli shown (a) on the axial MR slice, (b) on the segmented axial brain slice. Activities of each temporal lobe are presented using a single equivalent dipole.

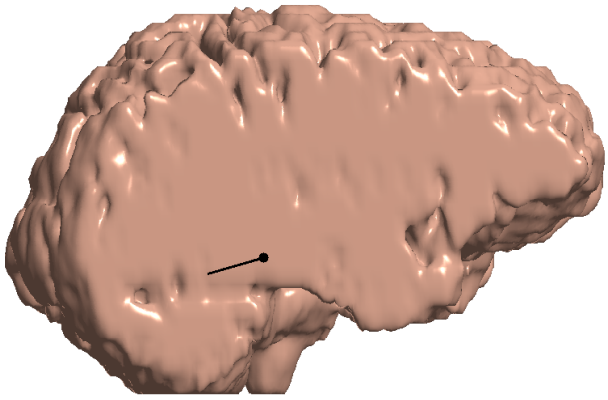

(a)

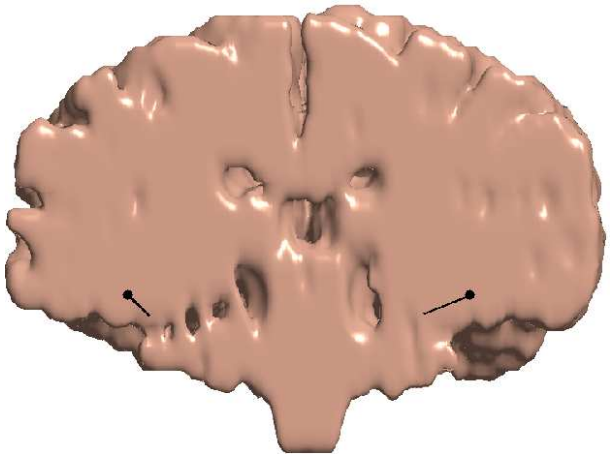

(b)

Figure 7.26: Location of the estimated dipoles for the 5kHz stimuli shown on the segmented brain slices (a) sagittal view, (b) coronal view. Activities of each temporal lobe are presented using a single equivalent dipole.

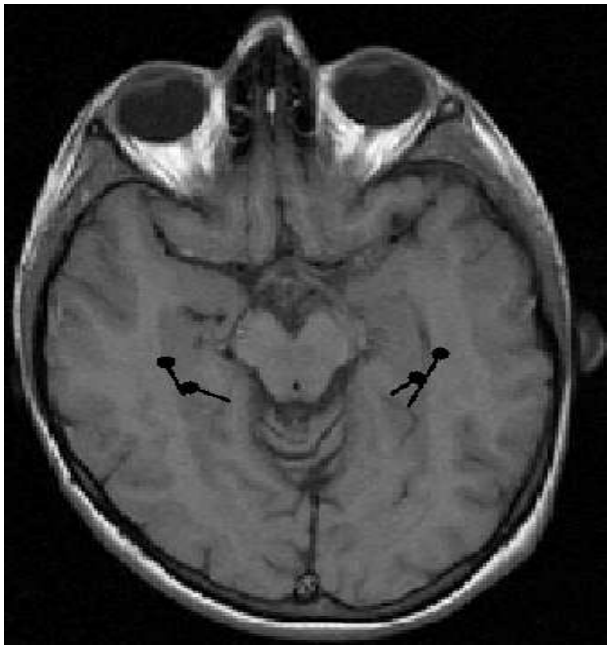

(a)

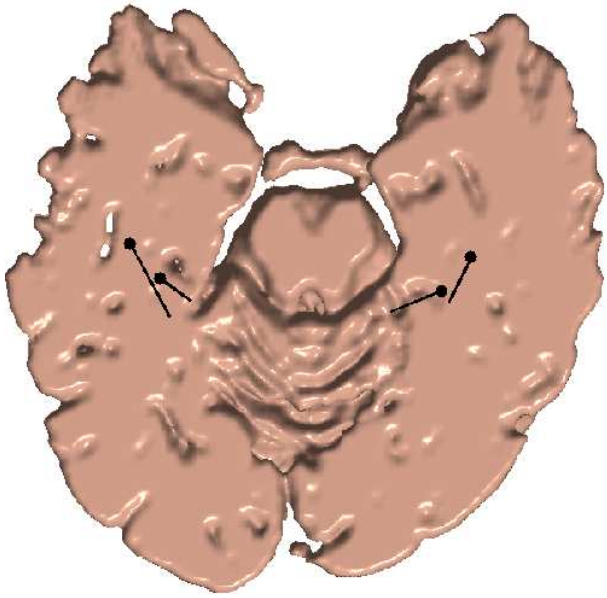

(b)

Figure 7.27: Location of the estimated dipoles for the 1kHz stimuli shown (a) on the axial MR slice, (b) on the segmented axial brain slice. Activities of each temporal lobe are presented using two equivalent dipoles.

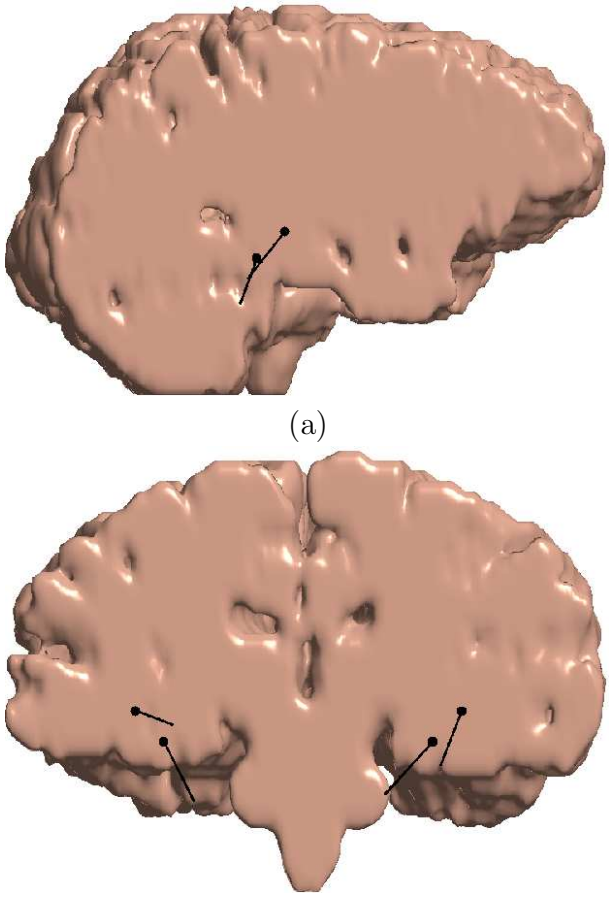

(a)

(b)

Figure 7.28: Location of the estimated dipoles for the 1kHz stimuli shown on the segmented brain slices (a) sagittal view, (b) coronal view. Activities of each temporal lobe are presented using two equivalent dipoles.

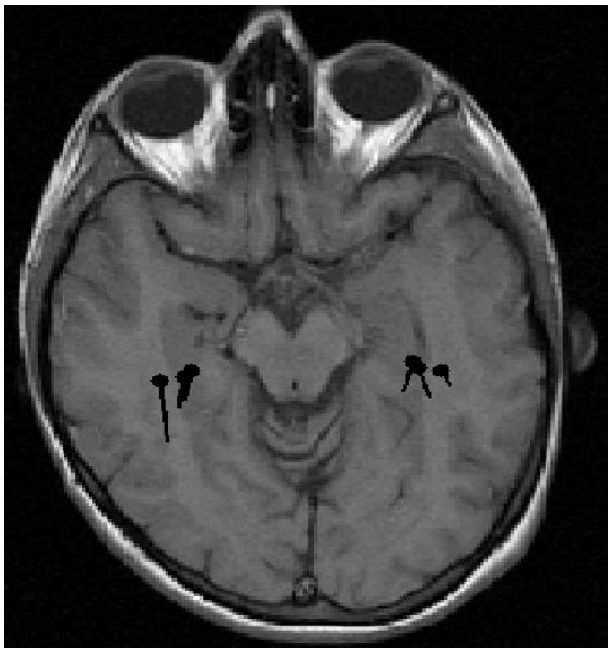

(a)

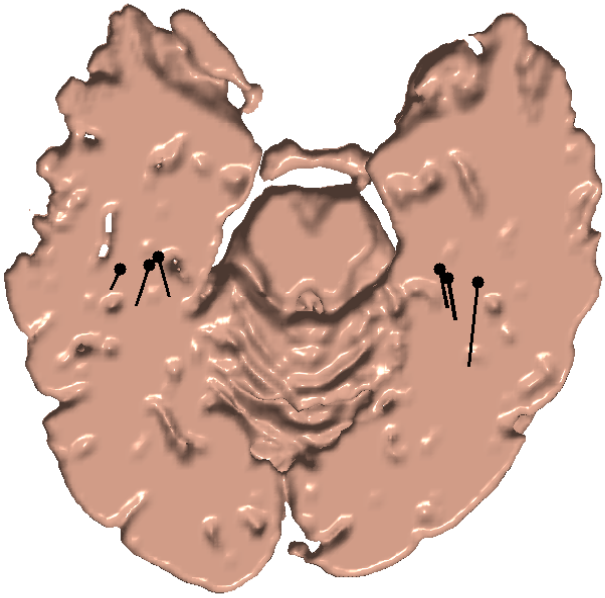

(b)

Figure 7.29: Location of the estimated dipoles for the 1kHz stimuli shown (a) on the axial MR slice, (b) on the segmented axial brain slice. Activities of each temporal lobe are presented using three equivalent dipoles.

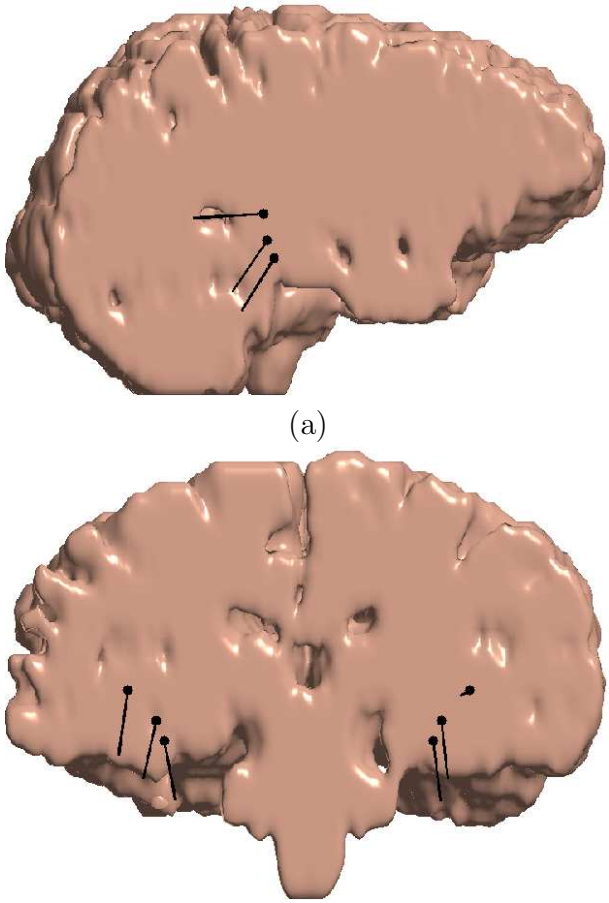

(a)

(b)

Figure 7.30: Location of the estimated dipoles for the 1kHz stimuli shown on the segmented brain slices (a) sagittal view, (b) coronal view. Activities of each temporal lobe are presented using three equivalent dipoles.

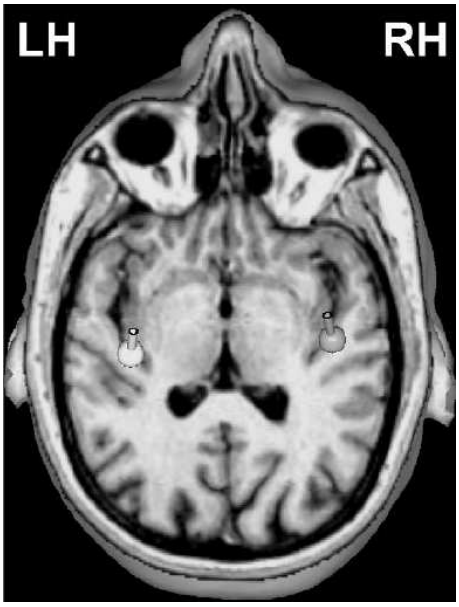

Figure 7.31: The location of Heschls gyrus where the auditory sources are found. (This figure is reproduced from [11].)

and 8% for the spherical case. From these results, it can be concluded that 6 dipole localizations explain more than 75% of the measurements.

CHAPTER 8

CONCLUSION AND DISCUSSION

This study describes a fast and accurate BEM implementation and a novel approach for creating detailed realistic BEM models from the multi-modal MR images. The implementation uses second-order isoparametric elements, and applies the IPA and recursive integration techniques for improved accuracy.

8.1 Accuracy of the BEM

The accuracy of the original BEM formulation [51] was improved by using the recursive integration technique and tested using the Rush and Driscoll head model [40]. For a specific head model of 512 elements and 1026 nodes on each surface, the maximum RDM decreases to 2.2% for a dipole located 2 mm apart from the skull.

To increase the accuracy of the forward problem solutions with the boundary element head models, the IPA must be applied. In general, a single layer is assumed in the skull. For realistic head models with arbitrary number of layers in the skull, a generalized version of the IPA is required. In this study, a generalized formulation for the IPA was described. The related integral equations and the discretized version of the modified source terms were presented. Two formulations were derived for the generalized version of the IPA. The matrix equation given in Equation (3.8) is suitable for a general multi-layer implementation where there are arbitrary number of layers in the skull. The integral equations for this case have also been described in [48]. However, the alternative form Equation (3.10) is more efficient when there is a single layer

inside the skull layer since no sub-matrices ($\mathbf{C}_{ij}$) are needed to be stored and used. The matrix equations of the alternative formulation are reduced to the equations given by [49] for a three layer head model.

The accuracy obtained by the new formulation was tested with spherical 4-layer models. After validating the IPA for spherical models, the effect of the CSF layer and a tumor tissue was investigated using the generalized form of the IPA in a realistic head model. The effect of the IPA was also investigated for an inhomogeneity in the brain. For a 4-layer spherical model, it was observed that the application of the IPA improves the RDM for both deep and shallow dipoles. The improvement in RDM*, however, was apparent for only shallow dipoles. For a radial dipole that is 1 mm close to the brain surface, the RDM* dropped from 1.88 to 0.03. The corresponding %RDM decreased from 227.9% to 9.9%.

Using the realistic head model, we have investigated the effect of three factors on the forward problem solutions: 1) The effect of the CSF layer, 2) the effect of an inhomogeneity with varying conductivities in the brain, 3) the effect of the IPA using the realistic model including the inhomogeneity in the brain.

The effect of the CSF layer and the inhomogeneity were investigated by comparing the potentials for a reference BEM model with the potentials for two different head models: the same model without CSF, and the model with an inhomogeneity inside the brain. It was observed that including the CSF layer changed the scale of the potentials considerably; the field pattern, on the other hand, did not change noticeably. The inclusion of an inhomogeneity with 0.033 S/m changed the scale of the potentials by 50% and the pattern by 25% for a dipole oriented toward the inhomogeneity. It was observed that an inhomogeneity shifts the pattern of the potentials and affects the magnitude of the measurements, in effect acting like a secondary source.

The effect of the IPA was investigated when there is an inhomogeneity in the brain. It was observed that in addition to a considerable change in the scale of the potentials, the RDM* also changed by 15%. The application of

the IPA also made an observable change in the field profiles. A shift in the location of the extrema was observed. The effect of the IPA on the accuracy of the forward problem was estimated to be more pronounced for realistic head models compared with the spherically symmetric models.

It may be argued whether a low conductivity inhomogeneity inserted in the isolated region would cause a numerical inaccuracy in the solutions. For a multi-layer inhomogeneity in the brain, the low conductivity outer layer would decrease the potentials in the inner layers of the inhomogeneity, and an inaccuracy in solutions may be expected. To reduce the inaccuracy, the isolated problem should then be defined for a geometry bounded from two surfaces: the inner surface of the skull layer and the outer surface of the inhomogeneity. In this study, we have not investigated the inaccuracy for such a multi-layer inhomogeneity. However, the accuracy for a single-layer inhomogeneity was tested. For that purpose, a four layer spherical BEM model representing scalp, skull, brain and a low conductivity single-layer inhomogeneity (0.033 S/m) was developed. Since the analytical expression allow source locations only in the innermost shell, a FEM model is generated [56], [74] and the solutions at the outer surface obtained using the two numerical methods are compared. The RDM was found less than 1% for various dipole locations and orientations. Thus, we have concluded that a low-conductivity single-layer inhomogeneity does not cause any numerical inaccuracy in the BEM solutions.

8.2 Accelerated BEM

Two new formulations were developed to compute the transfer matrices of EEG and MEG. The formulations allow the use of the IPA with the corresponding transfer matrices. The formulations presented in Section 2.3 and Section 2.4 assumes a three-layer realistically shaped head model. For multi-layer head models the formulations are updated in Section 3.3 and Section 3.4.

The computation times of the transfer matrices are 3.2 hours when a PC (Pentium IV, 2.4 MHz) and a nonoptimized iterative solver (biconjugate gradient method) is used for calculations. Note that this can be further reduced by

using better iterative algorithms, preconditioning, and optimized solvers. Once these matrices are calculated, the forward problem solutions for a realistic head model can be obtained using simple matrix multiplications in milliseconds.

In this study, we have focused on the computation of the MEG transfer matrix for a fixed head/helmet configuration. The transfer matrix method that we have proposed is computationally efficient compared to the conventional approach (where the potential of all nodes are calculated). This is especially evident for the inverse problem solutions that require large number of forward problem calculations.

If the head movements are to be taken into account, corresponding sensor positions must be recorded appropriately [196]. To use this information in the inverse problem, we may propose the following two approaches: 1) a different transfer matrix can be calculated for each head position, 2) a larger (parent) transfer matrix can be computed corresponding to a sensor set that covers a larger sensor area. The computation time for the first solution will be considerably longer compared to the case of single transfer matrix computation (for a fixed head/helmet configuration). However, we may expect smaller error in the source localization. The second solution, however, can be computationally more efficient. The rows of the transfer matrix corresponding to a specific sensor set can be calculated from the parent matrix by using interpolation techniques. The advantages/disadvantages of these techniques must be further investigated by simulation studies.

8.3 Head modeling

To obtain realistic head models, a semi-automatic segmentation algorithm was developed to extract the scalp, skull, WM, GM and eye tissues from MR images. The algorithm was tested on simulated data downloaded from the BrainWeb, as well as on real MR data. It was observed that the segmentation algorithm is capable of detecting the main tissues of the head with their characteristic features. However, the segmentation algorithm needs to be further automated, and validated on different individuals before being put to regular

use.

A mesh generation algorithm was developed for creating meshes from the segmented volumes. The mesh generation algorithm uses triangulation, filtering, coarsening and topological correction operations to generate high quality meshes. The mesh generation algorithm has two important features: 1) the ability to create meshes for intersecting tissue boundaries, and 2) generation of realistic meshes with second-order elements. The eye tissues are included by creating a mesh that conforms to the intersecting boundaries of the outer skull and eyes. The advantages of using high-order elements were presented previously [51]. However, these elements have not been used in the realistic models as it was difficult to fit them to the complex head geometry. By integrating second-order element generation process into the coarsening algorithm it is now possible to use second-order elements in the realistic BEM models.

The realistic head model developed in this study was used to investigate the effects of eye conductivity on the forward problem solutions. Dipoles 1.5 cm apart from an eye surface caused changes in the potential pattern yielding RDMs on the order of 2–6%. Thus if surface voltages are to be used for source localization, eyes should be included in the head model. This is especially necessary when the sources are assumed in the pre-frontal cortex. Including eyes in the head model produced negligible effect in the magnetic field solutions (i.e., the RDMs were below 0.1%).

The realistic head modeling approach of this study can be used in future advanced BEM implementations to investigate the effects of other complex features, such as tumors and skull defects, in the head.

8.4 Inverse Problem

The accelerated BEM implementation allows rapid computation of electrode potentials and magnetic fields at the sensors. This makes it possible to use a global optimization algorithms such as the GA in realistic head models, to solve the inverse problem of the EMSI. The GA was first applied using a spherical 4-layer BEM model with Monte-Carlo simulations for a single dipole

search. Assuming a 64 electrode configuration, the results are tested using analytically calculated forward problem solutions. It was observed that the localization errors are less than 2 mm for an SNR of 10, and less than 4 mm for an SNR of 5. Next, simulation studies with realistic head models were done. The effects of the eye tissues, and the CSF tissues on the IP solutions were explored. For this purpose, three different realistic BEM head models were generated. It was observed that for the EEG measurements the effect of the eye conductivity was more important than for the MEG measurements. But the presence of the CSF layer effects the IP solutions using both EEG and MEG measurements. For the EEG measurements, absence of the eye tissue increases the localization error from 1.1 mm to 3 mm, while MEG error increases from 1.2 mm to 1.4 mm. When the CSF is removed, EEG error increases to 6 mm, and MEG error becomes 4 mm. When a single-dipole source in a realistic model is explored using a best-fit spherical model, the localization errors increase up to 8.5 mm for EEG and 7 mm for MEG.

Multiple dipole localizations are also tested using a specific dipole configuration. A face-to-face dipole configuration is chosen which represents the worst-case setup when the face-to-face dipoles are close to each other. The performance in localization is quite similar to a single dipole case, when the distance between the face-to-face dipoles is large (4 cm). As the dipoles get closer (1 cm), the realistic model still provides better results, however, its performance degrades. Note that, when the distance between the dipoles approaches to zero, the corresponding potentials will completely cancel each other. For such an extreme case, the selected model (realistic or spherical) will not be important. In general, it was shown that the source localization using realistic head models provides definitely more accurate results.

To test the EMSI framework developed in this thesis study with experimental data, auditory experiments were performed using a 128–channel EEG system built in Hacettepe University, Faculty of Medicine, Biophysics Department. The acquired experimental data was used to localize the sources of the auditory evoked responses using two head models (spherical and realistic). The

P1 component of the recordings was investigated assuming a single dipole, two dipoles and three dipoles at each temporal lobes. The reconstructed source locations are found in the Heschl's gyrus which comply with the results obtained in the literature. The difference between the measured and the calculated data is 35% when the realistic model is used. The corresponding error is 41% when the spherical model is assumed. If 3 dipoles are used for each temporal region, these differences are 23% for the realistic model, and 25% for the spherical model.

In this thesis study, by developing new techniques, and integrating and improving existing algorithms, an accurate and high performance EMSI source localization framework have been developed. Using the developed platform, it has been possible to solve the source localization problem on realistic head models with reasonable computation times, even when a *slow* algorithm, such as GA, is used for solving the inverse problem. This research allows modeling and localization of sources from experimental data, and provide opportunities for further research.

REFERENCES

[1] Liu G. R., *Computational Inverse Techniques in Nondestructive Evaluation*, CRC Press, 2003.

[2] J. Malmivuo and R. Plonsey, *Principles and Applications of Bioelectric and Biomagnetic Fields*, Oxford University Press, New York, 1995.

[3] E. R. Kandel, J. H. Schwartz, and T. M. Jessell, *Principles of Neural Science*, Appleton and Lange, Norwalk, Conneticut, 1991.

[4] "Pathalogy: A comperative study guide," http://medocs.ucdavis.edu/PMD/study_aid/, Last accessed date June 2005.

[5] B. Vanrumste, *EEG dipole source analysis in a realistic head model*, PhD Thesis, University of Gent, 2000.

[6] E. J. Speckmann and Elger C. E., *Electroencephalography, Basic Principles, Clinical Applications and Related Fields*, vol. 1-16, Urban and Schwarzenberg.

[7] "The neuroscan homepage," http://www.neuroscan.com/, Last accessed date June 2005.

[8] "The 4-d neuroimaging homepage," http://www.4dneuroimaging.com/, Last accessed date June 2005.

[9] G. Taubin, "A signal processing approach to fair surface design," in *Proc. of Siggraph*, 1995, pp. 351–358.

[10] P. S. Heckbert and M. Garland, "Optimal triangulation and quadric-based surface simplification," *Computational Geometry*, vol. 14, pp. 49–65, 1999.

[11] P. Schneider, M. Scherg, H. G. Dosch, H. J. Specht, A. Gutschalk, and A. Rupp, "Morphology of heschl's gyrus reflects enhanced activation in the auditory cortex of musicians," *Nature Neuroscience*, pp. 688–694, 2002.

[12] P. L. Nunez, *Electric Fields of the Brain*, Oxford University Press, New York, Oxford, 1981.

[13] H. Berger, "über das elektrenkephalogramm das menchen," *Archiv für Psychiatrie*, vol. 87, pp. 527–570, 1929.

[14] S. Baillet, J. C. Mosher, and R. M. Leahy, "Electromagnetic brain mapping," *IEEE Signal Proc. Mag.*, vol. 18, pp. 14–30, 2001.

[15] J. Sherman A. Vander and D. Luciano, *Human Physiology*, McGraw-Hill, 1998.

[16] G. D. Dawson, "Cerebral responses to electrical stimulation of peripheral nerves in man," *J. Neurol. Neurosurg. Psychiatry*, vol. 10, pp. 137–140, 1947.

[17] J.P. Karjalainen, A. Kaipio, Koistinen, and Vauhkonen M., "Subspace regularization method for the single trial analysis of evoked potentials," *IEEE Trans. Biomed. Eng.*, vol. 46, pp. 849–860, 1999.

[18] J.E. Zimmerman, P. Thiene, and J.T. Harding, "Design and operation of stable rf-biased superconducting point-contact quantum devices and a note on the properties of perfectly clean metal contacts," *J. Appl. Phys.*, vol. 41, pp. 1572–1580, 1970.

[19] L. D. Cohen, "Manetoencephalography: Detection of the brain's electrical activity with a superconducting magnetometer," *Science*, vol. 175, pp. 664–666, 1972.

[20] D. Brenner, S.J. Williamson, and L. Kaufman, "Visually evoked magnetic fields of the human brain," *Science*, vol. 190, pp. 480–482, 1975.

[21] T.J. Teyler, B.N. Cuffin, and D. Cohen, "The visual evoked magnetoencephalogram," *Life Sci.*, vol. 17, pp. 683–692, 1975.

[22] J. C. De Munck, B. W. Van Dijk B W, and H. Spekreijse, "Mathematical dipoles are adequate to describe realistic generators of human brain activity," *IEEE Trans. Biomed. Eng.*, vol. 35, no. 11, pp. 960–966, 1988.

[23] K. Jerbi, S. Baillet, J.C. Mosher, G. Nolte, L. Garnero, and R.M. Leahy, "Localization of realistic cortical activity in MEG using current multipoles," *NeuroImage*, vol. 22, pp. 779–793, 2004.

[24] R. Plonsey and R. C. Barr, *Bioelectricity - A Quantitative Approach*, Plenum Press, New York and London, 1991.

[25] J. Lötjönen, *Construction of Boundary Element Models in Bioelectromagnetism*, PhD. Thesis, Helsinki University of Technology Espoo, Finland, 2000.

[26] E. Frank, "Electric potential produced by two point current sources in a homogeneous conduction sphere.," *Journal of Applied Physics*, vol. 23, no. 11, pp. 1225–1228, 1952.

[27] F. Grynszpan and D. B. Geselowitz, "Model studies of the magnetocardiogram," *Biophys. J.*, vol. 13, pp. 911–925, 1973.

[28] D. B. Geselowitz, "Model studies of the electric and magnetic fields of the heart," *Jour. Franklin. Inst.*, vol. 296, no. 6, pp. 379–391, 1973.

[29] N. B. Cuffin and D. Cohen, "Magnetic fields of a dipole in special volume conductor shapes," *IEEE Trans. Biomed. Eng.*, vol. 24, no. 4, pp. 372–381, 1977.

[30] J. C. Lin and D. M. Durand, "Magnetic field of current monopoles in prolate and oblate spheroid volume conductors," *IEEE Trans. on Magnetics*, vol. 34, pp. 2177–2184, 1998.

[31] P. M. Berry, "N, m space harmonics of the oblate spheroid," *Annals New York Acad. of Sci.*, vol. 65, pp. 1126–1134, 1956.

[32] R. N. Kavanagh, T. M. Darcey, D. Lehmann, and D. H. Fender, "Evaluation of method for three-dimensional localization of electrical sources in the human brain," *IEEE Trans. Biomed. Eng.*, vol. 25, pp. 421–429, 1978.

[33] J. C. De Munck, "The potential distribution in a layered anisotropic spheroidal volume conductor," *Journal of Applied Physics*, vol. 64, no. 2, pp. 464–470, 1988.

[34] C. J. Henderson and S. R. Butler, "The localization of equivalent dipoles of EEG sources by the application of electrical field theory," *Neurophysiol.*, vol. 39, no. 117-130, 1975.

[35] D. Cohen, N. B. Cuffin, K. Yunokuchi, R. Maniewski, C. Purcell, R. G. Cosgrove, J. Ives, J. G. Keneddy, and L. D. Schomer, "MEG versus EEG localization test using implanted sources in the human brain," *Annals of Neurology*, vol. 28, no. 6, pp. 811–817, 1990.

[36] D. S. Barth, W. Sutherling, J. Broffman, and J. Beatty, "Magnetic localization of a dipolar current source implanted in a sphere and a human cranium," *Electroenceph. Clin. Neurophysiol.*, vol. 63, 1986.

[37] H. Weinberg, P. Brickett, F. Coolsma, and M. Baff, "Magnetic localization of intracranial dipoles: simulation with a physical model," *Electroenceph. Clin. Neurophysiol.*, vol. 64, pp. 159–170, 1986.

[38] Z. Zhang and D. Jewett, "Insidious errors in dipole localization parameters at a single time-point due to model misspecification of number of shells," *Electroenceph. Clin. Neurophysiol.*, vol. 88, pp. 1–11, 1993.

[39] Z. Zhang, D. Jewett, and G. Goodwill, "Insidious errors in dipole parameters due to shell model misspecification using multiple time points," *Brain Topography*, vol. 6, pp. 283–298, 1994.

[40] S. Rush and D. A. Driscoll, "Current distribution in the brain from the surface electrodes," *Anesthesia and Analgesia, Current res.*, vol. 47, pp. 717–723, 1968.

[41] M. Schneider, "Effect of inhomogeneities on surface signals coming from a cerebral current dipole source," *IEEE Trans. Biomed. Eng.*, pp. 52–54, 1974.

[42] R. D. Sidman, V. Giambalvo, T. Allison, and P. Bergey, "A method for localization of sources of human cerebral potentials evoked by sensory stimuli," *Sensory Proc.*, vol. 2, pp. 116–129, 1978.

[43] T. M. Darcey, J. P. Ary, and D. H. Fender, "Methods for the localization of electrical sources in the human brain," *Progr. Brain. Res.*, vol. 54, pp. 128–134, 1980.

[44] N. B. Cuffin, "Eccentric spheres models of the head," *IEEE Trans. Biomed. Eng.*, vol. 38, no. 9, pp. 871–878, 1991.

[45] N. B. Cuffin, "EEG localization accuracy improvements using realistically shaped head models," *IEEE Trans. Biomed. Eng*, vol. 44, no. 3, pp. 299–303, 1996.

[46] S. Ueno, K. Irmina, H. Ozaki, and K. Harada, "The MEG topography and the source model of abnormal neural activities associated with brain lesions," *IEEE Trans. Magn.*, vol. 22, pp. 874–876, 1986.

[47] S. Ueno, K. Irmina, and K. Harada, "Effects of inhomogeneities in cerebral modeling for magneto-encephalography," *IEEE Trans. Magn.*, vol. 23, pp. 3753–3755, 1987.

[48] J. W. H. Meijs, O. Weier, and M. J. Peters, "On the numerical accuracy of the boundary element method," *IEEE Trans. Biomed. Eng.*, vol. 36, pp. 1038–1049, 1989.

[49] M. S. Hämäläinen and J. Sarvas, "Realistic conductivity geometry model of the human head for interpretation of neuromagnetic data," *IEEE Trans. Biomed. Eng.*, vol. 36, no. 2, pp. 165–171, 1989.

[50] N. B. Cuffin, "A method for localizing EEG sources in realistic head models," *IEEE Trans. Biomed. Eng*, vol. 42, no. 1, pp. 68–71, 1995.

[51] N. G. Gençer and I. O. Tanzer, "Forward problem solution of electromagnetic source imaging using a new BEM formulation with high- order elements," *Phys. Med. Biol.*, vol. 44, pp. 2275–2287, 1999.

[52] Finke S. and Gulrajani R. M., "Conventional and reciprocal approaches to the forward problem of electroencephalography," *Electromagetics*, vol. 21, pp. 513–530, 2001.

[53] M. Thevenet, O. Bertrand, F. Perrin, T. Dumont, and J. Pernier, "The finite element method for a realistic head model of electrical brain activities: preliminary results.," *Clin. Phys. Physiol. Meas.*, vol. 12. Suppl. A., pp. 89–94, 1991.

[54] Y. Yan, P. L. Nunez, and R. T. Hart, "A finite lement model for the human head: scalp potentials due to dipole sources," *Med. Biol. Eng. Comp.*, vol. 29, pp. 475, 1991.

[55] J. Haueisen, C. Ramon, P. Czapski, and M. Eiselt, "On the influence of volume currents and extended sources on neuromagnetic fields: A simulation study," *Anna. Biomed. Eng.*, vol. 23, pp. 728–739, 1995.

[56] N. G. Gençer and C. E. Acar, "Sensitivity of EEG and MEG measurements to tissue conductivity," *Physics in Med.and Biol.*, vol. 49, pp. 701–717, 2004.

[57] J. B. Nixon, P. E. Rasser, M. D. Teubner, C. R. Clark, and M. J. Bottema, "Numerical model of electrical potential within the human head," *Int. J. for numerical methods on Eng.*, vol. 56, no. 15, pp. 2353–2366, 2003.

[58] B. Vanrumste, G. Van Hoey, R. Van de Walle, M. R. P. D'Have, I. A. Lemahieu, and P. A. J. M. Boon, "The validation of the finite difference method and reciprocity for solving the inverse problem in EEG dipole source analysis," *Brain Topography*, vol. 14, no. 2, pp. 83–92, 2001.

[59] Z. Akalın-Acar and N. G. Gençer, "An advanced boundary element method (BEM) implementation for the forward problem of electromagnetic source imaging," *Physics in Medicine and Biology*, vol. 49, pp. 5011–5028, 2004.

[60] C. H. Wolters, L. Grasedyck, and H. Hackbusch, "Efficient computation of lead field bases and influence matrix for the FEM-based EEG and MEG inverse problem," *Inverse Problems*, vol. 20, pp. 1099–1116, 2004.

[61] J. J. Ermer, J. C. Mosher, S. Baillet, and R. M. Leahy, "Rapidly recomputable EEG forward models for realistic head shapes," *Physics in Medicine and Biology*, vol. 46, pp. 1265–1281, 2001.

[62] B. Yvert, A. Crouzeix-Cheylus, and J. Pernier, "Fast realistic modeling in bioelectromagnetism using lead-field interpolation," *Hum. Brain Mapp.*, vol. 14, pp. 48–63, 2001.

[63] B. J. Roth, M. Balish, A. Gorbach, and S. Sato, "How well des a three-sphere model predict positions of dipoles in a realistically shaped head?," *Electroenceph. Clin. Neurophysiol.*, vol. 87, pp. 175–184, 1993.

[64] A. Crouzeix, B. Yvert, O. Bertrand, and J. Pernier, "An evaluation of dipole reconstruction accuracy with spherical and realistic head models in MEG," *Clin. Neurophysiol.*, vol. 110, pp. 2176–2188, 1999.

[65] C. Ramon, P. Schimpf, J. Haueisen, M. Holmes, and A. Ishimaru, "Role of soft bone, csf and gray matter in EEG simulations," *Brain Topography*, vol. 16, no. 4, pp. 245–248, 2004.

[66] H. Hemholtz, "Ueber einiger gezetze der vertailung elektrischer strome in korperlichen leiter mit anwendungauf die thierishch electrischeb versuche," *Pogg Ann Physik Chemie*, vol. 33, pp. 353–377, 1853.

[67] F. Darvas, D. Pantazis, E. Kucukaltun-Yildirim, and R. M. Leahy, "Mapping human brain function with MEG and EEG methods and validation," *NeuroImage*, vol. 23, pp. S289–S299, 2004.

[68] C. M. Michel, M. M. Murray, G. Lantz, L. Gonzales, S. Spinelli, and R. G. de Peralta, "EEG source imaging," *Clin. Neurophysiol*, vol. 115, no. 10, pp. 2195–2222, 2004.

[69] J. H. M. Frijns, S. L. de Snoo, and R. Schoonhoven, "Improving the accuracy of the boundary element method by the use of second-order interpolation functions," *IEEE Trans. Biomed. Eng.*, vol. 47, no. 10, pp. 1336–1346, 2001.

[70] N. G. Gençer and Z. Akalın-Acar, "Use of the isolated problem approach for multi-compartment BEM models of electro-magnetic source imaging," *Physics in Med. and Biol.*, vol. 50, pp. 3007–3022, 2005.

[71] D. Kozinska, F. Carducci, and K. Nowinski, "Automatic alignment of EEG/MEG and MRI data sets," *Clin. Neurophysiol.*, vol. 112, pp. 1553–1561, 2001.

[72] C. M. Michel, G. Thut, S. Morand, A. Khateb, A. J. Pegna, R. G. de Peralta, S. Gonzales, M. Seeck, and T. Landis, "Electric source imaging of human brain functions," *Brain Research Reviews*, vol. 36, no. 2-3, pp. 108–118, 2001.

[73] B. He, "High-resolution source imaging of brain electrical activity," *IEEE Eng. Med. and Biol.*, vol. 17, no. 5, pp. 123–129, 1998.

[74] N. G. Gençer, C. E. Acar, and I. O. Tanzer, *Magnetic Source Imaging of the Human Brain*, chapter Forward problem solution of magnetic source imaging, pp. 77–100, Hillsdale, NJ: Lawrence Erlbaum Associates, 2003.

[75] J. Budiman and D. S. Buchanan, "An alternative to the biomagnetic forward problem in a realistically shaped head model, the "weighted vertices"," *IEEE Trans. Biomed. Eng.*, vol. 40, no. 10, pp. 1048–1053, 1993.

[76] D. J. Fletcher, A. Amir, D. L. Jewett, and G. Fein, "Improved method for computation of potentials in a realistic head shape model," *IEEE Trans. Biomed. Eng.*, vol. 42, no. 11, pp. 1094–1104, 1995.

[77] M. Fuchs, M. Wagner, and J. Kastner, "Boundary element method volume conductor models for EEG source reconstruction," *Clin. Nuerophysiol.*, vol. 112, pp. 1400–1403, 2001.

[78] R. Oostenveld and T. F. Oostendorp, "Validating the boundary element method for forward and inverse EEG computations in the presence of a hole in the skull," *Hum. Brain Mapp.*, vol. 17, no. 3, pp. 179–192, 2002.

[79] C. G. Bénar and J. Gotman, "Modeling of post-surgical brain and skull defects in the EEG inverse problem with the boundary element method," *Clin. Neurophysiol.*, vol. 113, pp. 48–56, 2002.

[80] D. B. Geselowitz., "On bioelectric potentials in an inhomogeneous volume conductor.," *Biophys. J.*, vol. 1, no. 7, pp. 1–11, 1967.

[81] R. C. Barr, T. C. Pilkington, J. P. Boineau, and M. S. Spach, "Determining surface potentials from current dipoles with applications to electrocardiography," *IEEE Trans. Biomed. Eng.*, vol. 13, pp. 88–97, 1966.

[82] C. L. Barnard, I. M. Duck, and M. S. Lynn, "The application of electromagnetic theory to electrocardiology. i. derivation of the integral equations," *Biophys. J.*, vol. 7, no. 443-462, 1967.

[83] A. C. L Barnard, I. M. Duck, M. S. Lynn, and W. P. Timlake, "The application of electromagnetic theory to electrocardiography. ii. numerical solution of the integral equations.," *Biophys. J.*, vol. 7, pp. 463–491, 1967.

[84] A. S. Ferguson and G. Stroink, "Factors affecting the accuracy of the boundary element method in the forward problem i: Calculating surface potentials," *IEEE Trans. Biomed. Eng.*, vol. 44, pp. 1139–1155, 1997.

[85] M. S. Lynn and W. P. Timlake, "The use of multiple deflations in the numerical solution of singular systems of equations, with applications to potential theory," *SIAM Journal of Numerical Analysis*, vol. 5, pp. 303–322, 1968.

[86] S. Rush and D. A. Driscoll, "EEG electrode senstivity: An application of reciprocity," *IEEE Trans. Biomed. Eng.*, vol. 16, pp. 15–22, 1969.

[87] K. Özdemir and N. G. Gençer, "A new finite element method formulation for the forward problem solution of electro-magnetic source localization," in *19th Annual International Conference Proceedings of the IEEE Engineering in Medicine and Biology Society*, 1997, pp. 2104–2107.

[88] C. E. Acar and N. G. Gençer, "Forward problem solution of esi using FEM and BEM with quadratic isoparametric elements," in *Proc. of IEEE EMBS Conf.*, September 1999.

[89] Z. Akalın and N. G. Gençer, "Investigating the effects of eye conductivity on EMSI forward problem using a realistic BEM head model," in *Proc. of Int. J. Bioelectromagn.*, 2002, vol. 4, pp. 219–220.

[90] M. J. van Burik and M. J. Peters, "Estimation of the electric conductivity from scalp measurements: feasibility and application to source localization," *Clin. Neurophysiol.*, vol. 111, pp. 1514–1521, 2000.

[91] F. Babiloni, F. Carducci, F. Cincotti, C. Del Gratta, V. Pizzella, G. L. Romani, P. M. Rossini, F. Tecchio, and C. Babiloni, "Linear inverse source estimate of combined EEG and MEG data related to voluntary movements," *Hum. Brain Mapp.*, vol. 14, pp. 197–209, 2001.

[92] M. Fuchs, R. Drenckhahn, H. A. Wiscmann, and M. Wagner, "An improved boundary element method for realistic volume conductor modeling," *IEEE Trans. Biomed. Eng.*, vol. 8, no. 980-997, 1998.

[93] L. A. Geddes and L. E. Baker, "The specific resistance of biological materials–a compendium of data for the biomedical engineer and physiologist," *Med. Biol. Eng.*, vol. 5, pp. 271–293, 1967.

[94] H. Suzuki and J. Toriwaki, "Automatic segmentation of head MRI images by knowledge guided thresholding," *Computerized Med. Imag. Graphics*, vol. 15, no. 4, pp. 233–240, 1991.

[95] C. Li, D. B. Godlgof, and L. O. Hall, "Knowledge-based classification and tissue labelling of mr images of human brain," *IEEE Trans. Med. Imag.*, vol. 12, pp. 740–750, 1993.

[96] M. E. Brummer, R. M. Mersereau, R. L. Eisner, and R. R. J. Lewine, "Automatic detection of brain contours in MRI data sets," *IEEE Trans. Med. Imag.*, vol. 12, pp. 153–166, 1993.

[97] M. S. Atkins and B. T Mackiewich, "Fully automatic segmentation of the brain in MRI," *IEEE Trans. Med. Imag.*, vol. 17, pp. 98–107, 1998.

[98] H. Tang, E. X. Wu, Q. Y. Ma, D. Gallagher, G. M. Perera, and T. Zhuang, "MRI brain image segmentation by multi-resolution edge detection and region selection," *Computerized Medical Imaging and Graphics*, vol. 24, pp. 349–357, 2000.

[99] Z. Y. Shan, G. H. Yue, and J. Z. Liu, "Automated histogram-based brain segmentation in t1-weighted three-dimensional magnetic resonance head images," *NeuroImage*, vol. 17, pp. 1587–1598, 2002.

[100] W. M. Wells, W. E. L. Grimson, R. Kikinis, and F. A. Jolesz, "Statistical intensity correction of MRI data," *SPIE*, vol. 2359, pp. 13–24, 1994.

[101] K. Held, E. R. Kops, B. J. Krause, W. M. Wells, R. Kikinis, and H. W. M. Gartner, "Markov random field segmentation of brain mr images," *IEEE Trans. Med. Imag.*, vol. 16, no. 6, pp. 878–886, 1997.

[102] M. Joshi, J. Cui, K. Doolittle, S. Joshi, D. V. Essen, L. Wang, and M. I. Miller, "Brain segmentation and the generation of cortical surfaces," *NeuroImage*, vol. 9, pp. 461–476, 1999.

[103] S. Sandor and R. Leahy, "Surface-based labeling of cortical anatomy using a deformable atlas," *IEEE Trans. Med. Imag.*, vol. 16, no. 1, pp. 41–54, 1997.

[104] S. L. Hartmann, M. H. Parks, P. R. Martin, and B. M. Dawant, "Automatic 3-d segmentation of internal structures of the head in mr images using a combination of similarity and free-form transformations: Part ii, validation on severely atrophied brains," *IEEE Trans. on Med. Imag.*, vol. 18, no. 10, pp. 917–926, 1999.

[105] J. W. Snell, M. B. Merickel, J. M. Ortega, J. C. Goble, J. R. Brookman, and N. F. Kassel, "Segmentation of the brain from 3D MRI using a hierarchical active surface template," in *Proc. of the SPIE Conference on Medical Imaging*, 1994.

[106] P. Schimpf, J. Haueisen, C. Ramon, and H. Novak, "Realistic computer modeling of electric magnetic fields of human head and torso," *Parallel Computing*, vol. 24, pp. 1433–1460, 1998.

[107] B. Yvert, O. Bertrand, J. F. Echallier, and J. Pernier, "Improved forward eeg calculations using local mesh refinement of realistic head geometries," *Electroenceph. Clin. Neurophysiol.*, vol. 95, pp. 381–392, 1995.

[108] R. Kristeva-Feige, Ch. Grimm, H.-J. Huppertz, M. Otte, A. Schreiber, D. Jger, B. Feige, M. Bchert, J. Hennig, T. Mergner, and C. H. Lcking, "Reproducibility and validity of electric source localisation with high-resolution electroencephalography," *Electroenceph. Clin. Neurophysiol.*, vol. 103, pp. 652–660, 1997.

[109] L. Rao, R. He, Y. Li, S. Liu, and W. Yan, "Computations of electroencephalography and magnetoencephalography for real head model," *IEEE Trans on magnetics*, vol. 36, no. 4, pp. 1812–1816, 2000.

[110] D. van 't Ent, J. C. de Munck, and A. L. Kaas, "A fast method to derive realistic BEM models for E/MEG source reconstruction," *IEEE Trans. Biomed. Eng.*, vol. 48, no. 12, pp. 1434–1443, 2001.

[111] Y. Wang and J. Gotman, "The influence of electrode location errors on EEG dipole source localization with a realistic head model," *Clin. Neurophysiol.*, vol. 112, pp. 1777–1780, 2001.

[112] N. B. Cuffin, D. L. Schomer, J. R. Ives, and H. Blume, "Experimental tests of EEG source localization accuracy in realistically shaped head models," *Clin. Neurophysiol.*, vol. 112, pp. 2288–2292, 2001.

[113] G. Huiskamp, M. Vroeijenstijn, R. Van Dijk, G. Wieneke, and A. C. Van Huffelen, "The need for correct realistic geometry in the inverse EEG problem," *IEEE Trans. Biomed. Eng.*, vol. 46, pp. 1281–1287, 1999.

[114] Z. Akalın and N. G. Gençer, "Mr kafa görüntülerinin bölütlenmesi," in *Biyomedikal Mühendisliği Ulusal Toplantısı Bildiriler Kitabi*, 2000.

[115] O. Nobuyuki, "A threshold selection method from gray-level histograms," *IEEE Trans. on Systems, Man, and Cybernetics*, vol. SMC-9, no. 1, pp. 62–66, 1979.

[116] M. Kass, A. Witkin, and D. Terzopoulos, "Snakes: Active contour models," *Int. J. Comput. Vision*, vol. 1, pp. 321–331, 1987.

[117] C. Xu and J. L. Prince, "Snakes, shapes and gradient vector flow," *IEEE Trans. Image Proc.*, vol. 7, no. 3, pp. 359–369, 1998.

[118] L. D. Cohen, "On active contour models and balloons," *CVGIP-Image Understanding*, vol. 53, no. 2, pp. 211–218, 1991.

[119] C. Xu and J. L. Prince, "Generalized gradient vector flow external forces for active contours," *Signal Processing*, vol. 71, pp. 131–139, 1998.

[120] A. K. Jain, *Fundamentals of Digital Image Processing*, Prentice Hall, Englewood Cliffs, 1989.

[121] R. J. Schalkoff, *Digital Image Processing and Computer Vision*, 1989.

[122] C. A. Cocosco, V. Kollokian, R. K-S. Kwan, and A. C. Evans, "Brainweb: Online interface to a 3D MRI simulated brain database," *NeuroImage, Proceedings of 3-rd International Conference on Functional Mapping of the Human Brain, Copenhagen*, vol. 5, no. 4 part 2/4, 1997, Last accessed date June 2005.

[123] T. Poston, T. Wong, and P. Heng, "Multiresolution isosurface extraction with adaptive skeleton climbing," in *Proc. of Eurographics*, 1998, vol. 17.

[124] A. Guziec, G. Taubin, F. Lazarus, and B. Horn, "Cutting and stitching: Converting sets of polygons to manifold surfaces," *IEEE Trans on visualization and computer graphics*, vol. 7, no. 2, pp. 136–151, 2001.

[125] S. H. Lo, "Automatic mesh generation over intersecting surfaces," *Int. J. for Numer. Methods in Eng.*, vol. 38, pp. 943–954, 1995.

[126] R. Lohner and P. Parikh, "Generation of three-dimensional unstructured grids by the advancing-front method," *Int. J. for Numerical Methods in Fluids*, vol. 8, pp. 1135–1149, 1988.

[127] W. E. Lorensen and H. E. Cline, "Marching cubes: A high resolution 3D surface construction algorithm," *Computer Graphics*, vol. 21, no. 4, pp. 163–169, 1987.

[128] M. Garland and P. S. Heckbert, "Surface simplification using quadric error metrics," in *Proc. of SIGGRAPH*, 1997, pp. 209–293.

[129] M. Garland, "QSlim simplification software," http://graphics.cs.uiuc.edu/∼garland/software/qslim.html, Last accessed date June 2005.

[130] P. Adjamiana, G. R. Barnesa, A. Hillebranda, I. E. Hollidaya, K.D. Singha, P.L. Furlonga, E. Harringtonb, C.W. Barclayb, and P.J.G. Route, "Co-registration of magnetoencephalography with magnetic resonance imaging using bite-bar-based fiducials and surface-matching," *Clin. Neurophysiol.*, vol. 115, pp. 691–698, 2004.

[131] K.D. Singh, I.E. Holliday, P.L. Furlong, and G.F.A. Harding, "Evaluation of MRI-MEG/EEG co-registration strategies using monte carlo simulation," *Electroenceph. Clin. Neurophysiol.*, vol. 102, pp. 81–85, 1997.

[132] G.V. Simpson, M.E. Pflieger, J.J. Foxe, S.P. Ahlfors, H.G. Jr. Vaughan, J. Hrabe, R.J. Ilmoniemi, and G. Lantos, "Dynamic neuroimaging of brain function," *J. Clin. Neurophysiol.*, vol. 12, pp. 432–449, 1995.

[133] T.D. Buchner, H.and Waberski, M. Fuchs, R. Drenckhahn, M. Wagner, and H.-A. Wischmann, "Postcentral origin of p22: evidence from source reconstruction in a realistically shaped head model and from a patient with a postcentral lesion.," *Electroenceph. Clin. Neurophysiol.*, vol. 100, pp. 332–342, 1996.

[134] D. Schwartz, D. Lemoine, E. Poiseau, and C. Barillot, "Registration of MEG/EEG data with 3D MRI: Methodology and precision issues," *Brain Topography*, pp. 101–116, 1996.

[135] H.-J. Huppertz, M. Otte, C. Grimm, R. Kristeva-Feige, T. Mergner, and C.H. Lücking, "Estimation of the accuracy of a surface matching technique for registration of EEG and MRI data," *Electroenceph. Clin. Neurophysiol.*, vol. 106, pp. 409–415, 1998.

[136] D. McNay, E. Michielssen, R. L. Rogers, S. A. Taylor, M. Akhtari, and W. W. Sutherling, "Multiple source localization using genetic algorithms," *J. of Neuroscience Methods*, vol. 64, pp. 163–172, 1996.

[137] K. Uutela, M. Hämäläinen, and R. Salmelin, "Global optimization in the localization of neuromagnetic sources," *IEEE Trans. Biomed. Eng.*, vol. 45, no. 6, pp. 716–723, 1998.

[138] J. Li, H. Zhu, and S. He, "Fast method for the localisation of current dipoles in the human brain," *Med. and Biol. Eng. and Comp.*, vol. 39, pp. 678–680, 2001.

[139] T. Nagano, Y. Ohno, H. Uesugi, and A. Ishiyama, "Multi-source localization by genetic algorithm using MEG," *IEEE Trans. on Magnetics*, vol. 34, no. 5, pp. 2976–2979, 1998.

[140] R. Cabeza and L. Nyberg, "Neural bases of learning and memory: functional neuroimaging evidence," *Current Opinion in Neurology*, vol. 13, no. 4, pp. 415–421, 2000.

[141] N. G. Gençer, , S. J. Williamson, A. Gueziec, and R. Hummel, "Optimal reference electrode location for electric source imaging," *Electroenceph. Clin. Neurophysiol.*, vol. 99, pp. 163–173, 1996.

[142] D. B. Geselowitz, "The zero of potential," *IEEE Eng. Med. and Biol. Magazine*, vol. 17, no. 1, pp. 128–132, 1998.

[143] M. S. Hämäläinen, R. Hari, R. J. Ilmoniemi, J. Knuutila, and O. V. Lounasmaa, "Magnetoencephalography theory, instrumentation, andapplications to noninvasive studies of the working human brain," *Reviews of Modern Physics*, vol. 65, no. 2, pp. 413–497, 1993.

[144] M. Fuchs, M. Wagner, T. Kohler, and H-A. Wischmann, "Linear and nonlinear current density reconstructions," *J. Clin. Neurophysiol. EEG Source Modeling.*, vol. 16, 1999.

[145] J. Sarvas, "Basic mathematical and electromagnetic concepts of the biomagnetic inverse problem," *Phys. Med. Biol.*, vol. 32, no. 1, pp. 11–22, 1987.

[146] T. Musha and Y. Okamoto, "Forward and inverse problems of EEG dipole localization," *Crit. Reviews in Biomed. Eng.*, vol. 27, no. 3-5, pp. 189–239, 1999.

[147] T S Kim, Y Zhou, S Kim, and M Singh, "EEG distributed source imaging with a realistic finite-element head model," in *Proc. IEEE Nuc. Sci. Symp. Med. Im. Conf.*, 2001, pp. M9B–17.

[148] O. Faugeras, G. Adde, G. Charpiat, C. ChefdHotel, M. Clerc, T. Deneux, R. Deriche, G. Hermosillo, R. Keriven, P. Kornprobst, J. Kybic, C. Lenglet, L. Lopez-Perez, J.-P. Papadopoulo, T. Pons, F. Segonne, B. Thirion, D. Tschumperle, T. Vieville, and N. Wotawa, "Variational, geometric, and statistical methods for modeling brain anatomy and function," *NeuroImage*, vol. 23, pp. S46–S55, 2004.

[149] J. C. Mosher, P. S. Lewis, and R. M. Leahy, "Multiple dipole modeling and localization from spatio-temporal MEG data," *IEEE Trans. Biomed. Eng.*, vol. 39, pp. 541–557, 1992.

[150] S. C. Jun, B. A. Pearlmutter, and G. Nolte, "Fast accurate MEG source localization using a multilayer perceptron trained with real brain noise," *Phys. Med. Biol.*, vol. 47, pp. 2547–2560, 2002.

[151] J. Nelder and R. Mead, "A simplex method for function minimization," *Comput. J.*, vol. 4, pp. 308–313, 1965.

[152] D. Weinstein, L. Zhukov, and C. Johnson, "Lead-field bases for electroencephalography source imaging," *Annals of Biomed. Eng.*, vol. 28, no. 9, pp. 1059–1164, 2000.

[153] S. Finke and R. M. Gulrajani, "Conventional and reciprocal approaches to the inverse dipole localization problem of electroencephalography," *IEEE Trans. Biomed. Eng.*, vol. 50, 2003, preprint.

[154] D. W. Marquardt, "An algorithm for least-squares estimation of nonlinear parameters," *J. Soc. Indust. Appl. Math.*, vol. 11, pp. 431–441, 1963.

[155] M. Huang, C. Aine, S. Supek, E. Best, D. Ranken, and E. Flynn, "Multi-start downhill simplex method for spatio-temporal source localization in magnetoencephalography.," *Electroenceph. Clin. Neurophysiol.*, vol. 108, pp. 32–44, 1998.

[156] A. Achim, F. Richer, and J-M. Saint-Hilaire, "Methodological considerations for the evaluation of spatio-temporal source models," *Electroenceph. Clin. Neurophysiol.*, vol. 79, pp. 227–240, 1991.

[157] D. Cabrera Fernandez and Grave de, "Neural bases of learning and memory: functional neuroimaging evidence," *Current Opinion in Neurology*, vol. 13, no. 4, pp. 415–421, 2000.

[158] W. Miltner, C. Braun, Jr. R. Johnson, G. V. Simpson, and D. S. Ruchkin, "A test of brain electrical source analysis (BESA): a simulation study.," *Electroenceph. Clin. Neurophysiol.*, vol. 91, pp. 295–310, 1994.

[159] R. O. Schmidt, "Multiple emitter location and signal parameter estimation," *IEEE Trans. Antennas. Prop.*, vol. 34, pp. 276–280, 1986.

[160] J. C. Mosher and R. M. Leahy, "Recursive MUSIC: a framework for EEG and MEG source localization," *IEEE Trans. Biomed. Eng.*, vol. 45, pp. 1342–1354, 1998.

[161] J. C. Mosher and R. M. Leahy, "Source localization using recursively applied and projected (rap) music," *IEEE Trans. Signal Proc.*, vol. 47, pp. 332–340, 1999.

[162] A. J. Bell and T. J. Sejnowski, "An information-maximization approach to blind seperation and blind deconvolution," *Neural Comput.*, vol. 7, pp. 1129–1159, 1995.

[163] L. Zhukov, D. Weinstein, and C. R. Johnson, "Statistical analysis for FEM EEG source localization in realistic head models," School of Computing Technical Report UUCS-2000-003, University of Utah, February 2000.

[164] A. K. Liu, A. M. Dale, and J. W. Belliveau, "Monte carlo simulation studiesof EEG and MEG localization accuracy," *Hum. Brain Mapp.*, vol. 16, pp. 47–62, 2002.

[165] I. F. Gorodnitsky, J. S. George, and B. D. Rao, "Neuromagnetic source imaging with FOCUSS: a recursive weighted minimum norm algorithm," *Electroenceph. Clin. Neurophysiol.*, vol. 95, pp. 231–251, 1995.

[166] C. L. Lawson and R. J. Hanson, *Solving least squares problems*, Englewood Cliffs, NJ: Prentice Hall, 1974.

[167] R.D. Pasqual-Marqui, C.M. Michel, and D. Lehmann, "Low resolution electromagnetic tomography: a new method to localize electrical activity in the brain.," *Int. J. Psychophysiol.*, vol. 18, pp. 49–65, 1994.

[168] R. Grave de Peralta and S. Gonzalez Andino, "Comparison of algorithms for the localization of focal sources: evaluation with simulated data and analysis of experimental data (online journal)," *Int. J. Bioelectromagn.*, 2002.

[169] G.R. Barnes and A. Hillebrand, "Statistical flattening of MEG beamformer images.," *Hum. Brain Mapp.*, vol. 18, pp. 1–12, 2003.

[170] K. Kobayashi, H. Yoshinaga, M. Oka, Y. Ohtsuka, and J. Gotman, "A simulation study of the error in dipole source localization for EEG spikes with a realistic head model.," *Clin. Neurophysiol.*, vol. 114, pp. 1069–1078, 2003.

[171] B. Yvert, O. Bertrand, J. F. Echallier, and J. Pernier, "Improved dipole localization using local mesh refinement of realistic head geometries: an EEG simulation study," *Electroenceph. Clin. Neurophysiol.*, vol. 99, pp. 79–89, 1996.

[172] B. Vanrumste, G. Van Hoey, R. Van de Walle, M. R. P. D'Have, I. A. Lemahieu, and P. A. J. M. Boon, "Comparison of performance of spherical and realistic head models in dipole localization from noisy EEG.," *Med. Eng. Phys.*, vol. 24, pp. 403–418, 2002.

[173] K. Whittingstall, G. Stroink, L. Gates, J. Connolly, and A. Finley, "Effects of dipole position, orientation and noise on the accuracy of EEG source localization," *Biomed. Eng. Online*, pp. 2–14, 2003.

[174] M. Fuchs, J. Kastner, M. Wagner, S. Hawes, and J.S. Ebersole, "A standardized boundary element method volume conductor model.," *Clin. Nuerophysiol.*, vol. 113, pp. 702–712, 2002.

[175] G.L. Barkley and C. Baumgartner, "MEG and EEG in epilepsy (review)," *J. Clin. Neurophysiol.*, vol. 20, pp. 163–178, 2003.

[176] P. Ungan, S. Yagcioglu, and C. Goksoy, "Differences between the N1 waves of the responses to interaural time and intensity disparities: scalp topography and dipole sources.," *Clin. Neurophysiol.*, vol. 112, pp. 485–498, 2001.

[177] B. W. Johnson, M. Hautus, and W. C. Clapp, "Neural activity associated with binaural processes for the perceptual segregation of pitch," *Clin. Neurophysiol.*, vol. 114, pp. 2245–2250, 2003.

[178] C. Ponton, J. J. Eggermont, D. Khosla, B. Kwong, and M. Don, "Maturation of human central auditory system activity: separating auditory evoked potentials by dipole source modeling," *Clin. Neurophysiol.*, vol. 113, pp. 407–420, 2002.

[179] P. M. Gilley, A. Sharma, M. Dorman, and K. Martin, "Developmental changes in refractoriness of the cortical auditory evoked potential," *Clin. Neurophysiol.*, vol. 116, pp. 648–657, 2005.

[180] D. R. Stapells, "The tone-evoked abr: Why it's the measure of choice of young infants," *The Hearing Journal*, vol. 55, pp. 14–18, 2002.

[181] P. Korczak, D. Kurtzberg, and D. R. Stapells, "Effects of sensorineural hearing loss and personal hearing aids on cortical event-related potential and behavioral measures of speech-sound processing," *Ear and Hearing*, 2005.

[182] D. R. Stapells, "The Human Auditory Physiology Laboratory Homepage School of Audiology and Speech Sciences, The University of British Columbia, Vancouver, B.C., Canada," http://www.audiospeech.ubc.ca/haplab/haplab.htm, Last accessed date June 2005.

[183] M. Huotilainena, I. Winklera, K. Alhoa, C. Escerac, J. Virtanena, R. J. Ilmoniemie, I. P. Jääskeläinena, E. Pekkonena, and R. Naäätänena, "Combined mapping of human auditory EEG and MEG responses," *Electroenceph. Clin. Neurophysiol.*, vol. 108, pp. 370–379, 1998.

[184] T. Hamada, "A neuromagnetic analysis of the mechanism for generating auditory evoked fields," *Int. J. of Psychophysiology*, vol. 56, pp. 93–104, 2005.

[185] J. Virtanen, J. Ahveninen, R. J. Ilmoniemi, R. Näätänen, and E. Pekkonen, "Replicability of MEG and EEG measures of the auditory N1/N1m-response," *Electroenceph. Clin. Neurophysiol.*, vol. 108, pp. 291–298, 1998.

[186] C. Mulert, G. Juckel, H. Augustin, and U. Heger, "Comparison between the analysis of the loudness dependency of the auditory N1/P2 component with LORETA and dipole source analysis in the prediction of treatment response to the selective serotonin reuptake inhibitor citalopram in major depression," *Clin. Neurophysiol.*, vol. 113, pp. 1566–1572, 2002.

[187] W. A. Teder-Sälejärvi, K. L. Pierce, E. Courchesne, and S. A. Hillyard, "Auditory spatial localization and attention deficits in autistic adults," *Cognitive Brain Research*, vol. 23, pp. 221–234, 2005.

[188] S.-H. Jin, B.-J. Ham, and S. Y. Kim, "Functional clustering in EEG photic and auditory driving in schizophrenia," *Int. J. of Psychophysiology*, vol. 56, pp. 249–259, 2005.

[189] C. Y. Ducommun, M. M. Murray, G. Thut, A. Bellmann, I. Viaud-Delmon, S. Clarke, and C. M. Michel, "Segregated processing of auditory motion and auditory location: an ERP mapping study," *NeuroImage*, vol. 16, pp. 76–88, 2002.

[190] A. Gutschalk, R. D. Patterson, M. Scherg, S. Uppenkamp, and A. Rupp, "Temporal dynamics of pitch in human auditory cortex," *NeuroImage*, vol. 22, pp. 755–766, 2004.

[191] Y. G. Xu, G. R. Li, and Z. P. Wu, "A novel hybrid genetic algorithm using local optimizer based on heuristic pattern move," *Applied Artificial Intelligence*, vol. 15, pp. 601–631, 2001.

[192] C. Darwin, *The origin of species by means of natural selection*, London & Toronto, J.M. Dent & sons, 1928.

[193] J. C. Mosher, R. M. Spencer, M. E. Leahy, and P. S. Lewis, "Error bounds for EEG and MEG dipole source localization," *Electroenceph. Clin. Neurophysiol.*, vol. 86, pp. 303–321, 1993.

[194] D. Lehmann, *Principles of spatial analysis.*, vol. 1. Methods of analysis of brain electrical and magnetic signals, Handbook of electroencephalography and clinical neurophysiology, Elsevier, Amsterdam, 1987.

[195] M. Scherg, "Functional imaging and localization of electromagnetic brain activity," *Brain Topography*, vol. 5, pp. 361–364, 1992.

[196] J. C. De Munck, J. P. A. Verbunt, D. Van't Ent, and B. W. Van Dijk B W, "The use of an MEG device as 3D digitizer and motion monitoring system," *Physics in Med. and Biol.*, vol. 46, pp. 2041–2052, 2001.

APPENDIX A

BEM FORMULATION

In BEM the integral equations Equation (2.1) and Equation (2.2) are discretized. The functions $g(\vec{r})$ and $\vec{B}_0(\vec{r})$ in Equation (2.1) and Equation (2.2) are defined as

$$g(\vec{r}) = \frac{1}{4\pi\sigma_0}\frac{\vec{p}\cdot\vec{R}}{R^3} \tag{A.1}$$

$$\vec{B}_0(\vec{r}) = \frac{\mu_0}{4\pi}\frac{\vec{p}\times\vec{R}}{R^3} \tag{A.2}$$

where $\vec{p}$ represents a current dipole source, $\vec{R} = \vec{r} - \vec{r'}$ is the vector between a field point and the source point. σ_0 is the unit conductivity and μ_0 is the permeability of the vacuum. The functions g and $\vec{B}_0$ represent the contribution of the primary sources whereas the second terms in Equation (2.1) and Equation (2.2) are the secondary fields representing the effects of conductivity interfaces.

To solve the above equations numerically, each surface S_k is discretized into N area elements. The surface integration in Equation (2.1)can then be obtained by summing up the integrals on these elements.

$$\int_{S_k} \phi(\vec{r'})\frac{\vec{R}}{R^3}\cdot d\vec{S}_k(\vec{r'}) = \sum_{i=1}^{N}\int_{S_k^i} \phi(\vec{r'})\frac{\vec{R}}{R^3}\cdot d\vec{S}_k^i(\vec{r'}) \tag{A.3}$$

where S_k^i represents the area of the ith element on surface S_k. On each element, ϕ is represented by a number of interpolation functions.

$$x = \sum_{i=1}^{m} N_i(\zeta, \eta, \nu) x_i^e \tag{A.4}$$

$$y = \sum_{i=1}^{m} N_i(\zeta, \eta, \nu) y_i^e \tag{A.5}$$

$$z = \sum_{i=1}^{m} N_i(\zeta, \eta, \nu) z_i^e \tag{A.6}$$

$$\phi = \sum_{i=1}^{m} N_i(\zeta, \eta, \nu) \phi_i^e \tag{A.7}$$

where m is the number of nodes in an element, x_i^e, y_i^e, z_i^e are the coordinates and ϕ_i^e is the potential of the ith node. The shape functions are defined on the local coordinates (ζ, η, ν) of a parent element. Since the parent element is planar, ν is a dependent variable (i.e. $\nu = 1 - \zeta - \eta$). Consequently, the element surface integrations given on the right-hand side of Equation (A.3) can be expressed in terms of the local coordinates (ζ, η). Thus Equation (A.3) can be rewritten as

$$\int_{S_k} \phi(\vec{r}') \frac{\vec{R}}{R^3} \cdot d\vec{S}(\vec{r}') = \sum_{i=1}^{N} \int_0^1 \int_0^{1-\eta} \phi(\vec{r}') \frac{\vec{R}}{R^3} \cdot \vec{n} G d\zeta d\eta \tag{A.8}$$

where G is defined as

$$G = |\frac{\partial \vec{r}'}{\partial \zeta} \times \frac{\partial \vec{r}'}{\partial \eta}| \tag{A.9}$$

The integral on the local coordinates can be approximated by using the Gauss-Legendre quadrature, which evaluates the integrand at Gauss points (ζ_i, η_i), $j = 1, ..., gp$, while multiplying each value with a certain weight w_j. That is, if f is the integrand then

$$\int_0^1 \int_0^{1-\eta} f(\zeta, \eta) d\zeta d\eta \approx \frac{1}{2} \sum_{j=1}^{gp} f(\zeta_j, \eta_j) w_j \tag{A.10}$$

Thus the surface integrals can be expressed as

$$\int_{S_k} \phi(\vec{r}') \frac{\vec{R}}{R^3} \cdot d\vec{S}(\vec{r}') = \sum_{i=1}^{N} \frac{1}{2} \sum_{j=1}^{gp} \phi(\zeta_j, \eta_j) w_j \frac{\vec{R}(\zeta_j, \eta_j)}{R(\zeta_j, \eta_j)^3} \cdot \vec{n}(\zeta_j, \eta_j) G(\zeta_j, \eta_j) \tag{A.11}$$

Since ϕ at any local coordinate can be expressed in terms node potentials ϕ_j, this integration can simply be written as

$$\int_{S_k} \phi(\vec{r}\,') \frac{\vec{R}}{R^3} \cdot d\vec{S}(\vec{r}\,') = \sum_{j=1}^{M_k} c_j \phi_j \tag{A.12}$$

where c_j represents the contribution of the jth node on the integration and M_k is the total number of nodes on the kth surface. By including the contribution of the other surfaces, the second term in the right-hand side of Equation (2.1) can be obtained as a linear combination of the node potentials. If ϕ is to be calculated at M nodes, then in matrix notation we obtain,

$$\Phi = \mathbf{C}\Phi + g \tag{A.13}$$

where Φ is an $M \times 1$ vector of node potentials, $\mathbf{C}$ is an $M \times M$ matrix whose elements are determined by the geometry and electrical conductivity information, and g is an $M \times 1$ vector representing the contribution of the primary sources. Consequently, Φ can be calculated as follows:

$$\Phi = [\mathbf{I} - \mathbf{C}]^{-1} g \tag{A.14}$$

Once ϕ is solved, $\vec{B}$ can be calculated using the potential values in the right-hand side of Equation (2.2).

VITA

Zeynep Akalın Acar was born in Izmir on 1974. She received her B.S. degree in Electronics Engineering from the Hacettepe University in 1996 and her M.S. degree in Electronics engineering from the Middle East Technical University in 1999. She has worked as a research assistant in the Department of Electrical and Electronics Engineering of Dokuz Eylül University from 1996 to 1997 and of Middle East Technical University from 1997 to 2005. During these periods, she was responsible from the antenna laboratory, analog and digital electronics laboratories, biomedical engineering laboratory and medical imaging projects. Her main areas of interest are electromagnetic source imaging, numerical methods, and head modeling.

Journal Papers

- N. G. Gençer, Z. Akalın-Acar, *Use of the Isolated Problem Approach for multi-compartment BEM models of Electro-magnetic Source Imaging*, Physics in Medicine and Biology, Vol:50, pp:3007-3022, 2005.
- Z. Akalın-Acar, N. G. Gençer, *An advanced BEM implementation for the forward problem of Electro-Magnetic Source Imaging*, Physics in Medicine and Biology, Vol: 49, no: 21, pp: 5011-5028, 2005.

Conference Papers

- N. G. Gençer, Z. Akalın-Acar, *Use of Isolated Problem Approach for the multi-compartment BEM models of Electric Source Imaging*, Proc. of BEM NFSI 2005, Minneapolis, USA.
- Z. Akalın-Acar, N. G. Gençer, *Accelerated BEM for the Calculation of the potential and magnetic fields*, Proc. of BIOMAG 2004,

Boston, USA.

- Z. Akalın-Acar, N. G. Gençer, *Electro-Magnetic Source Imaging with Realistic Head Models Using the Genetic Algorithms*, Proc. of BIOMAG 2004, Boston, USA.
- Z. Akalın-Acar, N. G. Gençer, *An Accelerated BEM Formulation for the Forward Problem Solution of ESI Using Realistic Head Models*, Proc. of IEEE EMBS Conf. CD-ROM, 2003, Cancun, Mexico.
- Z. Akalın, N G. Gençer, *Elektro-Manyetik Kaynak Görüntüleme Ileri Probleminde Gerçekçi Kafa Modelleri ve Iletkenliğe Duyarlılık Analizi*, Biyomedikal Mühendisliği Ulusal Toplantısı Bildiriler Kitabi, pp. 64-67, 2003, Istanbul, Turkey.
- Y. Ataseven, C. E. Acar, Z. Akalın, N. G. Gençer, *Insan Beyninin Elektro-Manyetik Kaynak Görüntülemesinde Sınır Elemanları Yönteminin (SEY) Paralel Uygulaması*, Biyomedikal Mühendisliği Ulusal Toplantısı Bildiriler Kitabi, pp. 197-201, 2003, Istanbul, Turkey.
- Z. Akalın, N. G. Gençer, *Investigating the Effects of Eye Conductivity on EMSI Forward Problem Using a Realistic BEM Head Model*, Proc. of International Journal of Bioelectromagnetism, vol. 4, pp. 219-220, 2002, Montreal, Canada.
- Z. Akalın, C. E. Acar, N. G. Gençer, *Development of Realistic Head Models for Electro-magnetic Source Imaging of the Human Brain*, Proc. of IEEE EMBS Conf. CD-ROM, 2001, Istanbul, Turkey.
- Z. Akalın, N. G. Gençer, *Forward Problem Solution of EMSI's with BEM Using Realistic Head Models*, Biomedizinische Technik, pp. 135-137, 2001, Innsbruck, Austria.
- Z. Akalın, N. G. Gençer, *Analytical Potential Solutions for ESIs Using Spheroidal Head Models*, Brain-Machine Workshop, 2000, Ankara, Turkey.
- Z. Akalın, N. G. Gençer, *MR Kafa Görüntülerinin bölütlenmesi*, Biyomedikal Mühendisliği Ulusal Toplantısı Bildiriler Kitabi, vol.138,

2000, Istanbul, Turkey.

- Z. Akalın, B. M. Eyüboğlu, *Magnetic Resonance Elastography and Inverse Problem Solution in Elasticity*, Proc. of EMBC, 1999, Atlanta, USA.
- Z. Akalın, B. M. Eyüboğlu, *Manyetik Rezonans Elastografi ve Elastisite Probleminde Ileri ve Geri Çzm*, Elektrik-Elektronik Bilgisayar Mühendisliği 8. Ulusal Kongresi Bildiri Kitabi, pp. 200-203, 1999, Gaziantep, Turkey.

Thesis

- Z. Akalın, Imaging Elasticity with Nuclear Magnetic Resonance, MSc Thesis, Department of Electrical and Electronics Engineering, METU, September 1999.